DGK Ausschuss Geodäsie (DGK)
der Bayerischen Akademie der Wissenschaften

Reihe C | Dissertationen | Heft Nr. 961

Xinyuan Jiang

Multi-GNSS Real-time Precise Satellite Clock Estimation

München 2025

Verlag der Bayerischen Akademie der Wissenschaften, München

ISSN 0065-5325 ISBN 978-3-7696-5373-1

DGK Ausschuss Geodäsie (DGK)
der Bayerischen Akademie der Wissenschaften

Reihe C Dissertationen Heft Nr. 961

Multi-GNSS Real-time Precise Satellite Clock Estimation

An der Fakultät VI - Planen Bauen Umwelt
der Technischen Universität Berlin
zur Erlangung des akademischen Grades
Doktor der Ingenieurwissenschaften
- Dr.-Ing. -
genehmigte Dissertation

vorgelegt von

Xinyuan Jiang, M. Sc.

München 2025

Verlag der Bayerischen Akademie der Wissenschaften, München

ISSN 0065-5325 ISBN 978-3-7696-5373-1

Adresse des Ausschusses Geodäsie (DGK)
der Bayerischen Akademie der Wissenschaften:

Ausschuss Geodäsie (DGK) der Bayerischen Akademie der Wissenschaften
Alfons-Goppel-Straße 11 ● D – 80 539 München
Telefon +49 – 89 – 23 031 1113 ● Telefax +49 – 89 – 23 031 - 1283 / - 1100
e-mail post@dgk.badw.de ● http://www.dgk.badw.de

Promotionsausschuss:
Gutachter: Prof. Dr. Dr. h.c. Harald Schuh
Gutachter: Prof. Dr.-Ing. Heiner Kuhlmann
Gutachter: Prof. Dr. Maorong Ge
Gutachter: Prof. Dr. Günther Retscher

Tag der wissenschaftlichen Aussprache: 10. Januar 2025

Diese Dissertation ist auf dem Server des Ausschusses Geodäsie (DGK)
der Bayerischen Akademie der Wissenschaften, München unter <http://dgk.badw.de/>
sowie auf dem Server der TU Berlin unter < https://doi.org/10.14279/depositonce-23173>,
Berlin 2025, elektronisch publiziert

ISSN 0065-5325 ISBN 978-3-7696-5373-1

Abstract

Nowadays, Global Navigation Satellite Systems (GNSS) play a pivotal role in precise positioning in geosciences and various related domains. Among all GNSS positioning services, real-time precise point positioning (PPP) stands out for its global consistency and flexibility. The quality of real-time services based on PPP hinges particularly on the precision and resilience of satellite orbit and clock corrections. Despite its importance, maintaining continuous and long-term reliable real-time service remains a complex challenge. This dissertation introduces innovative methods, including algorithms, strategies, and system designs, to enhance the performance of real-time services. The core contributions of this work are highlighted below:

An innovative approach for real-time clock rapid recovery is developed. Traditional clock estimation strategies require extensive time, often hours, to regain accuracy after interruptions, leading to significant gaps in real-time products and deteriorating the performance of real-time PPP services. The proposed method accelerates clock estimation restarts by leveraging historical data and previously saved filter state information, thus minimizing downtime. Additionally, it employs multi-thread processing to address the issue of thread concurrency effectively.

A novel Decentralized Clock Estimation (DECE) strategy for high-rate real-time multi-GNSS clock estimation is also proposed. The complexity of updating clocks in real-time at high frequencies poses significant challenges, especially with the expansion of multi-GNSS constellations and the increasing number of stations. The DECE strategy enables multiple Un-Differenced (UD) estimators and Epoch-Differenced (ED) estimators running on separate computers and even locations, with their outputs merged to produce a unified clock estimation to reduce the computational burden and to improve the product availability. The experimental results show that the DECE method greatly enhances clock estimation efficiency while maintaining performance nearly identical to that of the original clock products.

The evolution of the GNSS Real-Time Precision Positioning Service (RTPPS) system at the German Research Centre for Geosciences (GFZ) is comprehensively outlined in this dissertation. The system integrates real-time orbit determination, clock estimation, Uncalibrated Phase Delay (UPD) estimation, and PPP functionalities along with regional augmentation features, with a particular emphasis on system architecture

and performance evaluation. Additionally, it extensively analyzes the impact of network configuration on real-time clock estimation.

The Real-Time Positioning and Monitoring (RTPM) system is developed to retrieve real-time high-precision ground displacement for hazard monitoring and early warning in the framework of the Early-Warning and Rapid ImpaCt Assessment with real-time GNSS in the Mediterranean (EWRICA) project. The RTPM system has currently been deployed to the Rete INtegrata Nazionale GNSS (RING) network in Italy and the Badan Informasi Geospasial (BIG) network in Indonesia. its exceptional positioning performance has been demonstrated operationally.

In summary, this dissertation primarily focuses on improving the performance of real-time precise positioning service, particularly in the real-time satellite clock estimation. The introduction of various new strategies has significantly improved the efficiency and stability of real-time GNSS service. Both experimental validation and in-field operational deployment through the EWRICA project have demonstrated that the improved RTPPS system can offer users a variety of PPP services, yielding promising results.

Keywords: multi-GNSS; PPP; satellite clock estimation; ambiguity resolution; square root information filter; quality control; clock rapid recovery; decentralized; real-time service; PPP-AR; PPP-RTK; GFZ; RTPPS; RTPM, RTPPP; EWRICA project; geoscience.

Zusammenfassung

Heutzutage spielen globale Navigationssatellitensysteme (GNSS) eine zentrale Rolle bei der präzisen Positionierung in den Geowissenschaften und verschiedenen verwandten Bereichen. Unter allen GNSS-Positionierungsdiensten zeichnet sich die Echtzeit-Präzisionspunktpositionierung (PPP) durch ihre globale Konsistenz und Flexibilität aus. Die Qualität der Echtzeitdienste, die auf PPP basieren, hängt insbesondere von der Präzision und Widerstandsfähigkeit der Satellitenorbit- und Uhrenkorrekturen ab. Trotz ihrer Bedeutung bleibt die Aufrechterhaltung eines kontinuierlichen und langfristig zuverlässigen Echtzeitdienstes eine komplexe Herausforderung. Diese Dissertation stellt innovative Methoden vor, einschließlich Algorithmen, Strategien und Systemdesigns, um die Leistung von Echtzeitdiensten zu verbessern. Die Kernbeiträge dieser Arbeit sind nachfolgend hervorgehoben:

Eine innovative Methode zur schnellen Wiederherstellung von Echtzeituhren wird entwickelt. Traditionelle Strategien zur Uhrenschätzung erfordern viel Zeit, oft Stunden, um die Genauigkeit nach Unterbrechungen wiederzuerlangen, was zu erheblichen Lücken in den Echtzeitprodukten führt und die Leistung der Echtzeit-PPP-Dienste verschlechtert. Die vorgeschlagene Methode beschleunigt den Neustart der Uhrenschätzung durch die Nutzung historischer Daten und zuvor gespeicherter Filterzustandsinformationen, wodurch die Ausfallzeit minimiert wird. Zusätzlich wird die sog. multi-thread Verarbeitung eingesetzt, um das Problem der Thread-Parallelität effektiv zu adressieren.

Eine neuartige dezentrale Uhrenabschätzungs- (DECE) Strategie zur Hochfrequenz-Echtzeit-Multi-GNSS-Uhrenschätzung wird ebenfalls vorgeschlagen. Die Komplexität der Echtzeitaktualisierung von Uhren mit hoher Frequenz stellt insbesondere mit der Expansion der Multi-GNSS-Konstellationen und der zunehmenden Anzahl von Stationen erhebliche Herausforderungen dar. Die DECE-Strategie ermöglicht es mehreren undifferenzierten (UD) Schätzern und epochen-differenzierten (ED) Schätzern, auf separaten Computern und sogar an verschiedenen Standorten zu laufen, wobei ihre Outputs zusammengeführt werden, um eine einheitliche Uhrenschätzung zu erzeugen, was den Rechenaufwand reduziert und die Produktverfügbarkeit verbessert. Die experimentellen Ergebnisse zeigen, dass die

DECE-Methode die Effizienz der Uhrenschätzung erheblich verbessert, während die Leistung nahezu identisch mit der der ursprünglichen Uhrenprodukte bleibt.

Die Entwicklung des GNSS-Echtzeit-Präzisionspositionierungsdienstes (RTPPS) Systems am Deutschen GeoForschungsZentrum (GFZ) wird in dieser Dissertation umfassend dargestellt. Das System integriert Echtzeit-Orbitbestimmung, Uhrenschätzung, Unkalibrierte Phasenverzögerung (UPD) Schätzung und PPP-Funktionalitäten sowie regionale Ergänzungsmerkmale, mit besonderem Schwerpunkt auf Systemarchitektur und Leistungsbewertung. Darüber hinaus wird der Einfluss der Netzwerkkonfiguration auf die Echtzeit-Uhrenschätzung ausführlich analysiert.

Das Echtzeit-Positionierungs- und Überwachungssystem (RTPM) wurde entwickelt, um Echtzeit-Hochpräzisions-Bodendeformationen für die Gefahrenüberwachung und Frühwarnung im Rahmen des Projekts *Early-Warning and Rapid ImpaCt Assessment with real-time GNSS in the Mediterranean (EWRICA)* abzurufen. Das RTPM-System wurde derzeit im *Rete INtegrata Nazionale GNSS (RING)*-Netzwerk in Italien und im *Badan Informasi Geospasial (BIG)*-Netzwerk in Indonesien eingesetzt. Seine außergewöhnliche Positionierungsleistung wurde betriebsfähig demonstriert.

Zusammenfassend konzentriert sich diese Dissertation hauptsächlich auf die Verbesserung der Leistung des Echtzeit-Präzisionspositionierungsdienstes, insbesondere bei der Echtzeit-Satellitenuhrenschätzung. Die Einführung verschiedener neuer Strategien hat die Effizienz und Stabilität des Echtzeit-GNSS-Dienstes erheblich verbessert. Sowohl die experimentelle Validierung als auch der operative Feldeinsatz durch das EWRICA-Projekt haben gezeigt, dass das verbesserte RTPPS-System den Benutzern eine Vielzahl von PPP-Diensten anbieten kann und vielversprechende Ergebnisse liefert.

Schlüsselwörter: Multi-GNSS; PPP; Satellitenuhrenschätzung; Mehrdeutigkeitsauflö sung; Square Root Information Filter; Qualitätskontrolle; schnelle Wiederherstellung der Uhr bzw. Zeit; dezentralisierte Arbeiten; Echtzeitdienst; PPP-AR; PPP-RTK; GFZ; RTPPS; RTPM, RTPPP; EWRICA-Projekt; Geowissenschaften.

Table of Contents

List of Acronyms

AC	Analysis Center
AI	Artificial Intelligence
BDS	BeiDou Navigation Satellite System
BIG	Geospatial Information Agency (Indonesian: Badan Informasi Geospasial)
BKG	Federal Agency for Cartography and Geodesy (German: Bundesamt für Kartographie und Geodäsie)
CDMA	Code Division Multiple Access
CNES	National Centre for Space Studies Centre (French: national d'études spatiales)
CORS	Continuously Operating Reference Stations
DCB	Differential Code Biases
DECE	Decentralized Clock Estimation
DOY	Day Of Year
DSB	Differential Signal Biases
DGPS	Differential Global Positioning System
ECEF	Earth Centered Earth Fixed
EGNOS	European Geostationary Navigation Overlay Service
EUROCONTROL	European Organization for the Safety of Air Navigation
ED	Epoch Differenced
ERP	Earth Rotation Parameters
EPOS	Earth Parameter and Orbit System
ESA	European Space Agency
EU	European Union
EWRICA	Early-Warning and Rapid ImpaCt Assessment with real-time GNSS in the Mediterranean
FAA	Federal Aviation Administration
FDMA	Frequency Division Multiple Access
Galileo	the European Union navigation satellite system
GAGAN	GPS Aided GEO Augmented Navigation
GDGPS	Global Differential GPS
GEO	Geostationary Earth Orbit

GFZ	German Research Centre for Geosciences (German: Deutsches GeoForschungsZentrum)
GITEWS	German-Indonesian Cooperation for a Tsunami Early Warning System
GLONASS	GLObal NAvigation Satellite System
GNSS	Global Navigation Satellite System
GPS	Global Positioning System
GSEIS	GPS - SurfacE Deformations withIn Seconds
IFB	Inter-Frequency Bias
IGS	the International GNSS Service
IGSO	Inclined Geosynchronous Orbit
IMC	Instrument Meteorological Conditions
IOD	Issue Of Data
ISB	Inter-System Bias
LAMBDA	Least-squares AMBiguity Decorrelation Adjustment
LEO	Low Earth Orbit
LPV	Localizer Performance with Vertical guidance
LSQ	Least SQuare adjustment
MEO	Medium Earth Orbit
MD	Mixed Differenced
MGEX	IGS Multi-GNSS Experiment
MSAS	Multi-functional Satellite Augmentation System
MW	Melbourne-Wübbena
NEU	North, East, and Up
NRTK	Network RTK
NTRIP	Networked Transport of RTCM via Internet Protocol
OMC	Observed Minus Computed
OSR	Observation Space Representation
PANDA	Position and Navigation Data Analyst
PCE	Precise Clock Estimation
PCO	Phase Center Offset
PCV	Phase Center Variation
PIO	Platform, Instrument and Observation
POD	Precise Orbit Determination

PPP	Precise Point Pointing
PPP-AR	PPP with Ambiguity Resolution
PPP-RA	PPP with Regional Augmentation
PPP-RTK	PPP Real Time Kinematic
PRN	Pseudo Random Noise code
RMS	Root Mean Square
RINEX	Receiver Independent Exchange Format
RING	Rete INtegrata Nazionale GNSS
RR	Rapid Recovery
RT	Real-Time
RTCA	Radio Technical Commission for Aeronautics
RTCM	Radio Technical Commission for Maritime
RTPM	Real-Time Positioning and Monitoring
RTK	Real-Time Kinematic
RTS	Real-Time Service
RTPPP	Real-Time Precise Point Positioning
RTPPS	Real-Time Precise Positioning Service
OSB	Observable-Specific signal Bias
SAPOS	Satellite Positioning Service of the German State Survey
SBAS	Satellite Based Augmentation System
SDCM	System for Differential Corrections and Monitoring
SINEX	Solution INdependent Exchange
SISRE	Signal-In-Space Ranging Error
SRIF	Square Root Information Filter
SSR	State Space Representation
STD	Standard Deviation
TTFF	Time To First Fix
UD	Un-Differenced
UPD	Uncalibrated Phase Delay
WAAS	Wide Area Augmentation System
WL	Wide Lane
WHU	Wuhan University

List of Publications

Jiang, X., Xie, W., Du, S., Ge, M., Avallone, A., Babeyko, A. Y. (2023): Real-time GNSS earth surface displacement monitoring using PPP with regional augmentation and its implementation in the EWRICA project, XXVIII General Assembly of the International Union of Geodesy and Geophysics (IUGG) (Berlin 2023). doi: 10.57757/IUGG23-3507.

Jiang, X., Avallone, A., Chousianitis, K., Rahmawan, Yan., Ge, M., Strollo A., Babeyko, A. (2022): GNSS processing for geohazard early warning: implementation in the EWRICA project. IGS 2022 Virtual Workshop, 29.06.2022. https://files.igs.org/pub/resource/pubs/workshop/2022/IGSWS2022_S09_04_Jiang.pdf.

Jiang, X., Avallone, A., Chousianitis, K., Ge, M., Babeyko, A., Strollo A., Tilmann, F., Heinloo, Andres., Ambrosio, C., Cecere, G. (2021): EWRICA project: first results for real-time GNSS in the Mediterranean Sea. 37th General Assembly of the European Seismological Commission. https://www.erasmus.gr/microsites/1193.

Jiang, X., Gu, S., Li, P., Ge, M., Schuh, H. (2019): A Decentralized Processing Schema for Efficient and Robust Real-time Multi-GNSS Satellite Clock Estimation. Remote Sensing, 11, 21, 2595. doi: 10.3390/rs11212595.

Jiang, X., Gu, S., Li, P., Ge, M., Schuh, H. (2018): Improvement on the Computationa l Efficiency and Robustness of Real-time Multi-GNSS Satellite Clock Estimation. Ge ophysical Research Abstracts Vol. 20, EGU2018-4816, 2018 EGU General Assembly 2018. https://meetingorganizer.copernicus.org/EGU2018/EGU2018-4816.pdf.

Cui, B., Jiang, X., Wang, J., Li, P., Ge, M., Schuh, H. (2023): A new large-area hierarchical PPP-RTK service strategy. GPS Solutions, 27, 134. doi: 10.1007/s10291-023-01476-8.

Xie, W., Jiang, X., Du, S., Ge, M., Schuh, H., Antonio, A., Babeyko, A. Y. (2023): Reliable co-seismic displacement from tightly integrated processing of GNSS and

Accelerometers, XXVIII General Assembly of the International Union of Geodesy and Geophysics (IUGG) (Berlin 2023). doi: 10.57757/IUGG23-1534.

Wang, J., Jiang, X., Tang, L., Qin, Z., Zuo, X., Cui, B., Ge, M., Schuh, H. (2023): Real-time GNSS Service at GFZ: Current Status and Recent Development, XXVIII General Assembly of the International Union of Geodesy and Geophysics (IUGG) (Berlin 2023). doi: 10.57757/IUGG23-3422.

Ji, R., Jiang, X., Chen, X., Zhu, H., Ge, M., Neitzel, F. (2022) Quality monitoring of real-time GNSS precise positioning service system, Geo-spatial Information Science. doi: 10.1080/10095020.2022.2070554.

Zuo, X., Jiang, X., Li, P., Wang, J., Ge, M., & Schuh, H. (2021). A square root information filter for multi-GNSS real-time precise clock estimation. Satellite Navigation, 2: 28. doi: 10.1186/s43020-021-00060-0.

Yang, X., Jiang, X., Jiang, C., Xu, L. (2021). Real-Time Modeling of Regional Tropospheric Delay Based on Multicore Support Vector Machine. Mathematical Problems in Engineering, 2021: 7468963. doi: 10.1155/2021/7468963.

Li, P., Jiang, X., Zhang, X., Ge, M., Schuh, H. (2020). GPS + Galileo + BeiDou precise point positioning with triple-frequency ambiguity resolution. GPS Solutions, 24: 78. doi: 10.1007/s10291-020-00992-1.

Li, P., Jiang, X., Zhang, X., Ge, M., Schuh, H. (2019): Kalman-filter-based undifferenced cycle slip estimation in real-time precise point positioning. GPS Solutions, 23, 99. doi: 10.1007/s10291-019-0894-3.

1 Introduction

1.1 Background

1.1.1 State of multi-GNSS

Global Navigation Satellite System (GNSS), which provides global, continuous, precise positioning services, has been widely used in various areas such as navigation, positioning, geosciences, atmospheric sciences, etc. Currently, there are four developed GNSSs, the United States Global Positioning System (GPS), the Russian GLObal NAvigation Satellite System (GLONASS), the European Union (EU) navigation satellite system (Galileo), and the Chinese BeiDou Navigation Satellite System (BDS).

The United States launched the GPS project in 1973 to overcome the limitations of previous navigation systems. It reached total operational capacity in 1995, making it the first global navigation satellite system. The GPS satellite at a medium earth orbit uses a Code Division Multiple Access (CDMA) spread-spectrum technique where the low-bit-rate message data is encoded with a high-rate pseudo-random sequence that is different for each satellite. All satellites transmit signals at two carrier frequencies, 1575.42 MHz (L1 signal) and 1227.60MHz (L2 signal), modulated with corresponding pseudo-random code and navigation data. In the framework of the GPS modernization, the L5 frequency band at 1176.45MHz is added on Block IIF and even newer satellites. A fully operational GPS constellation is designed with 32 satellites orbiting at an altitude of approximately 20,200km, which is distributed in 6 orbital planes with an inclination of 55.0°, and the ascending nodes are separated by 60.0° longitude. The current GPS constellation consists of 31 satellites, including 7 BLCOK IIR, 7 BLCOK IIR-M, 12 BLCOK IIF, and 5 BLCOK III satellites (https://www.navcen.uscg.gov/?Do=constellationStatus).

GLONASS, developed by Russia, is the second global navigation system with a comparable capacity to GPS. Unlike GPS, the operational GLONASS signal is in Frequency Division Multiple Access (FDMA) mode, i.e., satellites transmit carrier signals with slightly different frequencies to distinguish them. Each satellite used to transmit signals on two frequencies, (1602+0.5625k) MHz (L1 signal) and (1246+0.4375k) MHz (L2 signal), where k denotes the channel number. Due to the inter-satellite frequency difference of FDMA signal, GLONASS also already transmit CDMA signals already published in the interface control documents in August 2016, and newer GLONASS satellites will support CMDA single in 1202.025 MHz (L3 signal). The orbit altitude of the

GLONASS satellite is about 20200 km. A fully operational constellation consists of 27 satellites distributed in 3 orbital planes with an inclination of 64.8°, while 18 satellites are necessary for covering the territory of Russia. The current GLONASS constellation consists of 26 satellites, including 23 GNLOANSS-M and 3 GNLOANSS-K1 satellites (https://www.glonass-iac.ru/en/GLONASS/).

Galileo is a young global navigation satellite system created by the EU through the European Space Agency (ESA) and went live in 2016. Like GPS, Galileo also uses a CDMA signal system, and five frequencies are supported, which are 1575.420 MHz (E1), 1278.750 MHz (E6), 1191.795 MHz (E5), 1176.450 MHz (E5a), and 1207.140 MHz (E5b). The orbit altitude of Galileo's satellite is about 24000 km. A fully operational Galileo constellation is designed with 36 satellites distributed in 3 orbital planes with an inclination of 56.0°. The ascending nodes are separated by 120.0° longitude (8 operating satellites and two active standby satellites per orbital plane). Currently, there are 21 launched satellites available, including 2 GALILEO-I and 19 GALILEO-II satellites. It should perform better than GPS because of the higher quality satellite clock and newer hardware for all satellites (https://www.gsc-europa.eu/system-service-status/constellation-information).

The development of the Chinese BDS was carried out in three steps: from 2000 to 20 03 experimental navigation system consisting of three satellites, and by 2012 regional nav igation system covering China and neighboring regions, referred to as BDS-2. And by 202 0 global navigation system, i.e., BDS-3. On 23 June 2020, the last BDS satellite to comple te the full constellation was successfully launched and the BDS global system started its f ull operation soon. The signal mode of BDS is also CDMA which is the same as GPS and Galileo. Three frequencies are supported by BDS-2, which are 1561.098 MHz (B1I signa l), 1207.140 MHz (B2I signal), and 1268.520 MHz (B3I signal). Five frequencies are sup ported by BDS-3, which are 1561.098 MHz (B1I signal), 1575.420 MHz (B1C signal), 11 76.450 MHz (B2a signal), 1207.14 MHz (B2b signal), and 1268.520 MHz (B3I signal). A s is well known, BDS has a special constellation that contains, Geostationary Earth Orbit (GEO) satellites, and Inclined Geosynchronous Orbit (IGSO) satellites for the regional ser vices besides Medium Earth Orbit (MEO) satellites. The full BDS-2 constellation consists of 5 GEO satellites, 5 IGSO satellites, and 4 MEO satellites. The full BDS-3 constellation consists of 3 GEO satellites, 3 IGSO satellites, and 24 MEO satellites. The orbit altitude o f the GEO and IGSO satellites is about 36000 km, and the orbit altitude of the MEO satell ite is about 21600 km. The inclination of MEO and IGSO satellites is 55.0°, and all MEO

satellites are distributed in 3 orbital planes with an inclination of 55.0°. Currently there are 15 BDS-2 (5 BEIDOU-2G + 7 BEIDOU-2I + 3 BEIDOU-2M) and 29 BDS-3 satellites (2 BEIDOU-3G + 3 BEIDOU-3I + 24 BEIDOU-3M) on orbit (http://www.csno-tarc.cn/system/constellation&ce=english).

Although each system is designed and developed independently to provide its PNT service for security and/or economic reasons, great efforts are made by the system developers to realize the interoperability among the systems so that they can be easily integrated to improve the service performance in terms of the stability and robustness. Indeed, combining all GNSS brings more opportunities for widening its applications but also significant challenges in developing appropriate methods for data analysis.

1.1.2 Development of real-time precise point pointing

As the standard positioning service of each individual system has a position accuracy of several meters, scientists, especially geodesists have been working hard to improve the position accuracy to extend its applications since the beginning of GPS system. In early years, the relative positioning mode was developed and has been widely used in high accuracy positioning areas, i.e., baseline processing and Real-Time Kinematic (RTK) positioning, respectively. The principle is that the satellite orbit and clock errors as well as the atmosphere delays can be almost eliminated by differentiating between two nearby GNSS receivers because of their spatial correlation. However, the obvious drawback of the relative positioning is the dependence of the spatial correlation on the distance between the reference and user station. This means the efficiency of the aforesaid error eliminating degrades along with the increase of the inter-station distance, especially for the atmosphere delays. To solve this problem, a network of Continuously Operating Reference Stations (CORS) is utilized to provide spatially interpolated corrections of these errors under the assumption that they vary linearly with geographic location. It is also called Network RTK (NRTK) and can enlarge the inter-station distance from tens of kilometers to hundreds of kilometers. (Pratt et al. 1997; Fotopoulos and Cannon 2001; Musa et al. 2005; Snay and Soler 2008). However, with the extended inter-station distance of NRTK, coverage of oceans and rural areas remains a challenging issue.

Zumberge et al. (1997) for the first time, realized Precise Point Positioning (PPP) to achieve a position with accuracy of centimeter level and to solve the computing efficiency problem of data processing of huge GNSS networks by using daily data of a stand-alone

receiver by fixing satellite orbits and clocks to corresponding precise products. Gao and Shen (2001) demonstrated the capability of the kinematic PPP and its feasibility for real-time applications. On the one hand, in recent years more and more multi-GNSS stations around the world have been installed and set-up to provide real-time data streams. On the other hand, with the great progress in high-speed internet communication, the GNSS data stream protocol and format, i.e., Radio Technical Commission for Maritime (RTCM) and Networked Transport of RTCM via Internet Protocol (NTRIP), are designed and developed for real-time GNSS data communication. These have extended the research and application of PPP from post-processing to real-time (RTCM SC-104 Version 3.3, 2016). Then the first global real-time precise positioning system was developed by JPL (Bar-Sever et al. 2009), in which a global network with well-distributed GPS stations is employed to estimate precise orbits and clocks and the corrections with respect to the corresponding broadcast ephemeris are transmitted to users, so that users can realize real-time PPP with a stand-alone receiver. In other words, we need a sever-end to provide real-time orbits and clocks, and a user-end to undertake PPP with the precise products. Although the two ends are both essential for the service, the server-end is much more complicated and crucial because of the costly infrastructure and its maintenance and software package for the data processing. For example, the International GNSS Service (IGS) launched a real-time pilot project in 2007 to establish a real-time network to provide data streams and generate real-time products with the streaming data (Dow et al. 2009; Caissy 2012). A lot of efforts are made to improve the data quality and availability and several methods and algorithms have been developed and improved for estimating precise real-time products.

Along with the continuous improvement of the quality of satellite orbit and clock products as well as more precise understanding of GNSS error sources, PPP with accuracy on centimeter or even millimeter level becomes possible. More important is that the high accuracy can be achieved world-wide and is almost independent of the distance to the nearest reference station. Beside the high accuracy, compared with RTK and NRTK the most significant advantage of PPP is its flexibility by working on the base of a single GNSS receiver. In addition, besides precise absolute station coordinates, various parameters such as the ionosphere delay, troposphere delay and receiver clock bias can also be retrieved which widely extends its applications. Finally, for basic PPP only precise orbit and clock products are needed and the data amount is rather small and can be easily broadcasted via communication satellites for a global coverage. That means no restriction on the number of

simultaneous users. Due to the above-mentioned advantages, PPP has been comprehensively implemented in high accuracy positioning and navigation (Li et al. 2015; El-Mowafy et al. 2017; Choy et al. 2017), geoscience and meteorology (e.g. Rocken et al. 2005; Leandro et al. 2010; Blewitt et al. 2016; Hadas et al. 2020), orbit determinations for low earth orbiters (e.g. ESA. 2012; Ge et al. 2020; Allahvirdi-Zadeh et al. 2021) and so on.

However, it takes rather long time to obtain position with the aforesaid high accuracy which is called the convergence problem of PPP. Moreover, GNSS signals could be easily interrupted, especially in the severe areas, for example, in the cities with high buildings, overpasses and tunnels; consequently, re-converge is needed for PPP. In the worst case, signals from most satellites in view are interrupted again and again during the convergence process, so that a converged PPP could hardly be achieved.

Different from RTK, the ambiguity resolution at a single station in PPP is in principle impossible due to the receiver and mainly satellite dependent Uncalibrated Phase Delay (UPD). However, studies show that the UPD can be accurately estimated using observations from a global or regional network, and then the ambiguity resolution at a single station becomes possible (Ge et.al 2008; Gu et.al 2015; Li et.al 2020a). PPP with Ambiguity Resolution (PPP-AR) has much better performance compared to the ambiguity-float PPP. It has been demonstrated that PPP-AR can significantly shorten the time to first convergence and improve the positioning accuracy. (Collins et al. 2008; Ge et al. 2008; Laurichesse et al. 2008; Geng et.al 2009; Li et.al 2017; Katsigianni et.at 2019; Li et.al 2020a).

In recent years, with the modernization of GPS and GLONASS as well as the new available of Galileo and BDS, more attention has been paid to the benefit of the multi-GNSS PPP. The IGS multi-GNSS experiment (MGEX, Montenbruck et al. 2013) project has carried out by IGS in order to realize the multi-GNSS service (Steigenberger et al. 2015; Kazmierski et al. 2018; Bahadır et al. 2019). The fusion of multi-GNSS significantly increases the number of observed satellites, optimizes the spatial observation geometry, and improves convergence and accuracy of positioning especially in the environments of restricted elevation view to satellites (Li et al. 2015).

In addition, since GPS and GLONASS have started to replace the old satellites with the new satellites, which support three frequency signals, and Galileo as well as BDS support five frequencies in the original design, it is possible to take full advantage of the

multi-frequency multi-system GNSS observations on PPP now (Li et al. 2019b, Duong 2019; Li et al. 2020b; Alcay et al. 2021). Normally, the more satellites contribute to multi-frequency PPP-AR, the faster the initializations will be. For example, Geng et al. (2020) indicate that the mean initialization time of PPP-AR declines to 3 minutes in case of using 20–21 GPS, BDS, Galileo and QZSS triple-frequency satellites.

Moreover, if a regional reference network is supported, PPP with Regional Augmentation (PPP-RA) which also called as PPP Real Time Kinematic (PPP-RTK) is available to further reduce the convergence time to several epochs or even only one epoch. First, real-time precise Un-Differenced (UD) atmosphere delays can be derived from the PPP-AR solution of the reference stations and broadcast to user stations. Then, with the corrected observations, rapid or instantaneous ambiguity resolution can be carried out within the user PPP. PPP-RA technology mainly solves the problem of long convergence time of standard PPP. PPP-RA is more flexible than NRTK and it is also easy to integrate PPP-RA and NRTK to a seamless positioning service system (Li et al. 2011, Li et al. 2014; Odijk et al. 2015; Teunissen et al. 2016; Zhang et al. 2019).

Since the quality of real-time satellite orbit and clock product determines the performance of real-time PPP service, the accuracy and stability of the satellite orbit and clock is critical. The improvement of the satellite products is always the main research objective in the real-time precise positioning service.

1.1.3 Global real-time precise positioning service

Based on the development of the theory and algorithms of real-time orbit determination and clock estimation as well as precise point positioning, operational Real-Time Precise Positioning Service (RTPPS) based on PPP technology was developed. The RTPPS enables real-time PPP and other navigation and positioning applications in a global scale by providing real-time GNSS orbit and clock corrections and UPD and atmosphere delay information. There are mainly two streams of the RTPPS development, one is the commercial system, for example the Trimble RTX system (Chen et al. 2011) and the NavCom Starfire system (Dixon, 2006), the other one is for scientific and research purpose which is represented by the IGS Real-Time Services (RTS). Each commercial system has its own global network and even equipped with almost the same or very similar receivers, compatible software package at the server- and user-end and the corrections can be transmitted by both internet and communication satellites. The IGS RTS is mainly based

on the IGS global infrastructure of network stations and the data processing is carried out by its real-time analysis centers (ACs) with their own software packages. Currently there are several ACs providing RTS such as Bundesamt für Kartographie und Geodäsie (BKG), Centre national d'études spatiales (CNES), Deutsches GeoForschungsZentrum (GFZ), Wuhan University (WHU). The processing strategies of the ACs are very similar. Each AC transmitting its products but only via internet and all ACs also contribute their products to IGS RTS and a combined product is generated and disseminated via internet as the IGS RTS product for public users.

Under the framework of the IGS RTS, usually, the predicted part of the ultra-rapid orbits is used for RTS. As is well known, the Precise Orbit Determination (POD) is carried out with the IGS observations over the latest 24 hours or longer and processed in batch mode to obtain the estimated orbits and then the predicted orbits by a forward integration. The quality of orbits used in RTS depends not only on the estimation but also the time of the prediction. Therefore, the computation efficiency is also an important issue for shortening the predicting time, especially for multi-GNSS integrated processing, while observation and force models are refined for POD, such as higher order ionosphere delay corrections, solar radiation models etc. (Montenbruck et al. 2015; Prange et al. 2017; Chen et al. 2019). Until now the IGS ultra-rapid orbit is updated every 6 hours by combining the contributions of several ACs but only for GPS satellites for public usage (Dow et al. 2009; Johnston et al. 2017), although GPS and GLONASS ultra-rapid orbits and even multi-GNSS products are generated and submitted operationally by some of the ACs within the IGS MGEX project. By the way, it is also possible to update multi-GNSS orbits on the hourly base for all the constellations using different processing strategies (Li et al. 2019a). Since real-time orbit generation operates in post-processing mode and employs local hourly observation files collected by GNSS receivers, which are more stable compared to real-time streaming, the performance is generally quite stable. Moreover, a single missing update will not cause any serious problem, as the previous orbits can still be used and even with a reasonable quality if the regular update interval is 1 or 2 hours.

Different from the real-time orbit determination, the satellite clock bias in generally varies quickly in time, so it must be estimated very frequently, for example every 5 s for most of the RTS ACs. Therefore, for real-time Precise Clock Estimation (PCE) the real-time data streams must be employed, and its performance heavily relies on the stability of the data streams which could be rather fragile at least compared with the hourly files used

in POD. In addition, the real-time PCE is usually carried out by a forward filter such as Kalman filter (Bock et al. 2009; Hauschild and Montenbruck 2009), the Square Root Information Filter (SRIF) (Ge et al. 2012, Bertiger et al. 2020; Zuo et al. 2021) or sequential Least SQuare adjustment (LSQ) (Fu et al. 2019).

1.1.4 Real-time clock estimation

The critical issues of the real-time clock estimation are the computational efficiency, accuracy, and robustness. In recent years, numerous efforts have been conducted on the improvement of real-time satellite clock estimation.

As there are many ambiguities that must be estimated together with the clock parameters, the computation is rather time-consuming and could not be updated in time if a global network with many stations is processed, particularly when outliers are detected in quality control. Therefore, many researchers have studied on the clock model to improve the real-time PCE efficiency. Bock et al. (2009) developed an efficient high-rate clock interpolation approach to generate 1HZ GPS clock estimates for products of the Center for Orbit Determination in Europe (CODE). Based on simplifications neglecting correlations for phase difference processing, the computational efficiency was greatly improved to guarantee the determination of high-rate clock offsets. Combined with the absolute clock offsets estimated in the un-differenced engine and the clock offsets variations estimated in the epoch-differenced engine, Zhang et al. (2011) realized 1 Hz clock estimation using the double-thread method and applied it to real-time precise point positioning. Experiments show that the estimated high-rate clocks agree very well with the IGS final clocks and the computational efficiency can satisfy real-time PPP applications. Ge et al. (2012) developed a novel method for rapid satellite clock estimation using a mixed difference model, which utilizes both epoch-differenced carrier phase and un-differenced pseudo-range observations. The experiment shows the accuracy of the clock estimated using the new method is comparable with that of the un-differenced approach, whereas the computation time is reduced to one-tenth. At the same time, fast computation approaches optimized according to CPU structure, such as matrix operations were also skillfully introduced into GNSS data processing in order to improve the computational efficiency (Gong et al. 2018).

Since most active parameters are ambiguities in real-time clock estimation, the processing of ambiguity parameters is also one of the research directions. Blewitt et al. (2010) proposed the carrier-range method in which the ambiguity is pre-fixed and applied to the phase observations. The accuracy of carrier-range is consistent with conventional

phase observations, but avoids the estimation of the ambiguity parameter. Following the same concept, Chen et al. (2014) employs the UD ambiguity resolution method developed by Ge et al. (2008) to employ carrier-ranges in huge network processing. Specifically, UPD is pre-generated with a sparse network to guarantee PPP-AR for each receiver. Laurichesse et al. (2008, 2013) proposes an integer clock method for CNES real-time products. The Wide Lane (WL) and Narrow Lane (NL) UPD as well as integer ambiguities are fixed in real-time. Both accuracy and efficiency have been significantly improved with the help of fixed ambiguities.

Another important indicator for real-time clock estimation is the robustness. In order to achieve stable and precise clock offsets, the online quality control procedure is necessary to avoid any contamination of the estimates and divergence and even crash of the filter. In the study of Lichten et al. (1990), according to the rule of 3 Standard Deviations (STDs), predicted residuals and their STDs are used to judge whether an observation contains outlier or not and further to confirm whether the detected outlier is excluded from the processing. Fu et al. (2019) proposes an online quality control strategy for the sequential least square adjustment based on the detection-identification and adaption (DIA) approach (Teunissen 1990; Yang et al. 2006, 2010). Shi et al. (2008) develops a new method based on correlation analysis to scan for outliers in real-time localization and demonstrated its efficiency in kinematic experiments with simulated and real outliers. Zuo et al. (2021) improvs the method of Shi et al. (2008) for simultaneous handling of multiple outliers. More important is that the algorithm is optimized to provide only the essential information required in the processing to improve the computational efficiency, so that it can be applied to the real-time estimation of high-rate clocks.

Apart from the performance of the filter, the recovery from the emergencies in real-time clock estimation is also very important. First, after starting PCE processing a long converge time is needed before ambiguity, troposphere delay parameters become stable, so that the estimated clock corrections can reach an accuracy suitable for PPP service. To our expertise, this convergence time could be up to 12 hours. Then, the filter has to be restarted because of inevitable changes and events related to the processing line, such as change of processing strategies and software package, software and hardware update of computational facility, interruption of power supplement and internet connection, and also unexpected failures of any component in the whole processing line. Due to the high update rate of clock estimation, it is almost impossible to solve these problems by the filter itself. As the quality of real-time clocks is the core factor of the performance of the real-time

service, to improve the robustness of PCE to guarantee the continuous update of precise satellite clock corrections is a crucial and challenging task in RTPPS, which is also the major objective of this study.

1.2 Main contributions

The main contributions of this dissertation are as follows:

(1) A new method for real-time clock rapid recovery has been developed, addressing the issue of slow restart of real-time service. Utilizing historical observations and filter state information, this strategy significantly reduces the time needed to restart clock processes, thereby shortening service downtime intervals. A multi-thread design is employed to efficiently manage thread concurrency during implementation. This optimization elevates service efficiency, offering clients enhanced capabilities for real-time positioning.

(2) A new decentralized strategy has been proposed to enhance real-time multi-GNSS clock estimation, addressing the challenge of frequent clock updates amidst expanding multi-GNSS constellations and an increasing number of stations. The new strategy creates a distinct product line through the generation of undifferenced and epoch-differenced products across multiple computing platforms. Real-time products derived from this strategy have proven its effectiveness, showcasing significant improvements in computational efficiency, accuracy, and PPP performance.

(3) The GFZ RTPPS system is introduced, along with an analysis of the performance of real-time orbit, clock, UPD, and PPP, as well as its regional augmentation. Additionally, the impact of the number of sites on clock estimation performance has been investigated. The primary contribution of the authors to the RTPPS system lies in the development of the client-side components, encompassing UPD estimation, atmosphere augmentation, and the PPP module.

(4) Real-time precise positioning technology, based on the GFZ real-time services, has been applied in earthquake monitoring. Supported by the Early-Warning and Rapid Impact Assessment with real-time GNSS in the Mediterranean (EWRICA) project, the Real-Time Positioning and Monitoring (RTPM) system has been developed, utilizing PPP-RTK as its core positioning technology. Thanks to the augmentation with precise regional atmosphere information, rapid convergence and high accuracy real-time positioning information are achieved and applied in earthquake monitoring. The RTPM system has been successfully deployed in the Rete INtegrata Nazionale GNSS (RING) network in Italy and the BIG

(Badan Informasi Geospasial) network in Indonesia, demonstrating its great potential for widespread applications.

1.3 Outline

The dissertation is structured into seven chapters, summarized as follows:

Chapter 1 introduces the background, objectives and main contributions of this research work, as well as the outline of this dissertation.

Chapter 2 covers the foundational theories of real-time multi-GNSS data processing, including mathematical models, parameter estimation, quality control, and data transmission methods.

Chapter 3 details a method for rapid real-time clock recovery using historical observations and filter state information, significantly reducing downtime and enhancing the robustness of the system.

Chapter 4 introduces a decentralized strategy that enhances computational efficiency and system stability in real-time clock estimation by integrating estimates from various processing streams.

Chapter 5 delves into the real-time precise positioning service, utilizing the GFZ RTPPS as a case study. It offers a comprehensive overview of the system's design and architecture, assesses its performance, and addresses a specific issue: the impact of network configuration on clock performance.

Chapter 6 delves into the utilization of the RTPPS system in the realm of geoscience within the EWRICA project. This encompasses an introduction to the RTPM system as well as its implementation in earthquake monitoring efforts in Italy and Indonesia.

Chapter 7 concludes the dissertation, summarizing major achievements and suggesting directions for future research in the field.

2 PPP-based Global Real-time Precise Positioning

This chapter introduces the global real-time precise positioning service as the state-of-the-art GNSS augmentation system based on the PPP technique. We then concentrate on the mathematical models and most recent approaches for estimating real-time clock corrections. As an indispensable part of the service, real-time data communication, including observation transferring and product dissemination, is also addressed afterward. In principle, it provides an overview of RTPPS and the fundamental research carried out in this dissertation.

2.1 Global real-time precise positioning service

The standard positioning service provided by individual GNSS is based on broadcast ephemeris and pseudo-range observations. Its accuracy is usually at the meter level, making it challenging to meet precise positioning and navigation needs. In the past decades, several global/wide-area real-time precise positioning services have been developed for applications requiring high accuracy and/or reliability.

The Wide Area Augmentation System (WAAS) is a satellite-based augmentation system developed by the Federal Aviation Administration (FAA) to improve the accuracy, integrity, and availability of the GPS standard service in the area of North America (Pinker et al. 2000). WAAS was designed in 1994 and its service was first available on July 10, 2003. It is a single frequency pseudo-range differential system that uses GEO satellites to broadcast the augmentation information. The downlink signal adopts L-band with a frequency of 1575.42 MHz, the same as the GPS L1 band. Now WAAS is preparing to broadcast differential correction and integrity information on the L5 band signal to support dual-band receiver users in the future. The corrections are uploaded to the WAAS satellites and can be conveniently received by the clients. The basic data transmission rate is 250 bps, and the standard Radio Technical Commission for Aeronautics (RTCA) do-229 format is used for transmission. By comparing NRTK, WAAS provided the correction model of the satellite orbit, clock, and ionosphere model, eliminating most of the systematic errors in observations. However, the corrections are generated by the original or phase-smoothed pseudo-range, so the positioning accuracy using WAAS is about 1-2 meters.

Since the WAAS is only available in North America, the European Geostationary Navigation Overlay Service (EGNOS) system, another Satellite Based Augmentation System (SBAS), is developed to improve the positioning performance for the area of

Europe. It is jointly designed and constructed by the ESA and the European Organization for the Safety of Air Navigation (EUROCONTROL) (Gómez et al. 2003, Ventura-Traveset et al. 2015). A complete EGNOS system consists of the space segment, the ground segment, the support system, and the user segment. Currently, it supplements the GPS by reporting on the reliability and accuracy of its positioning data and sending out corrections. The system will supplement Galileo in a future version. The construction of EGNOS was implemented in November 1998, and the corresponding R&D and verification started in May 2002. In March 2011, the EGNOS Safety-of-Life Service was deemed acceptable for use in aviation. This allows European pilots to use the EGNOS system as a form of positioning during an approach and will enable pilots to land the aircraft in Instrument Meteorological Conditions (IMC) using a GPS approach. As of September 2018, Localizer Performance with Vertical guidance (LPV) landing procedures, which are EGNOS-enabled, was available at more than 180 airports across Europe. According to specifications, horizontal position accuracy when using EGNOS-provided corrections should be better than seven meters. In practice, the horizontal positioning accuracy is at the meter level. Another wide area augmentation service has also been provided in Russia by the System for Differential Corrections and Monitoring (SDCM), and in Asia, by Japan's Multi-functional Satellite Augmentation System (MSAS) and India's GPS Aided GEO Augmented Navigation (GAGAN).

Although the above services significantly enhance the standard GNSS service, more accurate positioning is needed for many applications such as decimeters or centimeter-level positioning. Since only pseudo-range observations are used in WAAS, the service performance is limited by the high measurement noise of the pseudo-range. Recently, with the application of phase observations and the increasing construction of a global real-time GNSS network, the Differential Global Positioning System (DGPS) concept was proposed. JPL first proposed a global difference system called Global Differential GPS (GDGPS) based on Gipsy software, which is a complete, high accurate, and extremely robust real-time GNSS monitoring and augmentation system (Bar-Sever et al. 2004). The GDGPS system provides the global real-time differential corrections of GNSS orbit and clock. Sub-decimeter positioning accuracy is available anywhere regardless of local infrastructure (https://www.gps.gov/governance/advisory/meetings/2013-05/bar-sever.pdf).

Along with the completeness of the global GNSS network, the performance of real-time satellite orbit and clock is also significantly improved, which makes high-accuracy

real-time PPP feasible. Typically, the predicted ultra-rapid orbits are used for real-time PPP because of the dynamic stability of satellite motion. For example, the orbits are predicted every 6 hours for IGS products and every 3 hours for GFZ and CNES products. On the contrary, due to the short-term changes of satellite clocks, the real-time clocks need to be estimated frequently, for example, every 5 seconds, by IGS ACs.

The concept of real-time PPP was first proposed by Muellerschoen et al. of JPL (Muellerschoen et al. 2001), who used high-accuracy real-time orbit and clock corrections to realize real-time PPP. As introduced in Chapter 1, standard PPP is a technique that can provide an "absolute" position using a single GNSS receiver which has been widely recognized as a promising real-time positioning technique. However, since the ambiguity of standard PPP has no natural integer property because of UPDs, the accuracy and convergence of standard PPP are somehow limited. These UPDs can be determined accurately in advance within a reference network, which is provided for PPP-AR to shorten the convergence and improve its accuracy (Collins et al. 2008; Ge et al. 2008; Laurichesse et al. 2008). However, the atmosphere parameters are complex to determine accurately at the beginning of the filter. Thus, convergence is still an issue in PPP-AR. Due to the spatial correlation of atmosphere delays, precise ionosphere and troposphere corrections can be generated based on the observations of available nearby regional stations. PPP-RA or PPP-RTK is developed by providing fast integer ambiguity resolution, which can be understood as PPP-AR using augmentation corrections. PPP-RTK has at least a similar performance as that of network RTK (Li et al. 2011; Ge et al. 2012).

The integration of real-time orbit, clock, and UPDs, alongside client capabilities for standard PPP, PPP-AR, and PPP-RTK, culminates in a unified system known as the RTPPS. This system is designed to offer a range of services tailored to user needs and dependent on the availability of requisite infrastructure. With the support of the server products, various positioning modes are supported by RTPPS. For example, if precise real-time orbit and clock corrections are provided, then standard PPP is available. If we additionally use real-time UPD products, then the integer property of the ambiguity will be recovered, and PPP-AR becomes available. Moreover, if we add precise atmosphere delay information from a regional network, then PPP-RTK becomes available. Recently, several institutions have launched their unique RTPPSs, which, despite architectural differences, share broadly similar functionalities. As one of the IGS ACs, GFZ has also developed a comprehensive RTPPS, which will be detailed in Chapter 5.

2.2 Real-time clock estimation models

2.2.1 Un-differenced model

The basic GNSS observation model using pseudo-range and carrier phase on frequency f can be expressed as,

$$\begin{cases} P_{r,f}^s = \rho_{r,f}^s - c(dt_{r,f} - dt_f^s) + d_{r,f}^s - d_f^s + Ion_{r,f}^s + T_{r,f}^s + R_{r,f}^s + M_{r,f}^s + \varepsilon_{r,f}^s \\ L_{r,f}^s = \rho_{r,f}^s - c(dt_{r,f} - dt_f^s) + \lambda_f b_{r,f}^s - \lambda_f b_f^s + \lambda_f N_{r,f}^s - Ion_{r,f}^s + T_{r,f}^s + R_{r,f}^s + m_{r,f}^s + \xi_{r,f}^s \end{cases} \tag{2.1}$$

where P and L are the code pseudo-range and carrier-phase observations, respectively; s and r are the subscript for the satellite and receiver, respectively; f is frequency index; ρ is the distance between satellite and receiver; c is the speed of light in vacuum; dt_r and dt^s refer to the receiver clock and the satellite clock bias compared to the atomic clocks of current GNSS system; d_r^s and d^s are the code biases of the receiver and satellite; b_r^s and b^s are receiver and satellite dependent UPD and it should be noted that d_r^s and b_r^s are the same for all satellites in a CDMA system; λ is the wavelength of the current frequency; N is the integer ambiguity parameter; I is the slant ionosphere delay, for multi-frequency observations, $Ion_{r,j}^s = \lambda_j^2/\lambda_1^2 \cdot Ion_{r,1}^s$; T is the slant troposphere delay; R is the effects of the relativity; M is the multipath effects on the code pseudo-range; ε is the remaining errors which are considered as white noise on the code pseudo-range; m is the multipath effects on the carrier phase; ξ is the remaining errors which are considered as white noise on the carrier phase.

The major error sources in the signal transmission path are the ionosphere delay and troposphere delay. Thanks to the frequency-dependent characteristic of ionosphere delay, an effective way to eliminate the influence of the ionosphere is to use the combination of different frequency observations. For example, the dual ionosphere-free combination can eliminate the first-order ionosphere delay, which accounts for more than 99.9% of the total value (Hernández-Pajares et al. 2011). The ionosphere-free observations can be expressed as,

$$\begin{cases} P_{r,IF}^s = f_1^2/(f_1^2 - f_2^2) * P_{r,1}^s - f_2^2/(f_1^2 - f_2^2) * P_{r,2}^s \\ L_{r,IF}^s = f_1^2/(f_1^2 - f_2^2) * L_{r,1}^s - f_2^2/(f_1^2 - f_2^2) * L_{r,2}^s \end{cases} \tag{2.2}$$

where IF subscript means ionosphere-free combination; $P_{r,IF}^{s}$ and $\Phi_{r,IF}^{s}$ are the ionosphere-free pseudo-range and carrier phase observations; f_1 and f_2 are the carrier frequency of L_1 and L_2.

The troposphere delay can be separated into two parts: hydrostatic and wet delays. The hydrostatic delay accounts for about 90% of the total delay, and it can be precisely modeled using the Hopfield model or Saastamoinen model (Hopfield 1969, Saastamoinen 1973). The wet delay accounts for about 10% of the total delay, which is difficult to be modeled because it depends on the distribution of the water vapor with high spatial and temporal variability. Usually, the wet delay is parameterized as a piece-wise constant, linear function, or random-walk process to be estimated in the data processing.

Considering the modeling and parameterization of atmosphere delay, Equation (2.1) can be expressed as,

$$\begin{cases} P_{r,IF}^{s} = \rho_{rT}^{s} - c(\delta t_r - \delta t^s) + d_{r,IF}^{s} - d_{IF}^{s} + m_r^s \cdot Z_r + R_r^s + M_{r,IF}^{s} + \varepsilon_{r,IF}^{s} \\ L_{r,IF}^{s} = \rho_{rT}^{s} - c(\delta t_r - \delta t^s) + \lambda_{IF} b_{r,IF}^{s} - \lambda_{IF} b_{IF}^{s} + \lambda_{IF} N_{r,IF}^{s} + m_r^s \cdot Z_r + R_r^s + m_{r,IF}^{s} + \xi_{r,IF}^{s} \end{cases} \tag{2.3}$$

where ρ_{rT}^{s} refers to the geometric distance plus hydrostatic troposphere delay; m_r^s refers to the wet mapping function of troposphere delay between satellite s and receiver r; Z_r is the wet zenith troposphere delay of the receiver r.

In the case of multi-constellation, the combined GPS, GLONASS, Galileo, and BDS observation model under the assumption that for each system, there is a receiver clock offset can be expressed as,

$$\begin{cases} P_{r,IF}^{s,G} = \rho_{rT}^{s,G} - c(dt_r^G - dt^{s,G}) + d_{r,IF}^{G} - d_{IF}^{s,G} + m_r^{s,G} \cdot Z_r + R_r^{s,G} + M_{r,IF}^{s,G} + \varepsilon_{r,IF}^{s,G} \\ L_{r,IF}^{s,G} = \rho_{rT}^{s,G} - c(dt_r^G - dt^{s,G}) + b_{r,IF}^{G} - b_{IF}^{s,G} + \lambda_{IF}^{G} N_{r,IF}^{s,G} + m_r^{s,G} \cdot Z_r + R_r^{s} + m_{r,IF}^{s,G} + \xi_{r,IF}^{s,G} \\ P_{r,IF}^{s,R} = \rho_{rT}^{s,R} - c(dt_r^R - dt^{s,R}) + d_{r,IF}^{R} - d_{IF}^{s,R} + m_r^{s,R} \cdot Z_r + R_r^{s,R} + M_{r,IF}^{s,R} + \varepsilon_{r,IF}^{s,R} \\ L_{r,IF}^{s,R} = \rho_{rT}^{s,R} - c(dt_r^R - dt^{s,R}) + b_r^R - b_{IF}^{s,R} + \lambda_{IF}^{R} N_{r,IF}^{s,R} + m_r^{s,R} \cdot Z_r + R_r^{s,R} + m_{r,IF}^{s,R} + \xi_{r,IF}^{s,R} \\ P_{r,IF}^{s,E} = \rho_{rT}^{s,E} - c(dt_r^E - dt^{s,E}) + d_{r,IF}^{E} - d_{IF}^{s,E} + m_r^{s,E} \cdot Z_r + R_r^{s,E} + M_{r,IF}^{s,E} + \varepsilon_{r,IF}^{s,E} \\ L_{r,IF}^{s,E} = \rho_{rT}^{s,E} - c(dt_r^E - dt^{s,E}) + b_{r,IF}^{E} - b_{IF}^{s,E} + \lambda_{IF}^{E} N_{r,IF}^{s,E} + m_r^{s,E} \cdot Z_r + R_r^{s,E} + m_{r,IF}^{s,E} + \xi_{r,IF}^{s,E} \\ P_{r,IF}^{s,C} = \rho_{rT}^{s,C} - c(dt_r^C - dt^{s,C}) + d_{r,IF}^{C} - d_{IF}^{s,C} + m_r^{s,C} \cdot Z_r + R_r^{s,C} + M_{r,IF}^{s,C} + \varepsilon_{r,IF}^{s,C} \\ L_{r,IF}^{s,C} = \rho_{rT}^{s,C} - c(dt_r^C - dt^{s,C}) + b_{r,IF}^{C} - b_{IF}^{s,C} + \lambda_{IF} N_{r,IF}^{s,C} + m_r^{s,C} \cdot Z_r + R_r^{s,C} + m_{r,IF}^{s,C} + \xi_{r,IF}^{s,C} \end{cases} \tag{2.4}$$

where the subscript G, R, E, C represent GPS, GLONASS, Galileo, and BDS satellite.

It should be noted that in the basic model for clock estimation, we typically consider only float ambiguity estimation. In the subsequent discussion of this section, we will combine the integer ambiguity and UPD parameters into a float ambiguity parameter, denoted as B. The clock estimation model with ambiguity resolution will be discussed in detail in section 2.4. B can be expressed as,

$$B_r^s = N_r^s + b_r^s - b^s \tag{2.5}$$

During clock estimation, besides the satellite orbits, station coordinates can be fixed and estimated precisely in advance to reduce the number of unknowns. As demonstrated, the satellite Differential Signal Biases (DSB) for each channel is stable enough. Recently, the DSB product has provided by German Aerospace Center (DLR) and Chinese Academy of Sciences (CAS) (Montenbruck et al. 2014; Wang et al. 2016). The between-signal biases are given for more signals on each system, including GPS, GLONASS, Galileo, BDS. Typically, the clock estimation in real-time utilizes the DSB from the previous days. Receiver code biases are frequently incorporated into the receiver clock parameters, while ambiguity parameters can absorb phase delays. Therefore, after linearization, the fundamental observation model for UD clock estimation can be expressed as,

$$\begin{cases} v_{r,P}^{s,G} = \delta t_r^G - \delta t^{s,G} + m_r^{s,G} \cdot Z_r + l_{r,IF,P}^{s,G} \\ v_{r,L}^{s,G} = \delta t_r^G - \delta t^{s,G} + m_r^{s,G} \cdot Z_r + \bar{B}_{r,IF}^{s,G} + l_{r,IF,L}^{s,G} \\ v_{r,P}^{s,R} = \delta t_r^R - \delta t^{s,R} + m_r^{s,R} \cdot Z_r + l_{r,IF,P}^{s,R} \\ v_{r,L}^{s,R} = \delta t_r^R - \delta t^{s,R} + m_r^{s,R} \cdot Z_r + \bar{B}_{r,IF}^{s,R} + l_{r,IF,L}^{s,R} \\ v_{r,P}^{s,E} = \delta t_r^E - \delta t^{s,E} + m_r^{s,E} \cdot Z_r + l_{r,IF,P}^{s,E} \\ v_{r,L}^{s,E} = \delta t_r^E - \delta t^{s,E} + m_r^{s,E} \cdot Z_r + \bar{B}_{r,IF}^{s,E} + l_{r,IF,L}^{s,E} \\ v_{r,P}^{s,C} = \delta t_r^C - \delta t^{s,C} + m_r^{s,C} \cdot Z_r + l_{r,IF,P}^{s,C} \\ v_{r,L}^{s,C} = \delta t_r^C - \delta t^{s,C} + m_r^{s,C} \cdot Z_r + \bar{B}_{r,IF}^{s,C} + l_{r,IF,L}^{s,C} \end{cases} \tag{2.6}$$

where v and l are the post-fit residuals pre-fit residuals of the ionosphere-free observations, subscript P and L are for pseudo-range and carrier phase, respectively; $\delta t_r = c(dt_r + d_r)$ and $\delta t^s = c(dt^s + d^s)$ refer to the receiver and satellite clock; $\bar{B}_r^s = B_r^s + c(dt_r - d^s)$ denotes the float ambiguity in meters.

In GNSS systems that utilize CDMA signals, such as GPS, Galileo, and BDS, the differences among satellites within the same system are minimal due to their shared frequencies. Conversely, biases between satellites from different systems can be considerably significant and require proper handling; this is referred to as Inter-System Biases (ISBs). On the other hand, GLONASS satellites employ FDMA signals with varying frequencies, resulting in noticeable frequency-dependent biases. Therefore, these biases

should be parameterized individually for each satellite, known as Inter-Frequency Biases (IFBs). When GPS time is chosen as the time reference and ISB and IFB are defined in relation to GPS observations, the combined clock estimation models for GPS, GLONASS, BDS, and Galileo can be expressed as,

$$\begin{cases} v_{r,P}^{s,G} = \delta t_r^G - \delta t^{s,G} + m_r^{s,G} \cdot Z_r + l_{r,IF,P}^{s,G} \\ v_{r,L}^{s,G} = \delta t_r^G - \delta t^{s,G} + m_r^{s,G} \cdot Z_r + \bar{B}_{r,IF}^{s,G} + l_{r,IF,L}^{s,G} \\ v_{r,P}^{s,R_k} = \delta t_r^G + IFB_r^{R_k} - \delta t^{s,R_k} + m_r^{s,R_k} \cdot Z_r + l_{r,IF,P}^{s,R_k} \\ v_{r,L}^{s,R_k} = \delta t_r^G + IFB_r^{R_k} - \delta t^{s,R_k} + m_r^{s,R_k} \cdot Z_r + \bar{B}_{r,IF}^{s,R_k} + l_{r,IF,L}^{s,R_k} \\ v_{r,P}^{s,E} = \delta t_r^G + ISB_r^E - \delta t^{s,E} + m_r^{s,E} \cdot Z_r + l_{r,IF,P}^{s,E} \\ v_{r,L}^{s,E} = \delta t_r^G + ISB_r^E - \delta t^{s,E} + m_r^{s,E} \cdot Z_r + \bar{B}_{r,IF}^{s,E} + l_{r,IF,L}^{s,E} \\ v_{r,P}^{s,C} = \delta t_r^G + ISB_r^C - \delta t^{s,C} + m_r^{s,C} \cdot Z_r + l_{r,IF,P}^{s,C} \\ v_{r,L}^{s,C} = \delta t_r^G + ISB_r^C - \delta t^{s,C} + m_r^{s,C} \cdot Z_r + \bar{B}_{r,IF}^{s,C} + l_{r,IF,L}^{s,C} \end{cases} \tag{2.7}$$

where ISB^E and ISB^C represent the ISB parameters of Galileo and BDS satellites; and $IFB_r^{R_k}$ denotes the GLONASS satellite IFB parameters with frequency identity of k related to GPS.

The ISB and IFB parameters can be modeled as constants due to their temporal stability or as random walks to account for possible unexpected variations over time, especially for certain specialized receivers. It is evident that a constant shift in all ISB parameters for a GNSS system can be offset by an equivalent shift in their satellite clocks. Similarly, a shift in all IFBs for a specific GLONASS satellite cannot be distinguished from the satellite clock adjustment. To address the singularity arising from the full correlation between the satellite clocks and ISB/IFB parameters, constraints should be applied. Specifically, the constraint that the sum of all ISB parameters for each individual system equals zero and that the sum of all IFB parameters for an individual GLONASS satellite within a network equal zero should be imposed. Furthermore, to optimize computational efficiency, IFB and ISB values can be corrected using estimates from previous days, taking into account the stability of these estimates.

The key point for the computational efficiency of real time clock estimation is the number of parameters. Assume that n_{sys} is the number of navigation systems which is 4, n_{site} and n_{sat} are stations number and total number of multi-GNSS satellites, respectively, while n_p is the average number of satellites that are tracked at each station and epoch for a single system. This means that for each station there are n_p ambiguities need to be estimated at each epoch. Assuming the numbers of satellites for GPS, GLONASS, Galileo,

and BDS are $n_{sat}^{G} = 32$, $n_{sat}^{G} = 27$, $n_{sat}^{E} = 36$, and $n_{sat}^{C} = 35$, respectively. For GLONASS only ISB is considered. Without loss of generality, it is assumed that $n_{p}^{G} = 12$, $n_{p}^{R} = 8$, $n_{p}^{E} = 10$, $n_{p}^{C} = 15$, while for the GPS-only solution, the total number of parameters at each epoch is $n_{tot} = 14 * n_{site} + 32$, in the case of a four system multi-GNSS solution, $n_{sat}^{all} = 32 + 27 + 36 + 35 = 130$, $n_{p}^{all} = 12 + 8 + 10 + 15 = 45$ and the total number of parameters at each epoch $n_{tot}^{all} = 49 * n_{site} + 130$. In the solution of the satellite clock based on Equation (2.6), all parameters listed in Table 2.1 are going to be estimated simultaneously. From Table 2.1, we can find that most of the parameters to be estimated in the UD model are ambiguity parameters. Taking n_{site}= 100 as an example, in case of multi-GNSS, the ambiguity parameters account for 89.5% of the parameters to be estimated. Therefore, to enhance computational efficiency in real-time clock estimation, it is imperative to tackle the problem of excessive ambiguity parameters first.

Table 2.1 Parameters need to be estimated at each epoch in the UD model

Parameter type	**Parameters number (GPS)**	**Parameters number (Multi-GNSS)**
Receiver clocks and ISB	n_{site}	$n_{sys} \times n_{site}$
Satellite clocks	n_{sat}^{G}	n_{sat}^{all}
Zenith troposphere delay	n_{site}	n_{site}
UD ambiguities	$n_{p}^{G} * n_{site}$	$n_{p}^{all} * n_{site}$
Total (n_{tot})	$(2 + n_{p}^{G}) * n_{site} + n_{sat}^{G}$	$(n_{sys} + 1 + n_{p}^{all}) * n_{site} + n_{sat}^{all}$

2.2.2 Epoch differenced model

Most parameters in the UD model are ambiguities, the number of which increases linearly with the number of satellites and stations. It is clearly the main reason of the heavy computational burden in the clock estimation. The motivation of the Epoch Differenced (ED) model is to eliminate the ambiguity parameters, and consequently reduce the computation load. Since the range biases both ISB/IFB and DSBs/Observable-Specific signal Biases (OSBs) between GPS are rather stable in short time or even over a day (Zhang et al. 2016, Jiang et al. 2023), they can also be considered eliminated. Therefore, the ED observation equations at each epoch can be expressed as,

$$\begin{cases} \Delta v_{r,P}^{s,G} = \Delta\delta t_r^G - \Delta\delta t^{s,G} + \Delta m_r^{s,G} \cdot Z_r + \Delta l_{r,IF,P}^{s,G} \\ \Delta v_{r,L}^{s,G} = \Delta\delta t_r^G - \Delta\delta t^{s,G} + \Delta m_r^{s,G} \cdot Z_r + \Delta l_{r,IF,L}^{s,G} \\ \Delta v_{r,P}^{s,R} = \Delta\delta t_r^G - \Delta\delta t^{s,R} + \Delta m_r^{s,R} \cdot Z_r + \Delta l_{r,IF,P}^{s,R} \\ \Delta v_{r,L}^{s,R} = \Delta\delta t_r^G - \Delta\delta t^{s,R} + \Delta m_r^{s,R} \cdot Z_r + \Delta l_{r,IF,L}^{s,R} \\ \Delta v_{r,P}^{s,E} = \Delta\delta t_r^G - \Delta\delta t^{s,E} + \Delta m_r^{s,E} \cdot Z_r + \Delta l_{r,IF,P}^{s,E} \\ \Delta v_{r,L}^{s,E} = \Delta\delta t_r^G - \Delta\delta t^{s,E} + \Delta m_r^{s,E} \cdot Z_r + \Delta l_{r,IF,L}^{s,E} \\ \Delta v_{r,P}^{s,C} = \Delta\delta t_r^G - \Delta\delta t^{s,C} + \Delta m_r^{s,C} \cdot Z_r + \Delta l_{r,IF,P}^{s,C} \\ \Delta v_{r,L}^{s,C} = \Delta\delta t_r^G - \Delta\delta t^{s,C} + \Delta m_r^{s,C} \cdot Z_r + \Delta l_{r,IF,L}^{s,C} \end{cases} \tag{2.8}$$

where Δ is the difference operator between two adjacent epochs and the meaning of other parameters is the same to the UD model. Since the ambiguity parameters are removed, there are only three types of parameters left in the equation and they have been shown in Table 2.2. It should be noted that the ED zenith troposphere delays cannot be ignored although they are very small, because they have a systematic trend along with time and will bias the estimates if ignored (Bock et al. 2009).

Table 2.2 Parameters to be estimated at each epoch in the ED model

Parameter type	**Parameters number**
Receiver clocks	n_{site}
Satellite clocks	n_{sat}
Zenith troposphere delay	n_{site}
Total (n_{tot})	$2 * n_{site} + n_{sat}^{all}$

Under the same assumption of the number of satellites for each system above, the total number of unknowns is $2 * n_{site} + 32$ and $2 * n_{site} + 130$ for GPS-only and multi-GNSS solutions, respectively. However, it is suggested by Equation (2.8) that only the variation of the clock parameter between epochs, i.e., Δt, can be estimated in the ED model.

To get an intuitive impression on the comparison of the number of unknowns, Figure 2.1 illustrates the variation of the total number of parameters along with the number of stations n_{sta}. Let us take $n_{sta} = 100$ as an example, the total number of unknowns is 232, 330, 1232, 4630 for ED of GPS-only, ED of multi-GNSS, UD of GPS-only and UD of multi-GNSS, respectively. It is concluded that the inclusion of the new satellite systems implies a significant increase in computation load for the UD model, whereas this dilemma can be mitigated by using the ED model.

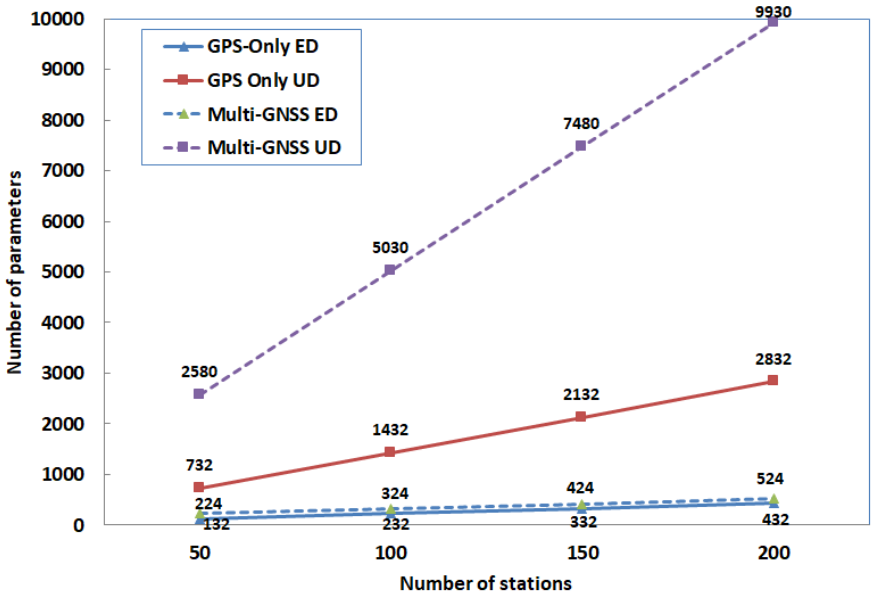

Figure 2.1 Relationship between the number of stations and number of parameters for the solutions using ED or UD model for GPS and multi-GNSS, respectively.

It must be pointed out that with the ED model only epoch-differenced clock biases are estimated. Although they can be accumulated to obtain a type of clock corrections, but the clock corrections of the starting epoch are anyway unknown. By the way, later study shows integer ambiguity fixing in the clock estimation can further improve the accuracy of satellite clocks. Using ED model only there is not chance to fix integer ambiguities. When we compare the UD and ED model, the initial clock biases in the ED model are in principle determined by the range observations. Although the biases have no significant impact on phase observations because of the exist of phase ambiguities, the range modelling will be biased and result in slow convergence at the user-end.

2.2.3 Mixed differenced model

Ge et al. (2012) proposed a Mixed Differenced (MD) model to overcome the problem of the initial clock biases, in which both ED phase observations and the UD pseudo range observations are used together to simultaneously estimate the ED satellite clocks and the initial clock bias for each satellite and receiver. The MD model can be expressed as,

$$\begin{cases} v_{r,P}^{s,G} = \delta t_r^G - \delta t^{s,G} + m_r^{s,G} \cdot Z_r + l_{r,IF,P}^{s,G} \\ \Delta v_{r,L}^{s,G} = \Delta\delta t_r^G - \Delta\delta t^{s,G} + \Delta m_r^{s,G} \cdot Z_r + \Delta l_{r,IF,L}^{s,G} \\ v_{r,P}^{s,R} = \delta t_r^G + ISB_r^R - \delta t^{s,R} + m_r^{s,R} \cdot Z_r + l_{r,IF,P}^{s,R} \\ \Delta v_{r,L}^{s,R} = \Delta\delta t_r^G - \Delta\delta t^{s,R} + \Delta m_r^{s,R} \cdot Z_r + \Delta l_{r,IF,L}^{s,R} \\ v_{r,P}^{s,E} = \delta t_r^G + ISB_r^E - \delta t^{s,E} + m_r^{s,E} \cdot Z_r + l_{r,IF,P}^{s,E} \\ \Delta v_{r,L}^{s,E} = \Delta\delta t_r^G - \Delta\delta t^{s,E} + \Delta m_r^{s,E} \cdot Z_r + \Delta l_{r,IF,L}^{s,E} \\ v_{r,P}^{s,C} = \delta t_r^G + ISB_r^C - \delta t^{s,C} + m_r^{s,C} \cdot Z_r + l_{r,IF,P}^{s,C} \\ \Delta v_{r,L}^{s,C} = \Delta\delta t_r^G - \Delta\delta t^{s,C} + \Delta m_r^{s,C} \cdot Z_r + \Delta l_{r,IF,L}^{s,C} \end{cases} \tag{2.9}$$

In the MD model, the ED carrier phases provide precise clock variations, while the UD pseudo-range determined the initial clock biases. The computational efficiency is very similar the ED model because of the cancellation of all ambiguity parameters. The accuracy of estimated initial clock biases increases along with the time due to the biases and noises in the range observations. Usually, they are stable at the 0.1 ns level after 24 hours.

2.3 Real-time precise point positioning model

The PPP model aligns fundamentally with the clock model described in Equation (2.1), with the primary difference being that the satellite clock is already known, while the position parameters are typically of primary concern.

2.3.1 Standard PPP model

The PPP model requires only dual-frequency observation data from a single receiver. Due to computational efficiency, the IF model is also preferred in real-time PPP, and the observation model can be expressed as,

$$\begin{cases} v_{r,P}^{s,G} = -\mathbf{u}_r^s \cdot \Delta\mathbf{r} + \delta t_r^G + m_r^{s,G} \cdot Z_r + l_{r,IF,P}^{s,G} \\ v_{r,L}^{s,G} = -\mathbf{u}_r^s \cdot \Delta\mathbf{r} + \delta t_r^G + m_r^{s,G} \cdot Z_r + \bar{B}_{r,IF}^{s,G} + l_{r,IF,L}^{s,G} \\ v_{r,P}^{s,R_k} = -\mathbf{u}_r^s \cdot \Delta\mathbf{r} + \delta t_r^G + IFB_r^{R_k} + m_r^{s,R_k} \cdot Z_r + l_{r,IF,P}^{s,R_k} \\ v_{r,L}^{s,R_k} = -\mathbf{u}_r^s \cdot \Delta\mathbf{r} + \delta t_r^G + IFB_r^{R_k} + m_r^{s,R_k} \cdot Z_r + \bar{B}_{r,IF}^{s,R_k} + l_{r,IF,L}^{s,R_k} \\ v_{r,P}^{s,E} = -\mathbf{u}_r^s \cdot \Delta\mathbf{r} + \delta t_r^G + ISB_r^E + m_r^{s,E} \cdot Z_r + l_{r,IF,P}^{s,E} \\ v_{r,L}^{s,E} = -\mathbf{u}_r^s \cdot \Delta\mathbf{r} + \delta t_r^G + ISB_r^E + m_r^{s,E} \cdot Z_r + \bar{B}_{r,IF}^{s,E} + l_{r,IF,L}^{s,E} \\ v_{r,P}^{s,C} = -\mathbf{u}_r^s \cdot \Delta\mathbf{r} + \delta t_r^G + ISB_r^C + m_r^{s,C} \cdot Z_r + l_{r,IF,P}^{s,C} \\ v_{r,L}^{s,C} = -\mathbf{u}_r^s \cdot \Delta\mathbf{r} + \delta t_r^G + ISB_r^C + m_r^{s,C} \cdot Z_r + \bar{B}_{r,IF}^{s,C} + l_{r,IF,L}^{s,C} \end{cases} \tag{2.10}$$

where $\mathbf{u}_r^s$ is the unit vector of the direction from receiver to satellite; $\Delta\mathbf{r}$ denotes the vector of the receiver position increment.

It should be noted that since the computational load of PPP is much less than that of clock estimation, we can also consider using an un-combined approach for PPP calculations. The observation model for the uncombined PPP of frequency f can be expressed as,

$$\begin{cases} v_{r,P}^{s,G} = -\mathbf{u}_r^s \cdot \Delta\mathbf{r} + \delta t_r^G + m_r^{s,G} \cdot Z_r + Ion_{r,f}^{s,G} + l_{r,f,P}^{s,G} \\ v_{r,L}^{s,G} = -\mathbf{u}_r^s \cdot \Delta\mathbf{r} + \delta t_r^G + m_r^{s,G} \cdot Z_r + \bar{B}_{r,f}^{s,G} - Ion_{r,f}^{s,G} + l_{r,f,L}^{s,G} \\ v_{r,P}^{s,R_k} = -\mathbf{u}_r^s \cdot \Delta\mathbf{r} + \delta t_r^G + IFB_r^{R_k} + m_r^{s,R_k} \cdot Z_r + Ion_{r,f}^{s,R} + l_{r,f,P}^{s,R_k} \\ v_{r,L}^{s,R_k} = -\mathbf{u}_r^s \cdot \Delta\mathbf{r} + \delta t_r^G + IFB_r^{R_k} + m_r^{s,R_k} \cdot Z_r + \bar{B}_{r,f}^{s,R_k} - Ion_{r,f}^{s,R} + l_{r,f,L}^{s,R_k} \\ v_{r,P}^{s,E} = -\mathbf{u}_r^s \cdot \Delta\mathbf{r} + \delta t_r^G + ISB_r^E + m_r^{s,E} \cdot Z_r + Ion_{r,f}^{s,E} + l_{r,f,P}^{s,E} \\ v_{r,L}^{s,E} = -\mathbf{u}_r^s \cdot \Delta\mathbf{r} + \delta t_r^G + ISB_r^E + m_r^{s,E} \cdot Z_r + \bar{B}_{r,f}^{s,E} - Ion_{r,f}^{s,E} + l_{r,f,L}^{s,E} \\ v_{r,P}^{s,C} = -\mathbf{u}_r^s \cdot \Delta\mathbf{r} + \delta t_r^G + ISB_r^C + m_r^{s,C} \cdot Z_r + Ion_{r,f}^{s,C} + l_{r,f,P}^{s,C} \\ v_{r,L}^{s,C} = -\mathbf{u}_r^s \cdot \Delta\mathbf{r} + \delta t_r^G + ISB_r^C + m_r^{s,C} \cdot Z_r + \bar{B}_{r,f}^{s,C} - Ion_{r,f}^{s,C} + l_{r,f,L}^{s,C} \end{cases} \tag{2.11}$$

These two models are equivalent for positioning purposes. The uncombined model often provides advantages as it integrates regional augmentation of ionosphere delay more easily. Meanwhile, the IF model is favored for its higher computational efficiency.

2.3.2 PPP with regional augmentation

For both IF or uncombined PPP, we can accurately extract the zenith troposphere delay Z_r from the estimated parameters. In the uncombined PPP model, precise ionosphere information for each satellite can be directly obtained from the parameters. In the IF PPP model, it is first necessary to determine the ambiguity of L_1 or L_2 frequency using the IF ambiguity which will be presented in Section 2.4, and then the ionosphere information can be accurately calculated using the phase equation. Taking using L_1 ambiguity as an example, the ionosphere delay can be extracted using the model,

$$\begin{cases} I_{r,1}^{s,G} = -\mathbf{u}_r^s \cdot \Delta\mathbf{r} + \delta t_r^G + m_r^{s,G} \cdot Z_r + \bar{B}_{r,1}^{s,G} + l_{r,1,L}^{s,G} - v_{r,1,L}^{s,G} \\ I_{r,1}^{s,R} = -\mathbf{u}_r^s \cdot \Delta\mathbf{r} + \delta t_r^G + IFB_r^{R_k} + m_r^{s,R_k} \cdot Z_r + \bar{B}_{r,1}^{s,R_k} + l_{r,1,L}^{s,R_k} - v_{r,1,L}^{s,R_k} \\ I_{r,1}^{s,E} = -\mathbf{u}_r^s \cdot \Delta\mathbf{r} + \delta t_r^G + ISB_r^E + m_r^{s,E} \cdot Z_r + \bar{B}_{r,1}^{s,E} + l_{r,1,L}^{s,E} - v_{r,1,L}^{s,E} \\ I_{r,1}^{s,C} = -\mathbf{u}_r^s \cdot \Delta\mathbf{r} + \delta t_r^G + ISB_r^C + m_r^{s,C} \cdot Z_r + \bar{B}_{r,1}^{s,C} + l_{r,1,L}^{s,C} - v_{r,1,L}^{s,C} \end{cases} \tag{2.12}$$

After accurately extracting ionosphere and troposphere information, considering the spatial correlation of atmosphere delays within the region, we can adopt a strategy of regional atmosphere modeling. This modeling helps us better understand and predict atmosphere changes, which in turn can significantly enhance the performance of PPP clients by using the precise atmosphere information obtained from the models.

A linear interpolation model can be employed to depict the atmosphere corrections derived for small regional scales. In this approach, three or more proximate monitoring stations are chosen as augmenting stations for each monitoring station. The atmosphere delay corrections from these augmenting stations are then interpolated using a linear combination method (Li et al. 2011), as,

$$\sum_{i=1}^{n} \alpha_i = 1, \sum_{i=1}^{n} (\hat{X}_m - \hat{X}_i) = 0, \sum_{i=1}^{n} \alpha_i^2 = Min \tag{2.13}$$

$$\hat{v}_m = \sum_{i=1}^{n} \alpha_i \hat{v}_i \tag{2.14}$$

where n is the number of selected augmenting stations; m and i are indices for the monitoring and the selected augmenting stations, respectively; $\alpha_i$denotes the interpolation coefficient; $\hat{X}_m$ and $\hat{X}_i$ are the station coordinates in the local horizontal plane system; ΔX_{im} and ΔY_{im} are the plane coordinate differences between the user and augmenting reference station; $\hat{v}_i$ is the ionosphere or troposphere delay; $\hat{v}_m$ is the interpolated ionosphere or troposphere delay at the monitoring station.

In regional reference networks characterized by moderate-to-short baselines-typically spanning a few tens of kilometers-interpolated atmosphere delay corrections can attain centimeter-level accuracy. These refined corrections are then applied as stringent constraints on the associated parameters of the user station, with coordinates being dynamically estimated in kinematic mode. When stations r_1 though r_n are chosen to serve as reference stations for deriving corrections at the user station, the constraint on the ionosphere slant delay parameter for a specific satellite s_i is determined by the interpolated correction as,

$$I_{r_m}^{s_i} - \hat{I}_{r_1,r_2\ldots r_n}^{s_i} = w_I, \qquad w_I \sim N(0, \sigma_{w_I}^2) \tag{2.15}$$

and the constraint for the zenith wet delay parameter is defined as,

$$Z_{r_m}^{s_i} - \hat{Z}_{r_1,r_2\ldots r_n}^{s_i} = w_T, \qquad w_T \sim N(0, \sigma_{w_T}^2) \tag{2.16}$$

where $I_{r_m}^{s_i}$ is the slant ionosphere delay from station r_m to satellite s_i; $\hat{I}_{r_1,r_2\ldots r_n}^{s_i}$ denotes the interpolated ionosphere correction; $Z_{r_m}^{s_i}$ is the zenith wet delay for user station r_m , and $\hat{Z}_{r_1,r_2\ldots r_n}^{s_i}$ is the interpolated correction. w_I and w_T represent the discrepancies between the actual and the interpolated atmosphere delay corrections. The statistical behaviors of w_I and w_T are characterized as zero-mean white noise processes, with variances $\sigma_{w_I}^2$ and $\sigma_{w_T}^2$ for the ionosphere and troposphere delays, respectively.

By utilizing regionally augmented atmosphere delay information, the positioning performance of PPP can be significantly improved, especially in terms of reducing

convergence time. Additionally, the use of regional atmosphere data not only enhances the accuracy of positioning but also improves the system's adaptability and stability in variable environments, thereby providing more reliable performance in demanding applications.

2.4 Ambiguity resolution

As discussed in Sections 2.2 and 2.3, high-performance real-time clock estimation and PPP is critically dependent on accurately resolving the ambiguity parameter B. Leveraging the inherent integer nature of N in B can significantly boost performance. In this section, AR approaches in both Double Differenced (DD) and UD mode are introduced. It is important to recognize that the phase IFB of GLONASS varies not only from one receiver to another but also between different siting configurations (antenna and cabling setups). Additionally, when utilizing differential operations between receivers, an IFB might arise among different receiver manufacturers (Liu et al. 2017). The IFB issue is somewhat avoided by deploying a homogeneous receiver network; however, it remains a significant challenge in our study. Therefore, this section exclusively covers ambiguity resolution methods for CDMA signal systems, encompassing GPS, Galileo, and BDS.

2.4.1 Double differenced ambiguity resolution

As shown in Equation (2.1) and (2.5)， only after we get precise N, b_r and b^s, carrier observations can become highly precise range measurements. Before tackling the UPD issue, it is crucial to first resolve the integer characteristic of the IF ambiguity, since both real-time clock estimation and PPP commonly utilize the IF model. Although the IF combination can eliminate the impact of the first-order ionosphere delay effect, it may also compromise the integer property of the ambiguities. To effectively fix the ambiguities, we can represent the IF ambiguity as a combination of WL and NL ambiguities, detailed as,

$$B^s_{r,IF} = f_1 f_2/(f_1^2 - f_2^2) * B^s_{r,WL} + f_1/(f_1 + f_2) * B^s_{r,NL} \tag{2.17}$$

Based on equation (2.5), we can rewrite the above expression as,

$$B^s_{r,IF} = f_1 f_2/(f_1^2 - f_2^2) * (N^s_{r,WL} + b_{r,WL} - b^s_{WL}) + f_1/(f_1 + f_2) * (N^s_{r,NL} + b_{r,NL} - b^s_{NL}) \tag{2.18}$$

The remaining issue is how to handle the impacts of WL and NL UPDs in Equation (2.18). Normally, there are two approaches to addressing the challenges posed by b_r and b^s: one involves their elimination through satellite and station differentials, known as the DD ambiguity fixing method, while the other entails estimating them as parameters using

global or regional networks, known as the UD ambiguity fixing method. In this section, the DD method is introduced first， while the UD method will be discussed in Section 2.4.2.

As is well understood, biases associated with both the satellite and receiver including UPDs are eliminated in the DD ambiguity which regains its integer characteristic. According to Equation (2.18), the DD ambiguity can be expressed as,

$$\nabla\Delta B_{mn,IF}^{ij} = f_1 f_2/(f_1^2 - f_2^2) * \nabla\Delta N_{mn,WL}^{ij} + f_1/(f_1 + f_2) * \nabla\Delta N_{mn,NL}^{ij} \quad (2.19)$$

where i and j represent the two satellites, m and n represent the two stations utilized in DD processing,∇ represents the satellite single difference operator, Δ represents the station single difference operator, thus $\nabla\Delta$ represent the inter-station satellite DD operator.

Resolving ambiguity typically involves a two-step process. First, the WL AR is addressed, followed by the NL AR. The Melbourne-Wübbena (MW) linear combination (Blewitt 1990) is popular for WL AR. This combination is derived using the code and phase measurements at the two corresponding frequencies, which must be the two frequencies used in forming IF observations. It should be noted that the antenna Phase Center Offset (PCO) and Phase Center Variation (PCV) need to be corrected for both the satellite and receiver ends on each frequency. This occurs because the impact on geometry-distance can only be eliminated when PCO/PCV corrections on different observations in cycles are the same. Taking this into account, the MW linear combination is expressed as,

$$\lambda_{WL}^{s} \cdot N_{r,WL}^{s} = (f_1 \cdot P_{r,1}^{s} + f_2 \cdot P_{r,2}^{s})/(f_1 + f_2) - (f_1 \cdot L_{r,1}^{s} - f_2 \cdot L_{r,2}^{s})/(f_1 - f_2) \quad (2.20)$$

where λ_{WL} is WL wavelength, about 86.4 cm for GPS, which can be expressed as,

$$\lambda_{WL}^{s} = c/(f_1 - f_2) \quad (2.21)$$

The UD WL ambiguity can be estimated from the MW combination of Equation (2.20) by filtering or smoothing over time, the DD WL ambiguity $\nabla\Delta N_{mn,WL}^{ij}$ can be generated and to fixed to integer since all systematic errors and UPDs are cancelled. Owing to the long wavelength of the WL ambiguities, they can be directly rounded to the nearest integer according to its float estimate and STD (Dong and Bock 1989) which can also simplified by a fixed the threshold for both the offset to the nearest integer and the STD, typically set to 0.15 cycles, respectively.

Upon successfully resolving the WL ambiguities, the float DD NL ambiguity $\nabla\Delta N_{mn,NL}^{ij}$ can be obtained according using Equation (2.19) as,

$$\nabla\Delta N_{mn,NL}^{ij} = (f_1 + f_2)/f_1 * \nabla\Delta B_{mn,IF}^{ij} - f_2/(f_1 - f_2) * \nabla\Delta N_{mn,WL}^{ij} \quad (2.22)$$

where $\nabla\Delta N_{mn,NL}^{ij}$ can be resolved using methods similar to those employed for $\nabla\Delta N_{mn,WL}^{ij}$. Commonly, the Least-squares AMBiguity Decorrelation Adjustment (LAMBDA) method can be used for resolving the NL ambiguity integers (Teunissen, 1995). After successfully fixing both WL and NL ambiguities, the IF ambiguity can be reconstructed with high precision, as outlined in Equation (2.19). This step involves reintegrating the ambiguity parameters back into the float solution equation, thereby achieving the fixed solution of greater accuracy.

The DD model has widely used for orbit determination, clock estimation, or network RTK, with the advantage of its simplicity. However, its main limitation is that computational demands grow geometrically with the number of observation stations. Moreover, it cannot be used for ambiguity resolution in single-receiver applications, such as PPP. To address this issue, method for fixing UD ambiguities have been developed and are detailed in the following section.

2.4.2 Un-differenced ambiguity resolution

The fundamental difference between UD and DD ambiguity fixing lies in how they handle the UPD component in ambiguity parameter $B_{mn,IF}^{ij}$ in Equation (2.3). Actually, the DD model uses differencing to eliminate the influence of b_r^s and b^s, while the UD method corrects it through estimation to achieve fixed solution. Therefore, the core issue with the UD model is determining how to perform UPD estimation.

For estimating UPD, obtaining the float ambiguities for all stations within a network is necessary. These ambiguities could originate from orbit determination, clock estimation, or PPP. Usually, we try to fix as many parameters as possible in the estimation in order to obtain fast-converged and stable ambiguities. In principle, PPP can provide the fastest and most stable ambiguities, whereas the orbit determination the slowest ones. Of course, inaccurate fixing of parameters may contaminate the estimates.

Assuming a network with n stations, typically more than 15 for regional networks or over 80 for global networks, that tracks m satellites, the UD float ambiguities at each station are estimated as B_i, the observation equation in the form of Equation (2.20) for these ambiguities (Li et al. 2011) can be described as,

$$\begin{bmatrix} B_1 \\ B_2 \\ \vdots \\ \vdots \\ B_n \end{bmatrix} = \begin{bmatrix} I & & & & R_1 & S_1 \\ & I & & O & R_2 & S_2 \\ & & \vdots & & & \\ & O & & I & & \\ & & & & I \quad R_n & S_n \end{bmatrix} \begin{bmatrix} N_1 \\ N_2 \\ \vdots \\ \vdots \\ N_n \\ b_r \\ b^s \end{bmatrix}, \qquad Q \tag{2.23}$$

where R_i and S_i are the coefficient matrices for receiver and satellite UPD respectively; Q is the co-variance matrix of the UD float ambiguities; In matrix R_i one column with all elements is 1 and the others are zero. For matrix S_i each line is one element of -1, the others are zero.

Given that all integer ambiguities are precisely known and one UPD is fixed at zero, other UPDs can be estimated using least squares adjustment. Additionally, for resolving integer ambiguities, only the fractional part of the UPD is necessary, as the integer part can be absorbed by the ambiguity parameters anyway. Consequently, we will not differentiate between UPD and its fractional part in subsequent discussions.

In order to obtain the integer ambiguities in Equation (2.23), an initial UPD set must be available. Assuming the receiver UPD at the first arbitrarily selected station is zero, the nearest integers of the UD ambiguities at this station represent their integer ambiguities, while the fractional parts provide estimates of the corresponding satellite UPD. When this satellite UPD is applied to the common satellites at the next station, the corrected UD ambiguities should exhibit very similar fractional parts. The average of the fractional parts across all common satellites is then the UPD for this receiver. With this UPD, it becomes possible to estimate the UPD for the satellites observed at the station but without UPD estimate yet. By repeating this process across all stations, an approximate UPD for all receivers and satellites can be generated.

Adjusting the UD float ambiguities with the UPDs, they should closely approximate integers, allowing for attempts at ambiguity resolution. By substituting integer ambiguity parameters with their fixed values in Equation (2.20), the remaining parameters can be refined, enhancing the UPD estimates and facilitating the resolution of additional integer ambiguities. The procedure outlined above can be performed iteratively until no further integer ambiguities can be resolved. The UPD from the final iteration provides the necessary information for ambiguity resolution. It should be noted that when estimating UPD, we can also use fixed DD ambiguities to constrain the UPD observation model, thereby enhancing the reliability of UPD estimates, especially for network solutions where

variation of ambiguities along with time is not negligible (Geng et al. 2012, Deng et al. 2022).

In the specific process of UPD calculation, the WL float ambiguities for a satellite-receiver pair for one epoch are first computed using Equation (2.20), followed by estimating the WL UPD using the procedure discussed above, as per Equation (2.23). Subsequently, the IF ambiguities of each satellite at each station are decomposed into a combination of WL and NL ambiguities using Equation (2.18). Since the WL float ambiguities are predominantly derived from pseudo-range observations and are thus inherently noisy, the estimated WL UPD is mainly utilized to fix the WL ambiguities rather than to extract the NL float ambiguities. Consequently, the NL ambiguities inherently include the WL UPD, as noted by Ge et al. (2008). Subsequently, the NL float ambiguities can be expressed as,

$$B_{r,NL}^{ij} = (f_1 + f_2)/f_1 * B_{r,IF}^{ij} - f_2/(f_1 - f_2) * N_{r,WL}^{ij} \tag{2.24}$$

Then, the NL UPDs can be estimated in the same way as for WL UPDs. At this point, the WL and NL UPDs together constitute a complete UPD product, which can be broadcasted to users for ambiguity resolution. For real-time PPP-AR, since the receiver UPD can be eliminated using the inter-satellite single-difference method, only satellite WL and NL UPDs are necessary to provide to PPP users. The process of PPP-AR involves first fixing WL ambiguities, then NL ambiguities, and finally reconstructing IF ambiguities. Further elaboration on this process is omitted here.

If the NL UPDs are not engaged in reconstructing fixed IF ambiguities, they will be absorbed by the clock parameters. In the satellite clock estimation, treating the NL UPDs in this manner will result in satellite clock estimates incorporating fractional parts. Consequently, when using these clock estimates, the satellite UPDs are also eliminated, ensuring that the SD ambiguities between satellites possess integer characteristics. The satellite clock product generated by this strategy is typically referred to as the integer clock product. (Laurichesse et al. 2013).

2.5 Real-time parameter estimation and quality control

Note: The core content of this section has been published by Zuo et al. (2021) and co-authored by myself as one of the contributors. The italicized text represents content from the published paper.

2.5.1 Square root information filter

The SRIF is widely used in spacecraft navigation and system control because of its high numerical reliability and flexibility in parameter processing strategy. The core principle of SRIF is to update the filter state using the Householder orthogonal transformation (Bierman 2006). In this dissertation, the SRIF is employed to estimate real-time clock parameters both in UD and ED models. The basic theory and quantity control strategy of SRIF are detailed included in this section.

2.5.1.1 Principle

Assuming that there are m *observations and* n *parameters at epoch* i*, the observation equations can be expressed in the following simplified form as,*

$$\underset{m\times 1}{l_i} = \underset{m\times n}{H_i} \cdot \underset{n\times 1}{x_i} + \underset{m\times 1}{\varepsilon_i} \tag{2.25}$$

where l_i *is the observation vector;* H_i *is the design matrix;* x_i *is the parameter vector;* ε_i *is the measurement noise with a variance matrix* D_{ε_i}*.*

In GNSS data processing, the parameters can be handled as either deterministic parameters y *or the time varying stochastic parameters* p*, which are usually parameterized as white noise or random-walk process. The random-walk process can be described with the following state equation of the first-order Gauss-Markov process,*

$$p_i = \Phi_{i,i-1} p_{i-1} + w_i \tag{2.26}$$

where $\Phi_{i,i-1}$ *is the state transition matrix and* w_i *is the process noise with* $E(w_i) = 0$ *and* $D(w_i) = D_{w_i}$*.*

In SRIF, the noises in the observation equations and state equations should obey the standard normal distribution, that is $N(0, I)$*.This can be achieved by adapting the corresponding equations. Taking the variance matrix of the observation as example,* D_{ε_i} *can be decomposed as* $D_{\varepsilon_i} = R_{z_i}^{-1} R_{z_i}^{-T}$ *where* R_{z_i} *is an upper triangular matrix and referred as square root information (SRI) of the observations. Then Equation (2.25) can be normalized by multiplying* R_{z_i} *on both sides as,*

$$z_i = A_i x_i + v_i \tag{2.27}$$

where $z_i = R_{z_i} l_i$*,* $A_i = R_{z_i} H_i$*,* $v_i = R_{z_i}^{-1} \varepsilon_i$ *and* $v_i \sim N(0, I)$*.*

The same normalization can be applied to the state equations and with $D_{w_i} = R_{w_i}^{-1} R_{w_i}^{-T}$ *the normalized state equation of Equation (2.26) reads,*

$$R_{w_i} p_i = \bar{\Phi}_{i,i-1} p_{i-1} + \bar{w}_i \tag{2.28}$$

where $\bar{\Phi}_{i,i\text{-}1} = R_{w_i}\Phi_{i,i\text{-}1}$, $\bar{w}_i = R_{w_i}w_i$.

Given the initial value of state parameter x, $E(x_0) = x_0$ *and* $D(x_0)$, *the corresponding initial constraint can be expressed in form of pseudo-observations as,*

$$x = x_0 + w_0 \tag{2.29}$$

with $D(x_0) = {R_0}^{-1}{R_0}^{-T}$, *the normalized observation equations should be,*

$$z_0 = R_0 x + v_0 \tag{2.30}$$

where $z_0 = R_0 x_0$ *and* $v_0 = R_0 w_0$ *with* $v_0 \sim N(0, I)$.

Assuming that the estimation problem includes only the initial information of parameter x *in Equation (2.30) and the observation equations Equation (2.27), the observation equations of the estimation can be summarized as,*

$$\begin{bmatrix} R_0 \\ A \end{bmatrix} x = \begin{bmatrix} z_0 \\ z \end{bmatrix} - \begin{bmatrix} v_0 \\ v \end{bmatrix} \tag{2.31}$$

By applying the Householder orthogonal transformation matrix T *to Equation (2.31) (Bierman 2006), we have:*

$$\begin{bmatrix} \hat{R} \\ 0 \end{bmatrix} x = \begin{bmatrix} \hat{z} \\ e \end{bmatrix} - \begin{bmatrix} \hat{v} \\ v_e \end{bmatrix} \tag{2.32}$$

The least squares solution of Equation (2.32) is to find the parameter vector x *that satisfies:*

$$min \left\| \begin{bmatrix} R_0 \\ A \end{bmatrix} x - \begin{bmatrix} z_0 \\ z \end{bmatrix} \right\|^2 = min \left\| \begin{pmatrix} \hat{R} \\ 0 \end{pmatrix} x - \begin{pmatrix} \hat{z} \\ e \end{pmatrix} \right\|^2 = min \left(\left\| \hat{R}x - \hat{z} \right\|^2 + \|e\|^2 \right) \tag{2.33}$$

where $\hat{R}$ *is also an upper triangular matrix and* e *is the a posteriori residual vector corresponding to the observations* z. *In order to minimize the norm of the residual vector, it is obvious that* x *must satisfy:*

$$\hat{R}x = \hat{z} \tag{2.34}$$

Then, the estimates and their covariance matrix can be derived accordingly. Equation (2.34) can also be used as initial information to be combined with new observations or with state equations for sequential estimation.

2.5.1.2 Time update

In real-time satellite clock estimation, the state vector x *includes the deterministic parameters* y *and the stochastic parameters* p, *of which the former are constant at all epochs such as ambiguities and the latter vary over epochs such as satellite and receiver clocks. After measurement update, Equation (2.34) can be expressed as,*

$$\begin{bmatrix} \hat{R}_{p_{i-1}} & \hat{R}_{p_{i-1}y} \\ 0 & \hat{R}_y \end{bmatrix} \begin{bmatrix} p_{i-1} \\ y \end{bmatrix} = \begin{bmatrix} \hat{z}_{p_{i-1}} \\ \hat{z}_y \end{bmatrix} \tag{2.35}$$

Combining Equation (2.35) and the state equations Equation (2.36) the information matrix for time update reads:

$$\begin{bmatrix} -\bar{\Phi}_{i,i-1} & R_{w_i} & 0 \\ \hat{R}_{p_{i-1}} & 0 & \hat{R}_{p_{i-1}y} \\ 0 & 0 & \hat{R}_y \end{bmatrix} \begin{bmatrix} p_{i-1} \\ p_i \\ y \end{bmatrix} = \begin{bmatrix} z_{w_i} \\ \hat{z}_{p_{i-1}} \\ \hat{z}_y \end{bmatrix} \tag{2.36}$$

Applying the Householder transformation, we obtain the following equation:

$$\begin{bmatrix} \tilde{R}_{p_{i-1}} & \tilde{R}_{p_{i-1}p_i} & 0 \\ 0 & \tilde{R}_{p_i} & \tilde{R}_{p_iy} \\ 0 & 0 & \tilde{R}_y \end{bmatrix} \begin{bmatrix} p_{i-1} \\ p_i \\ y \end{bmatrix} = \begin{bmatrix} \tilde{z}_{w_i} \\ \tilde{z}_{p_i} \\ \tilde{z}_y \end{bmatrix} \tag{2.37}$$

Obviously, the outdated parameters p_{i-1} can be removed from Equation (2.37) and we can predict the state vector by solving the following equation:

$$\begin{bmatrix} \tilde{R}_{p_i} & \tilde{R}_{p_iy} \\ 0 & \tilde{R}_y \end{bmatrix} \begin{bmatrix} p_i \\ y \end{bmatrix} = \begin{bmatrix} \tilde{z}_{p_i} \\ \tilde{z}_y \end{bmatrix} \tag{2.38}$$

After the time update, the state parameters of the current epoch are introduced and Equation (2.38) is ready as initial information for the measurement update.

2.5.1.3 Measurement update

Combining the initial information of Equation (2.38) obtained from the time update and the observation equations at the epoch i of Equation (2.27), the general measurement update can be expressed as,

$$\begin{bmatrix} \tilde{R}_i \\ A_i \end{bmatrix} x_i = \begin{bmatrix} \tilde{z}_i \\ z_i \end{bmatrix} \tag{2.39}$$

Similarly, by applying the Householder orthogonal transformation T to Equation (2.39), we have the observation updated $\tilde{R}_i$ with the residuals as,

$$\begin{bmatrix} \hat{R}_i \\ 0 \end{bmatrix} x_i = \begin{bmatrix} \hat{z}_i \\ e_i \end{bmatrix} \tag{2.40}$$

or shortly as,

$$\hat{R}_i x_i = \hat{z}_i \tag{2.41}$$

The standard full solution with the estimates and their covariance matrix can be derived straightforward as,

$$x_i = \hat{R}_i^{-1}\hat{z}_i$$
$$D_{x_i} = \hat{R}_i^{-1}\hat{R}_i^{-T} \quad (2.42)$$

For the next epoch $i+1$, Equation (2.42) is considered as a prior information the same as Equation (2.35) for time-update, so that sequential processing can be carried out for real-time processing.

2.5.2 Quality control

As described in Section 2.3.1, the e_i in Equation (2.40) is the posterior residual vector automatically generated in the measurement update which can also be used in the quality control. In this section, a new quality control strategy dedicatedly for SRIF is introduced (Zuo et al. 2021).

2.5.2.1 Detection

The first step of the SRIF quality control is to detect the existence of undetected cycle slips or outliers in the observation vector. From Equation (2.40) e_i is the corresponding vector of the posterior residuals at current epoch which theoretically satisfies $e_i \sim N(0, I)$, and the unit weight standard deviation can be calculated as,

$$\hat{\sigma}^2 = e_i^T e_i / m \quad (2.43)$$

where $e_i^T e_i$ follows Chi-square distribution with a freedom of the total number of observations m.

In principle, we can test the individual residuals or the variance of Equation (2.43) to detect whether there is any outlier or not. In this study, we check both of them by constructing the following simple hypothetical test:

$$H_0: |e_i|_{\max} < k_1 \; and \; \hat{\sigma} < k_2 \quad (2.44)$$

where k_1 and k_2 are the thresholds for the residuals and unit weight STD, respectively, and theoretically they can be set according to their stochastic distributions. If H_0 is accepted, there is no problematic observation at this epoch; otherwise, usually at least one outlier exists in the observation vector. It should be noted that the rejection of H_0 can also be caused by the inaccurate modeling of the state parameters. However, in this contribution, we focus on the quality control for observation blunders.

2.5.2.2 Identification

After H_0 is rejected, the second step of the quality control is to find out which observations are contaminated by undetected cycle slips or blunders. The basic idea is to extend the

observation model to consider the possible outliers and then check whether under the extended model the H_0 can be accepted. We first present the approach and then discuss how to select the outlier candidates from thousands of observations.

Assuming that there are n_b possible outliers with the observation index ip(k), k=1,2,…n_b, the function model Equation (2.39) can be extended by introducing the corresponding outlier parameters Δ with the a priori values of zero and variance matrix $D_\Delta = {R_\Delta}^{-1}{R_\Delta}^{-T}$ as,

$$\begin{bmatrix} \tilde{R}_i & O \\ O & R_\Delta \\ A_i & \theta_\Delta \end{bmatrix} \begin{bmatrix} x \\ \Delta \end{bmatrix} = \begin{bmatrix} \tilde{z}_i \\ O \\ z_i \end{bmatrix} \tag{2.45}$$

where θ_Δ is a matrix of $m \times n_b$ with unit vector for all the columns, and for its k-th column only the element at position $ip(k)$ equals to 1. By applying the same orthogonal transformation as that used to Equation (2.39) in the measurement update at epoch i, we can get

$$\begin{bmatrix} \hat{R}_i & \hat{R}_{\Delta,i} \\ O & R_\Delta \\ O & S_{\Delta,i} \end{bmatrix} \begin{bmatrix} x \\ \Delta \end{bmatrix} = \begin{bmatrix} \hat{z}_i \\ O \\ e_i \end{bmatrix} \tag{2.46}$$

with

$$\begin{aligned} \hat{R}_{\Delta,i} &= [\hat{R}_{\Delta_1}, \hat{R}_{\Delta_2}, \cdots \hat{R}_{\Delta_{n_b}}] \\ S_{\Delta,i} &= [S_{\Delta_1}, S_{\Delta_2}, \cdots S_{\Delta_{n_b}}] \end{aligned} \tag{2.47}$$

where $S_{\Delta,i}$ can be considered as the sensitivity matrix of the residual vector e_i with respect to outliers Δ. It means that the magnitude of the un-detected cycle slips or blunders is mapped into a posteriori residual vector through $S_{\Delta,i}$ as,

$$e_i = S_{\Delta,i}\Delta \tag{2.48}$$

It is clear that the residual vector e_i is a combination of outliers and observations noises, so the outlier parameters can be solved from Equation (2.48) using the least square adjustment and the solution reads as

$$\begin{cases} \hat{\Delta} = \left(S_{\Delta,i}^T S_{\Delta,i}\right)^{-1} S_{\Delta,i}^T e_i \\ \hat{v}_\Delta = e_i - S_{\Delta,i}\hat{\Delta} \\ \hat{\sigma}_0 = {\hat{v}_\Delta}^T \hat{v}_\Delta / (m - n_b) \end{cases} \tag{2.49}$$

Then the same hypothetical test H_0 can be conducted with the residuals and STD of the above solution. If the test is passed, the set of outliers should be accepted as the finally

identified ones; otherwise, an additional problematic observation should be selected and added, then the same procedure from Equation (2.45) to (2.49) is repeated until H_0 *is accepted.*

2.5.2.3 Adaptation

Once the outliers are identified, the negative impact of the identified outliers must be removed from the filter. As it is very difficult to down-weight the corresponding observations or to add the same observations but with a negative weight, the function model is extended in the identification step. This is also due to the fact that the most important affect comes from the cycle slips which can only be mitigated by adding an outlier parameter. By the way, the extended function model for the final identified outliers is already achieved with the help of the sensitivity vectors.

Assuming that there are n_b *outliers found at the last step of the identification, the adapted model with the* n_b *outliers is already available, i.e., Equation (2.46) where obviously* $\hat{R}_i$ *is obtained in the measurement update,* $\hat{R}_{\Delta,i}$ *and* $S_{\Delta,i}$ *are already calculated as the sensitivity vectors in the identification step.*

We can simply apply the same type of triangularization to the last n_b *column to achieve the SRI for further data processing:*

$$\begin{bmatrix} \hat{R}_i & \hat{R}_{\Delta,i} \\ 0 & \hat{R}_{\Delta} \\ 0 & 0 \end{bmatrix} \begin{bmatrix} x \\ \Delta \end{bmatrix} = \begin{bmatrix} \hat{z}_i \\ z_{\Delta} \\ \hat{e}_i \end{bmatrix} \tag{2.50}$$

Furthermore, the outlier parameters have to be eliminated sooner. For a range outlier the introduced parameter can be removed directly, whereas the parameter for a phase observation could be either a cycle slip or an outlier. For a cycle slip, it can be replaced by the difference between the ambiguity before and after the cycle slip, then the previous ambiguity will be eliminated and only the new ambiguity is kept.

Assuming the ambiguities are n_1 *and* n_2*, the* $\Delta n_{12} = n_2 - n_1$*, we have* $n_1 = n_2 - \Delta n_{12}$*. Replace* n_1 *in the Equation (2.46) by* $n_2 - \Delta n_{12}$*, we only have to triangularines the last* n_b *columns, otherwise the triangularization must start from the column where* n_1 *is. After the triangularization of the last* n_b *columns, the outlier parameters can be eliminated and the information equation is ready for deriving an adapted solution and for the processing of the next epoch.*

2.6 Real-time GNSS data communication

2.6.1 The networked transport of RTCM via internet protocol

Since 1993, the Receiver Independent Exchange Format (RINEX) has been developed and updated as a standard format for GNSS data exchanging and archiving. With the continuous development of GNSS and communication technology and the great desire for real-time positioning, several data format are developed in order to transmit GNSS data including observations and products in real time and among them the RTCM services messages are currently widely used for this purpose and are further extended from for GPS only to all the existing GNSS systems.

Besides the data format, more important is the data transaction strategy because of the requirement on real-time, information security and accessibility for large-scale users. The NTRIP which is dedicatedly designed for the real-time GNSS data transaction becomes an application-level protocol since 2005. It is a generic and stateless protocol based on the Hypertext Transfer Protocol HTTP/1.1 and has been widely used in the real-time GNSS service (https://igs.bkg.bund.de/root_ftp/NTRIP/documentation/). As an open none-proprietary protocol, the main advantages of NTRIP are as follows:

(1) It is based on the popular HTTP streaming media standard and is relatively easy to implement even if the server and client resources are limited.

(2) The real-time GNSS application based on NTRIP protocol is not limited to a specific coded stream but has the ability to distribute any type of GNSS data.

(3) It has the potential to support large-scale users, and can broadcast hundreds of streams to thousands of users at the same time.

(4) Considering the security requirements, the flow providers and users do not have to contact each other, and the flow is usually not blocked by firewall or proxy server protecting LAN.

(5) Due to the usage of TCP / IP, it can be streamed over any mobile IP network.

A NTRIP system consists of NTRIP sources, NTRIP caster, NTRIP server and NTRIP client. Their relationship is shown in Figure 2.2.

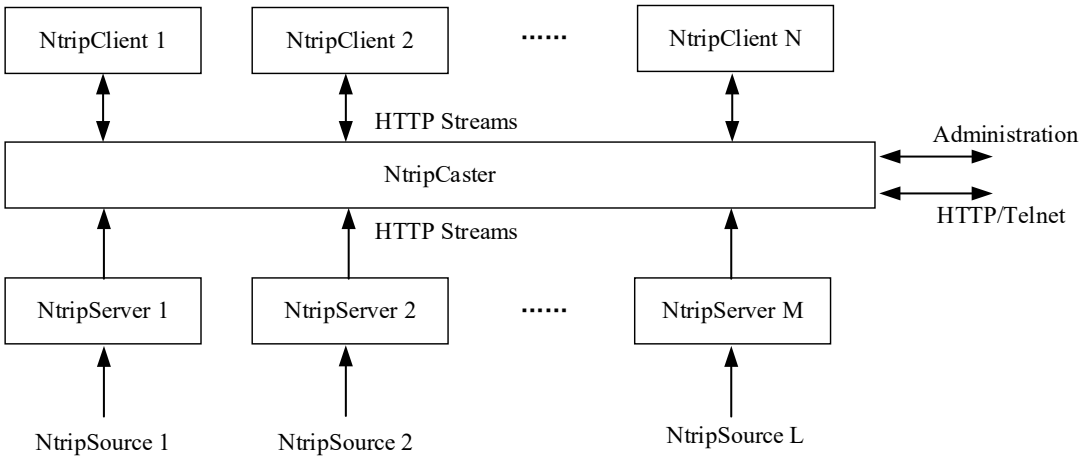

Figure 2.2 Relationship between NRTIP server, caster, and client

The NTRIP sources provide continuous GNSS data as streaming data. A single NTRIP source represents GNSS data referring to a specific location/receiver. The NTRIP server is used to transfer GNSS data of an NTRIP source to the NTRIP caster, where every single NTRIP source needs a unique ID which is called as mount point.

The NTRIP caster is the core component of the NTRIP system. It is an HTTP server which supports a subset of HTTP request / response messages and is tuned to low bandwidth streaming data (from 50 to 500 Bytes per second per stream). It accepts request messages from NTRIP servers or NTRIP clients on a single port and decides whether to receive or send stream data.

Before using TCP / IP connection to transfer GNSS data to NTRIP caster, NTRIP server sends an assignment of the mount point. The server password and mount point information must be defined by the administrator of the NTRIP caster and handed over to the administrators of NTRIP servers.

The NTRIP client is the application layer of the NTRIP system which receives data from NTRIP caster after it has been accepted. Normally, it can be integrated into the GNSS receiver firmware or GNSS positioning client software.

2.6.2 State space representation corrections

The representation of RTCM SC104 standard for GNSS real-time positioning service includes several message types. They are defined along with the GNSS development from GPS only to multi-GNSS and from supporting Observation Space Representation (OSR) to SSR. OSR provides corrections at the observation level, for example, for the differential GNSS and RTK operations using RTCM streams are based on OSR corrections, whereas

SSR provides information on individual error components, such as orbit, clock, troposphere and ionosphere delays, and is a straight forward concept to use actual state parameters for the representation of all the errors sources in GNSS applications (Wübbena et al. 2005). Compared to OSR, only one-way communication is required for SSR and the broadcast frequency is optional according to the time-varying characteristics of corrections. Thus, the bandwidth of SSR is significantly reduced. It also makes use of the satellite independence of troposphere model or the station independence of satellite clock. Currently, SSR corrections have been supported by RTCM standard and all IGS ACs is providing real-time SSR messages at least including orbit and clock corrections.

The satellite orbit corrections in SSR including position and velocity are provided in along, cross, and radial components. These components are defined in the Earth Centered Earth Fixed (ECEF) reference frame reference frame of the broadcast ephemeris. The satellite clock corrections in SSR are referred to the corresponding broadcast ephemeris and are expressed by the polynomial coefficients of bias, velocity, and acceleration. The Issue Of Data (IOD) parameter is an indicator of the SSR information suggesting the related broadcast ephemeris record. In other word, the SSR information can only be applied the broadcast ephemeris with the same IOD to obtain the precise orbit and clock information.

The real-time orbit and clock SSR correction for a satellite at the epoch t_0 can be expressed as,

$$\Delta SSR(t_0, IOD) = (\delta O_r, \delta O_a, \delta O_c, \delta \dot{O}_r, \delta \dot{O}_a, \delta \dot{O}_c, C_0, C_1, C_2) \tag{2.51}$$

where the ΔSSR is the SSR correction vector; δO_r , δO_a and δO_c are the position corrections and $\delta \dot{O}_r$, $\delta \dot{O}_a$ and $\delta \dot{O}_c$ are the velocity corrections of radial, along and cross component, respectively, with respect to the broadcast ephemeris with the same IOD. C_0, $C_1$and C_2 are the polynomial coefficient for correction of broadcast satellite clock in unit of meter. The corrected satellite position $\boldsymbol{r}(t)$ at time t is computed as,

$$\boldsymbol{r}(t) = \boldsymbol{r}_b(t) + (\boldsymbol{e}_r, \boldsymbol{e}_a, \boldsymbol{e}_c)\delta \boldsymbol{O} \tag{2.52}$$

with

$$\delta \boldsymbol{O} = \begin{bmatrix} \delta O_r \\ \delta O_a \\ \delta O_c \end{bmatrix} + \begin{bmatrix} \delta \dot{O}_r \\ \delta \dot{O}_a \\ \delta \dot{O}_c \end{bmatrix} (t - t_0) \tag{2.53}$$

$$\boldsymbol{e}_a = \boldsymbol{v}_b(t)/|\boldsymbol{v}_b(t)| \tag{2.54}$$

$$\boldsymbol{e}_c = \boldsymbol{r}_b(t) \times \boldsymbol{v}_b(t)/|\boldsymbol{r}_b(t) \times \boldsymbol{v}_b(t)| \tag{2.55}$$

$$\boldsymbol{e}_r = \boldsymbol{e}_a \times \boldsymbol{e}_c \tag{2.56}$$

where $\boldsymbol{r}_b(t)$ and $\boldsymbol{v}_b(t)$ are the satellite position and velocity at time t provided by the broadcast ephemeris with IOD.

The corrected satellite clock $dT(t)$ at the time t can also be computed with the SSR correction as,

$$dT(t) = dT_b(t) + [C_0 + C_1(t - t_0) + C_2(t - t_0)^2]/c \tag{2.57}$$

where $dT_b(t)$ is the broadcast satellite clock at time t provided by the broadcast ephemeris; c is the speed of light in vacuum.

2.7 Summary

In this chapter, we mainly introduced the basic theory and method related to real-time clock estimation. First the structure of RTPPS and the importance of real-time clock estimation are explained. Then the up-to-date methods for the observation model of real-time clock estimation are reviewed and their respective characteristics are also concluded. Since SRIF is used for the real-time clock estimation due to its numerical stability and freedom of parameter processing strategy, the model and quality control strategy of SRIF are detailed addressed. Finally, the special concepts in real-time data processing such as NTRIP system and SSR corrections are summarized.

3 Real-time Satellite Clock Rapid Recovery

3.1 Introduction

In the real-time processing mode, normally the estimated parameters must be updated epoch-by-epoch with a certain sampling rate to be able to catch up with the temporary variations of the estimated states. As is well known, the estimating is running forward by a sequential estimator such as recursive least square adjustment, Kalman or SRI filter, therefore there is usually a convergence period during which the state parameters are getting stable. Detailed to real-time clock estimation, a certain length of observations is needed in order to obtain estimates of high accuracy for providing the service, to fulfill the high requirement of real-time precise positioning application. The major reason is the zenith troposphere delays, ambiguity parameters need a long time of observations to be stabilized, so that clock estimates can be accurately separated from them. The convergence of the clock estimation could take dozens of hours for the estimation with a global network depending on the accuracy required which will be experimentally demonstrated hereafter.

In fact, restart of a real-time estimator is inevitable as there could be various reasons requiring and/or causing an estimator interruption. The unexpected reasons include for example estimator crash due to software bugs, computer system or network failures, and power supply problem, while the expected reasons could be estimator software update, computer hardware and software upgrade, significant changes in the tracking network or satellite constellations and as well as the processing strategy. For the later ones, the reason is known in advance and the corresponding restart can be well scheduled.

Considering the fact of the inevitable estimator restart, in order to guarantee the continuity of the service, parallel running estimators in a single data processing and as well as the whole data processing operated in different computational facilities and locations are essential. This is the focus of the following chapter. With the aforesaid precaution of redundant running estimators, however, it is still very important to shorten the convergence time of the start and restart for reducing the risk of service outage. Taking the parallel running of two estimators as example, there will be no usable estimates if the main estimator crashed before the parallel one has not been converged after a restart. It is obvious that the longer the convergence period is, the large is the risk. Hence, to shorten the convergence time to recover the real-time clock products rapidly is also a key point to improve the stability and reliability of the real-time service. Compared to real-time PPP

which takes only about 15-30 minutes to converge to the accuracy of centimeter level, the rapid convergence of real-time clock is more challenging. It must be pointed out that the convergence problem we are investigating here is under the assumption that the GNSS observations are continuous for most of the stations in the real-time network. Otherwise, a long convergence time cannot be avoided due to the discontinuity of the observations at most of the stations.

However, most of the studies focus on the improvement of the accuracy as well as the computational efficiency of real-time clock estimation, whereas the convergence has not yet been taking seriously. For real-time purpose, in principle the convergence relies on the previous information in the form of observations and/or their contribution, for example state information and normal equation at a certain epoch for filter and sequential LSQ, respectively, in order to stabilize ZTD and ambiguity parameters. The basic idea is to start an estimator with enough previous information and then process the backup observations and finally catch up with the processing of the real-time data. It is easy to understand, that the computation efficiency for epoch update is also critical for the reconvergence, although it cannot solve the problem.

In this chapter, a new processing methodology for rapid recovery of multi-GNSS real-time clock estimation is proposed. In the methodology both the historical observations and saved filter information are used to shorten the convergence time of the filter. Multi-threading technology is also employed to control the processing progress, so that a seamless connection between the processing of historical and real-time data is achieved. Based on the observation model and parameter estimation of real-time precise clock estimation in Chapter 2, the algorithm and data-processing strategy of rapid recovery of real-time estimation is emphasized here and the performance of the methodology is analyzed and evaluated.

3.2 Methodology of real-time clock rapid recovery

In the real-time clock estimation, real-time data at the current epoch is received and processed and the estimated clock corrections are sent to a caster and then wait for the data of the next epoch. When the processing crashes or a restart is needed, the filter will start again and real-time observations from the restarting epoch will be processed epoch by epoch as mentioned before. We have to wait for about at least several hours and even to 24 hours in order to provide stable estimates for precise positioning service. This restart

processing procedure is referred to as the conventional restart processing and is illustrated as approach (a) in Figure 3.1 focusing on the used data sources.

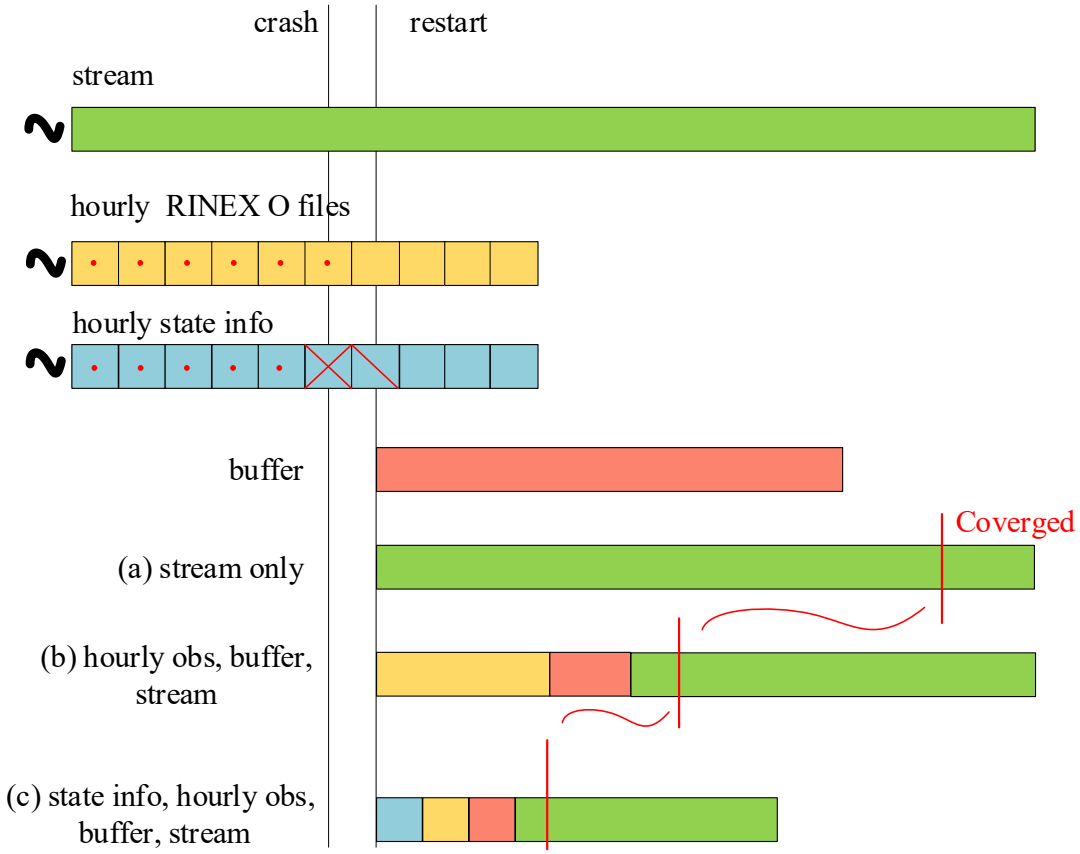

Figure 3.1 Comparison of the three different restart processing strategies: (a) the conventional restart using only real-time data; (b) restart using archived, buffered and real-time observations sequentially; (c) restart beginning with the latest saved filter information, and the archived, buffered and real-time observations sequentially.

The advantages of a conventional restart are obvious, the processing is exactly the same as the initial start with no changes to the estimator or the processing procedure. However, the major disadvantage is also clear that only real-time observations are used in spite that historical observations are available. That means the restart line can only provide suitable products until the observations reaches the length for the convergence no matter how fast is epoch-update of the estimator as it has to wait for observations of the next epoch. Therefore, historical data which can be easily archived in the computer should be used to shorten the convergence time. We can also further storage the filter information to the disk on a regular base, so that it can be used as initial values for restart after an unexpected crash.

In this section, we proposed the method to speed up the convergence of a restarted real-time clock estimation using the historical observations and the regularly saved filter state

information. The first one is to use only historical observations, while the other one considers also the saved filter state information.

3.2.1 Real-time clock recovery leveraging historical observations

In recent years, with the development of global real-time service, there are several public GNSS service organizations broadcasting real-time observations through internet such as IGS, MGEX, GFZ, BKG, US and NRCAN. The providers are distributed in different continents and make a great effort to improve their hardware and software and internet connections for providing continuous and stable real-time streams. Therefore, it is always possible to obtain enough real-time streams for real-time processing, even if a few of the casters could be out of service for a short time. Thus, a premise of the new method is assuming the real-time streams are always available and all the received real-time observations are saved on the disk simultaneously during the real-time processing.

In this new method, we first process historical observations of all the real-time processed stations saved in the form of hourly RINEX files until the latest available ones. Be aware that the files are saved by real-time data receiving software modules running at different locations and can be made available for the restart, i.e., the availability of hourly files is not affected by the crash and the last available hourly file includes the data on the full hour that just ended. As the purpose of using the historical data is to stabilize all the non-epoch-wise parameters instead of providing clock corrections, the sampling interval can be rather large in order to save computation time to catch up with the real-time data processing as soon as possible. For example, if it is processed with a sampling rate of 30 seconds, the computational time can be reduced to one of sixth compared with current real-time processing where clocks are usually updated every 5 seconds. Of course, the impact of sampling rate for historical data on the convergence and accuracy of the estimates will be investigated and optimized later on. Here we call the step of processing historical observations as “file processing step”.

From the end of the last available hourly file to the real-time stream, there is usually a gap because the hourly files are delivered at the last epoch the hour. The smallest gap will be the computational time for processing the last hourly data, whereas the maximum should not be longer than one hour otherwise a new hourly file could be used. In order to cover the gap, the real-time data is buffered in memory while processing the historical data and the buffer is wrapped for just keeping the data of the latest one hour. In other words, there is an overlap of the hourly data and the buffered data, so that data input source can be switch

smoothly. As soon as, the historical data in hourly files are all processed, the buffered observations will be fed into the estimator. During this time period, the buffer must be updated continuously, until the processed epoch time is very close to the actual time, for example within few epochs in the real-time clock update interval, so that the processing can switch to real-time streams as a regular processing line. Here we call this step as "buffer processing step". The function of the buffer step is to link the processing of "file processing" and the upcoming "real-time processing step" seamlessly.

Normally the filter should be already well converged after the buffer data are processed. Then the estimator will switch to the regular real-time processing and the precise real-time service will be available. The data sources employed and the processing procedure of this restart is also illustrated as approach (b) in Figure 3.1. The yellow, orange and green bars represent the computation period for the hourly files, buffered observations and steam data, respectively.

Anyway, the length of the historical data in hourly files should be optimized according to the length of observations for a converged solution, the computation efficiency of the estimator and the processing sampling rate of historical and buffered observations, which plays an important role for shortening the convergence time.

3.2.2 Real-time clock rapid recovery leveraging historical state information

In the above-mentioned restart processing, a certain length of historical data must be processed epoch-by-epoch which is still time consuming. Assume that the epoch update time (without the time waiting for observations) for a multi-GNSS network with about 70 stations is 3 seconds, it will take about 360 seconds for 1 hours historical or buffered data, and 2 hours of computational time if 20 hours of past data is needed for a converged solution, which can be seen from our validation in 3.4. However, most of the data are already processed in the job before a crash or restart and their contribution is expressed in the form of the state information of the estimator. Based on this fact, we propose a further improvement by making use of regularly saved state information of the estimator instead of processing all the long-term observations. When the estimator is running, the state information can be stored on a regular base, for example at the end of each full hour, on the disk as shown in Figure 3.2. In the case of a restart, the latest saved state information can be input as the initial values of the estimator. Therefore, the restart will continue processing historical hourly data starting from the epoch after that of the saved state information. This will shorten the length of the historical and buffered data to be processed from 20 hours to

few hours, and consequently reduce the restart time to within 1 hour. It should be noted that it is much more suitable for the restart with the same processing schema and strategy, otherwise special attention must be paid to the adaption and validation of the historical state information to the new processing strategy. The data sources employed and the processing procedure of this restart is also illustrated in Figure 3.1 as approach (c). Compared with approach (b) in Figure 3.1, a new processing period indicated by grey bar is introduced additionally to approach (c), which means the usage of historically stored state information.

3.3 Multithreaded concurrent system design

To enhance the rapid recovery capabilities of the GNSS real-time clock offset estimation system, we have designed and developed a new method capable of handling information from different data sources in collaboration with the estimator. The system employs multi-threading technology to meet the demands for concurrent processing, and Figure 3.2 illustrates the overall workflow design of the system.

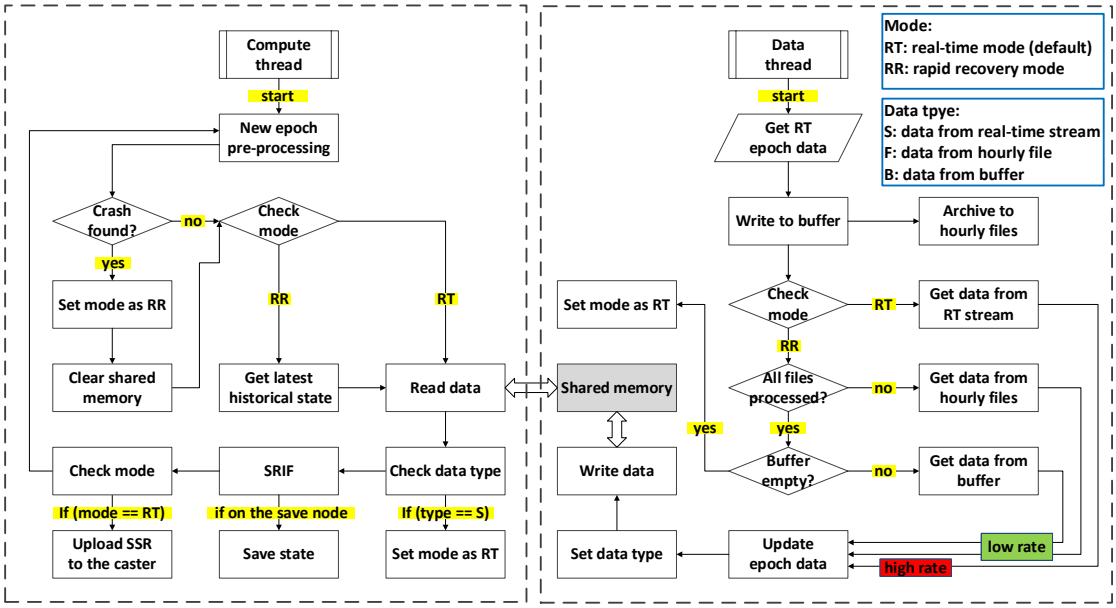

Figure 3.2 Multithreaded workflow for real-time clock rapid recovery

Upon initiation, the compute thread immediately performs preprocessing for the new epoch, which includes preparations for the SRIF update, acquiring ultra-rapid orbit data, broadcast clock, and configuration information. Once an SRIF crash is detected, the compute thread switches to Rapid Recovery (RR) mode. In this mode, the thread first clears the real-time data from shared memory to prepare for loading the historical data required for a swift restart. Meanwhile, when the data thread detects that the system has switched to

RR mode, it automatically starts retrieving data from hourly files or the buffer for use in the next epoch. If no SRIF crash is detected, the thread bypasses the clearing step and continues in Real-Time (RT) mode. In RR mode, an additional step for the compute thread is to acquire the latest historical state before reading data from shared memory. If a historical state is available, it will use this state in conjunction with the data retrieval. Subsequently, the thread determines whether a mode switch is necessary based on the data source type. When data in shared memory is marked as real-time data ("S"), hourly observation file data ("F"), or buffer data ("B"), the thread will perform mode switching as appropriate. If the shared memory data marking indicates that all files and buffer data have been processed, the compute thread switches the mode back to RT to continue providing normal real-time services. The core process of the compute thread is parameter estimation module using SRIF. If SRIF is completed at a save node, the filter state at current epoch will be stored in memory. After SRIF processing is complete, the system checks the mode again; if it is in RT mode, normal service continues, and correction data is uploaded to the NTRIP caster; if not, it does not upload, and the system prepares for the next epoch.

On the data thread side, once real-time single-epoch data is successfully decoded and acquired, it is first written to a temporary buffer. This buffer acts not only as a temporary storage for data but also provides necessary data backup for the stable operation of the system. Subsequently, the thread archives this data hourly, a crucial step for any potential system restarts because it ensures that a historical record of the data is available for recovery at any given time. The process continues with monitoring the current mode: if the system is in RT mode, the data thread continues to process the high sampling rate real-time data stream. Conversely, if the system is in RR mode, the data thread first checks whether all hourly files have been processed. If unprocessed files are found, the thread prioritizes processing these files to ensure data continuity. Once these hourly files are processed, the thread checks the buffer again to determine if there is data pending. At this point, if there is data in the buffer, the thread prepares this data at a lower sampling rate for processing, typically occurring when the system has just switched from RR mode back to RT mode but there is still residual data in the buffer. After all data is processed, the thread switches the mode back to RT and shifts the focus to processing the new real-time data stream, preparing for the next epoch. In the data update step, the data thread performs the task of filtering and optimizing the data; it removes unnecessary information according to system configuration requirements and selects the most critical observational data from the multitude to write into shared memory for timely processing by the compute thread.

In this highly parallel system, the use of shared memory is key to the collaboration between the data thread and the compute thread. Since it stores information crucial to both threads, such as real-time data, historical states, and processing modes, it is imperative to ensure that the data in memory is up-to-date and consistent at all times. To achieve this, we have implemented a read-write lock mechanism to manage access to shared memory. This type of lock allows multiple threads to read data simultaneously, but only one thread can write at any moment. This ensures that when the data thread is updating shared memory, the compute thread is not reading from the same memory area, thus preventing potential data races and inconsistencies. Furthermore, the processing mode variable is a global variable designed as a bridge for communication between threads. Since changes in mode affect the behavior of the entire system, proper management of access to this variable is crucial. When the data thread needs to update the mode, it first obtains a write lock to ensure no other threads are reading or writing the variable. This control mechanism prevents concurrent write operations, ensuring the integrity and accuracy of the mode variable at any time. This strict synchronization mechanism not only guarantees the stable operation of the system but also enhances the speed of system recovery and processing efficiency. Lastly, considering the real-time requirements of the system, we have also set a timeout mechanism for read and write operations in shared memory. If the compute thread cannot obtain the lock within the specified time, it will record a timeout message and take appropriate contingency measures, such as continuing processing using the latest historical data, to ensure that the system's continuity is not interrupted. These carefully designed concurrency control measures ensure the efficient and stable operation of the GNSS real-time clock offset estimation system in a multi-threaded environment.

3.4 Validation and results

3.4.1 Overview

In this section, three experiments are designed to validate the impact of the length of historical data, the impact of sampling rate for processing historical / buffered data, and the advantage of using historical state information. The Position and Navigation Data Analyst (PANDA) software package (Liu and Ge, 2003; Shi et al. 2008) is used as the tool for real-time data processing in this study. Based on the theory above, we have implemented the method into the PANDA software. The BKG NTRIP Client (BNC) (Stürze et al. 2016) software is used to receive global real-time streams from IGS NTRIP caster. The ultra-

rapid orbits are predicted every three hours and fixed as known. The real-time observations will be written into the shared memory directly for the processing by the estimator SRIF, and simultaneously saved into hourly files and buffered in memory.

A global multi-GNSS network comprising 70 stations all with real-time streams are employed in the experiments. The distribution of real-time stations is shown in Figure 3.3. We try to ensure the stations are globally well-distributed and most of the streams are stable enough.

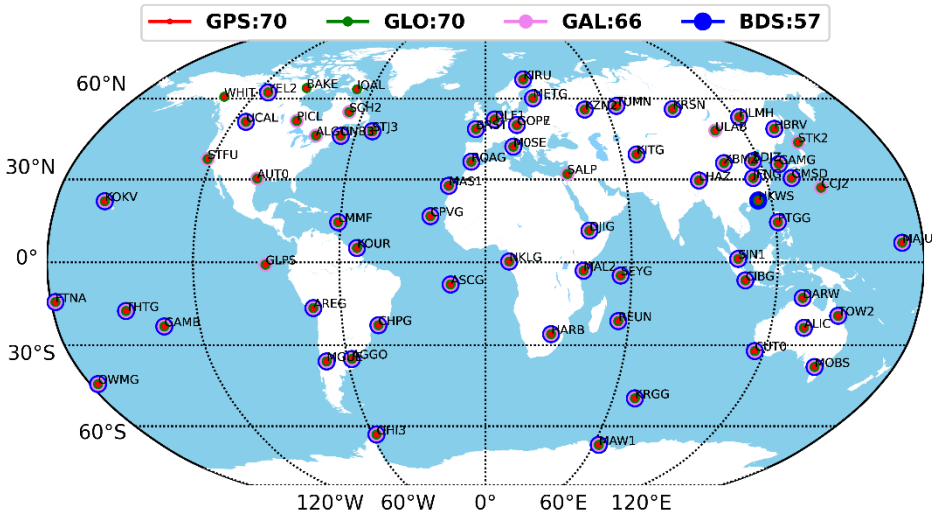

Figure 3.3 the distribution of stations for the multi-GNSS real-time clock estimation

The data processing strategy is shown in Table 3.1. To evaluate and analyze the performance of various strategies on the same dataset, the following experiments employ a simulated real-time processing approach. The data used in the experiment are all recorded after being received in real time. The primary reason for adopting this approach is to facilitate the repeated processing and comparison of data.

Table 3.1 Data processing strategy involved in clock estimation.

Model/Method	
Measurement model	
Observation	Ionosphere-free combinations of code and phase measurements
Sample rate	UD 20s / ED 5s
Elevation cutoff angle	7°
Weighting	A priori precision of 1 cm and 1 m for ionosphere free phase and code, respectively, 1 for elevation > 30° otherwise 2*sin(elevation) (Gendt et al. 2006)
Correction model	

Receiver phase center	igs14.atx PCO and PCV of Galileo and BDS are corrected as GPS
Satellite phase center	igs14.atx
Phase wind up	Corrected (Wu et al. 1993)
Troposphere a priori model	Saastamoinen model for wet and dry hydrostatic delay with Global Mapping Function (GMF) mapping functions without gradient model (Boehm et al. 2006)
Solid Earth tides	IERS Conventions 2010 (Gendt et al. 2006)
Solid Earth pole tides	IERS Conventions 2010
Ocean tides	IERS Conventions 2010
Relativistic effects	IERS Conventions 2010
Parameterization	
Station coordinate	Fixed (from Solution INdependent EXchange (SINEX) file or by Position and PANDA GPS-only PPP weekly solutions)
Satellite orbit	Fixed (from predicted orbit)
Receiver clocks	White noise with a unit weight variance of 9000 m
Satellite clocks	White noise with a unit weight variance of 5000 m
Ambiguity	Estimated as constant parameters and re-initialized if a cycle slip, loss of lock and other data disruption occurs
Troposphere	Piecewise constant zenith delay for each station every 2 hours with a constraint of 2 cm/√h
ISB	Estimated as constant
IFB	Estimated in the orbit determination and corrected as a constant
Adjustment method	SRIF

3.4.2 Influences of historical data length

The purpose of this experiment is to analyze the influence of the length of historical observations on the performance of rapid clock restart. Obviously, what we concern most is how long of the historical data is needed in order to obtain a converged estimation and how accurate are the clock estimates after the restart procedure is finished. In the experiment, historical observations of the latest 0 to 36 hours are tested. It should be noted that the historical observations in this experiment means all observations in files and buffer. The processing interval for both preprocessing and observation update in the filter is set to 30 seconds.

Figure 3.4 shows the relationship between the length of observations and the time consuming of the restart. The obvious linear relationship is because the processing time depends on the number of epochs and the constant epoch update time. On average, it takes about 4.5 minutes to process 1 hour of historical data. For example, in case of using 24

hours of historical observations, it needs about 109 minutes to process all data in the files and buffer, and 160 minutes for using 36 hours of historical observations.

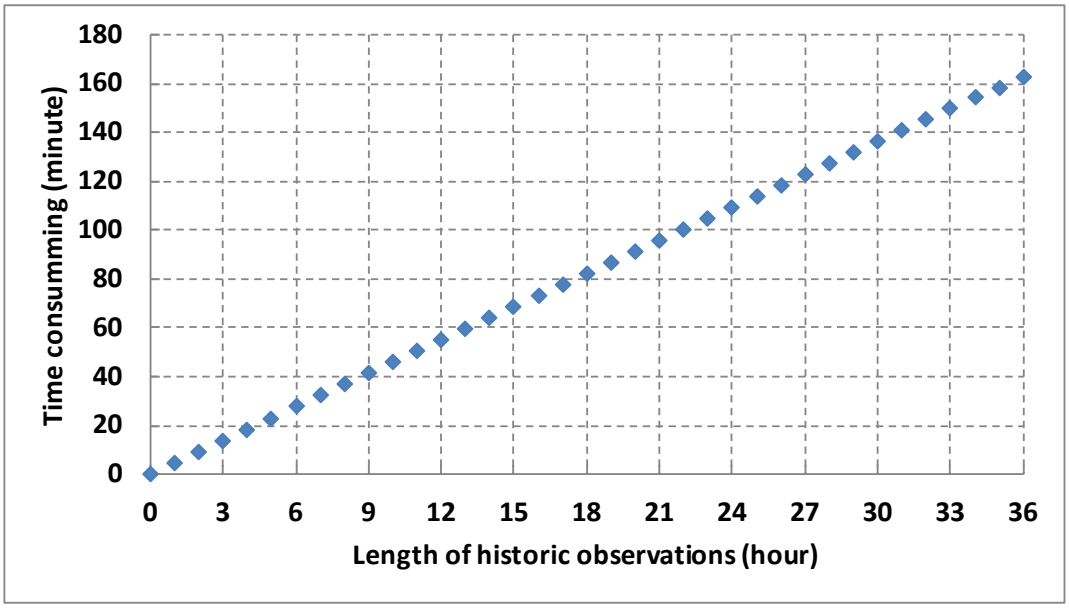

Figure 3.4 Relationship between the length of historical observation and computational time

In the test of clock accuracy following a restart, we initially assumed the real-time clock estimation process had crashed, triggering the rapid clock recovery process. As illustrated in Figure 3.4, even though the system is required to process up to 36 hours of historical data, it manages to successfully complete the restart within 3 hours. This indicates that, after 3 hours, the clock estimation processes for all experimental groups have transitioned to real-time mode. Consequently, we select the real-time clock data from the 3-hour period following the initial 3 hours to assess the accuracy of the real-time clock under various scenarios after a rapid restart. In other words, the real-time clock from the 3rd to the 6th hour is used for accuracy analysis. The results are compared to the GFZ multi-GNSS rapid products (GBM), which are supposed to have the best quality among the existing multi-GNSS products (Deng et al. 2016). Figure 3.5 shows the relationship between the length of the historical observations used and the accuracy of the real-time clocks. The sub figure (a), (b), (c), (d), (e) in Figure 3.5 means the results of GPS, GLONASS, Galileo, BDS MEO/IGSO and BDS GEO satellites, respectively. The blue bars in Figure 3.5 denote the average STD of the clock difference compared with the GBM products. The orbit differences in radial direction are removed in the comparison. The red dashed line in Figure 3.5 refers to the last result of the experiment (observation length = 36 hours) as a reference.

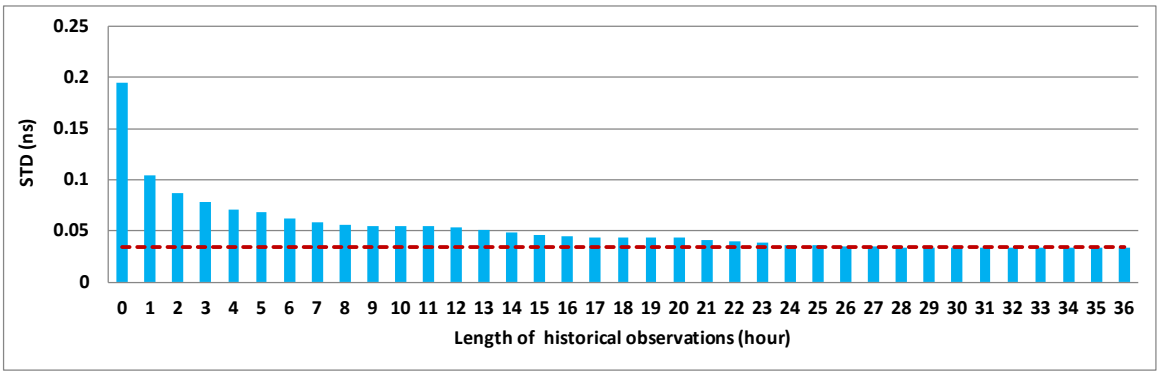

(a) GPS satellites

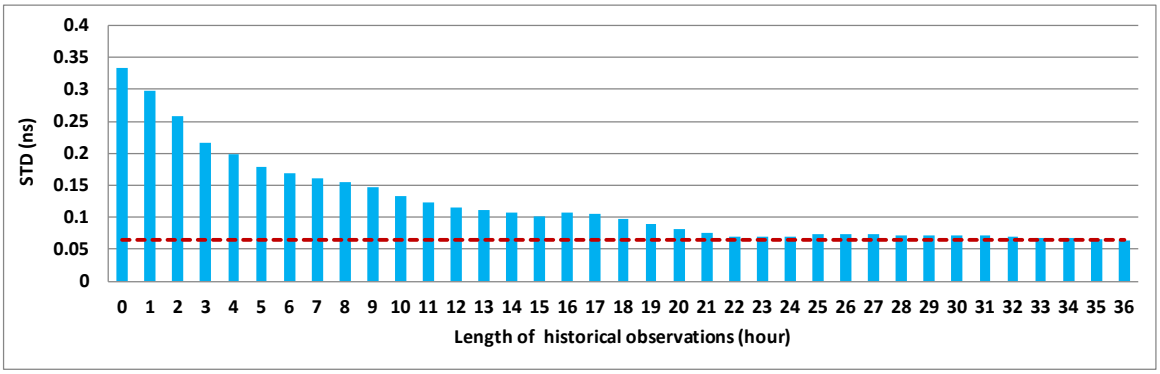

(b) GLONASS satellites

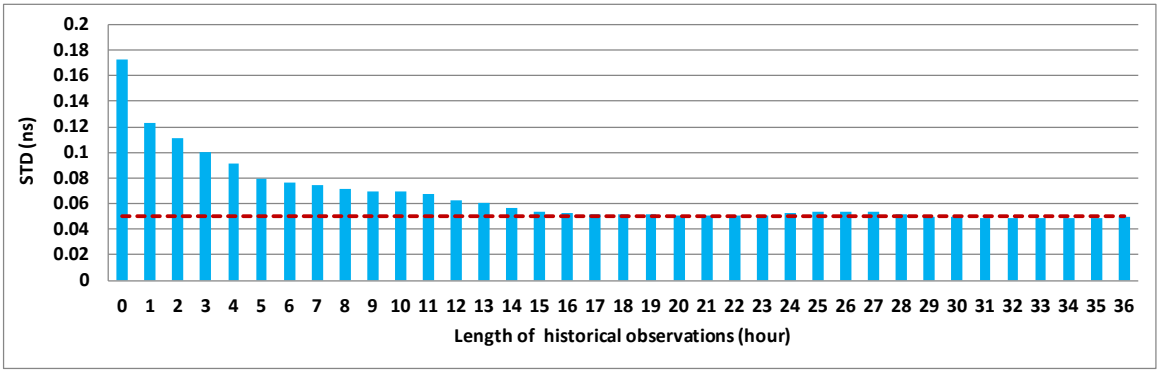

(c) Galileo satellites

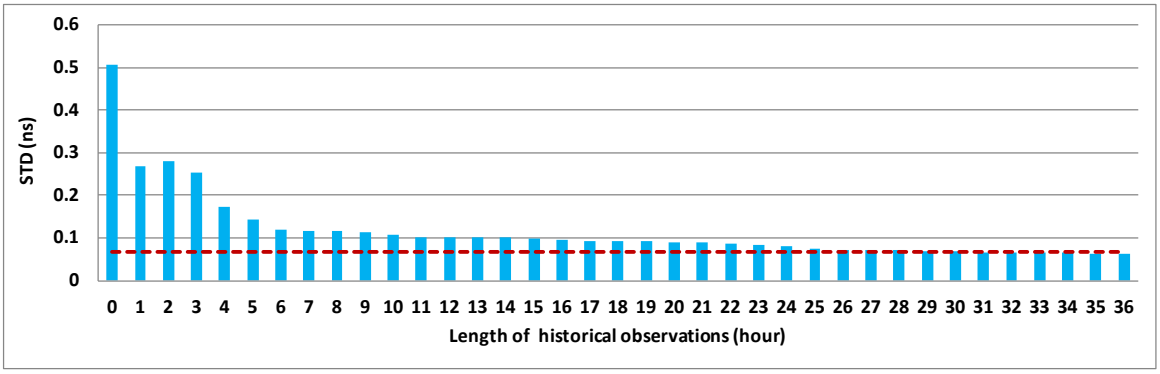

(d) BDS MEO and IGSO satellites

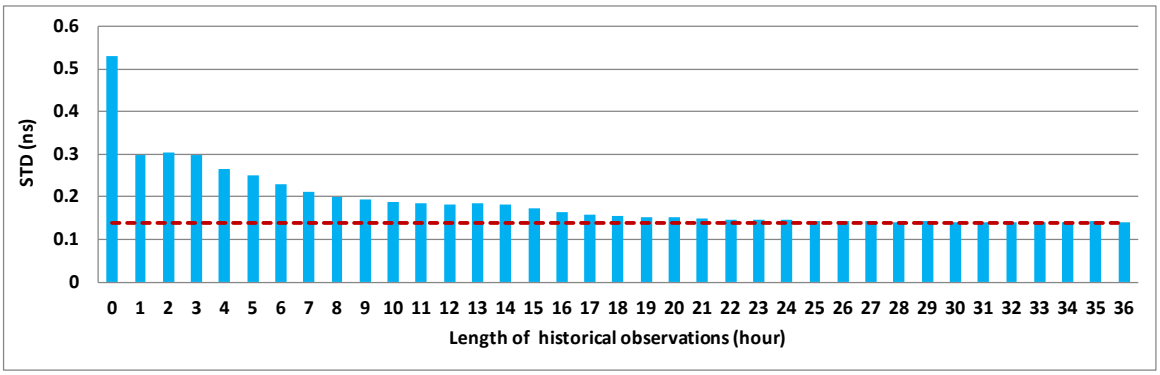

(e) BDS GEO satellites

Figure 3.5 Relationship between observation length and accuracy of estimated clocks compared with the GFZ GBM products

As shown in Figure 3.5, normally the longer the length of observations used, the higher accuracy of the clock estimates can be achieved. However, with the increase of observation length, the significance of the accuracy improvement is diminishing. For all systems, when the historical observation is longer than 24 hours, the further improvement is hardly visible. For example, in the case of using 24-hour historical observations, the accuracy of the clock for GPS, GLONASS, Galileo and BDS IGSO/MEO and BDS GEO satellites are 0.036 ns, 0.070 ns, 0.053 ns, 0.080 ns and 0.146 ns, respectively, while similar accuracies of 0.034 ns, 0.064 ns, 0.050 ns, 0.064 ns and 0.140 ns for the corresponding systems/satellite types for using 36 hours are achieved. Compared among the systems, the convergence for Galileo and BDS GEO satellites is faster than the others in this experiment, about 16 hours for Galileo and 18 hours for BDS GEO satellites is enough to reach a stable solution.

Considering that using longer historical observations requires more computation time, we need to balance the computational efficiency and accuracy. The selection of the length of historical observations should be determined according to actual requirements. If clocks of higher accuracy are required, using longer observations is suggested. If a faster restart is needed, better to use observations of appropriate length to recover the service as soon as possible.

3.4.3 Influences of historical data sampling rates

Since the computation time for each epoch is almost a constant, the total computation time depends linearly on the number of epochs to be processed as shown in Figure 3.6. From the study of the previous section that a certain length of historical observation is required for a converged restart, one possibility to reduce the processing time is to process the

observations with a larger sampling interval. In this experiment, historical observations of the latest 24 hours are used and the processing configuration is the same as in the experiment in 3.4.2 except that the observation intervals from 30 seconds to 300 seconds with an increment of 30 seconds are tested in order to evaluate the relationship between the quality of clock estimates and the processing interval.

Figure 3.6 shows the relationship between the time consuming and sampling intervals. Obviously, the time consuming is reduced with the increase of sampling interval, but the variety is not linear. However, only when the value of sampling interval is small, increasing the sampling interval can significantly reduce the computing time. For example, when the sampling interval is changed from 30 seconds to 60 seconds, the computing time decreases about 1/3. Changing the sampling rate from 150 seconds to 300 seconds reduces the number of epochs processed to half of the former one, however, the computing time decreases only about 1/5. The major reason is that although the data processing interval is enlarged, the pre-processing and parameter elimination are still needed. Especially the number of integer ambiguities will not be affected by the sampling interval and their elimination time will not change very much.

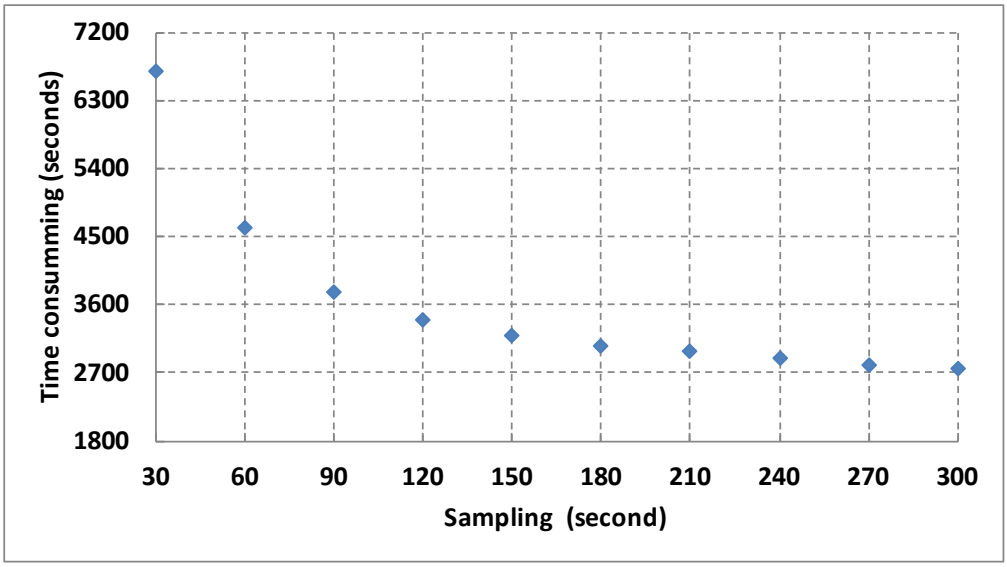

Figure 3.6 Relationship between sampling rate and time consuming using 24-hour historical data

Figure 3.7 shows the relationship between sampling interval and the clock accuracy after the rapid recovery procedure. the results of GPS, GLONASS, Galileo, BDS MEO/IGSO and BDS GEO satellites are illustrated in sub-figures (a), (b), (c), (d), (e) in Figure 3.7, respectively. The red dashed line is the fitted trend line for all results the

corresponding functions and the square of the fitting related coefficient is shown in the upper left of each sub-figure.

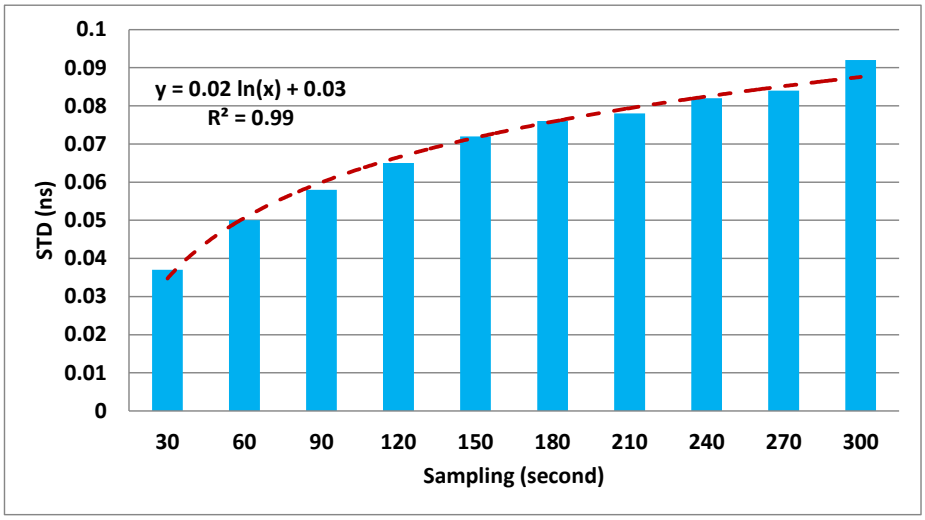

(a) GPS satellites

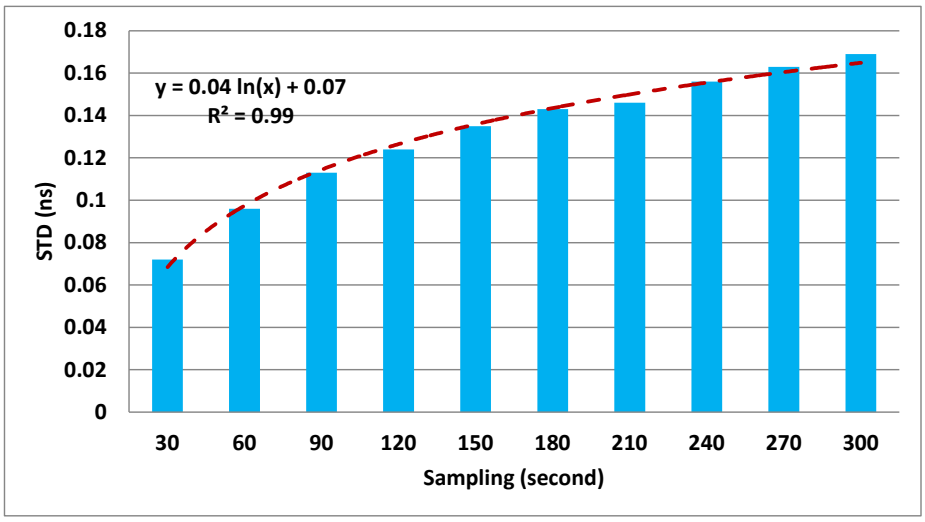

(b) GLONASS satellites

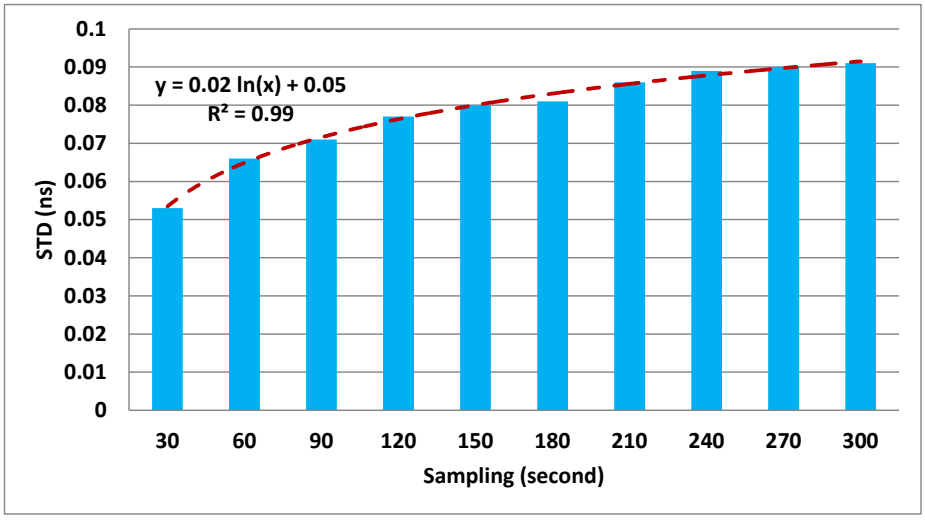

(c) Galileo satellites

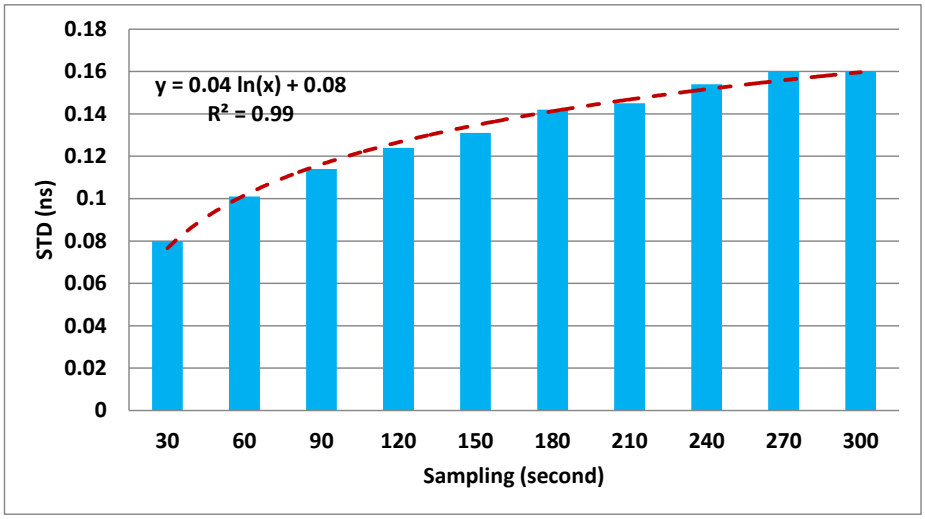

(d) BDS IGSO and MEO satellites

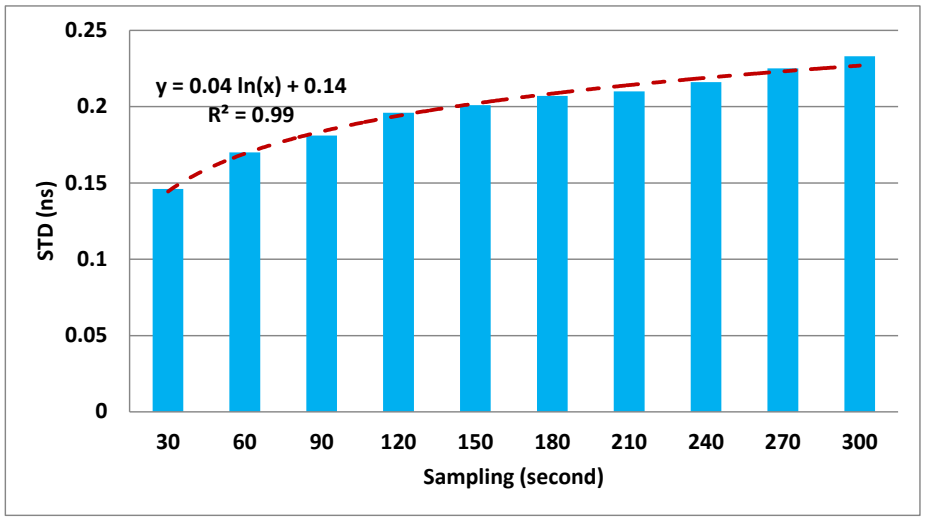

(e) BDS GEO satellites

Figure 3.7 Relationship between sampling and accuracy compared to GBM products

It can be observed that the change in accuracy is highly correlated with the logarithmic function, with a correlation coefficient greater than 0.99. With the increase of sampling interval, the clock accuracy shows a slowly decreasing trend. Considering both accuracy and computational efficiency, set sampling to 60 seconds should be the optimized choice.

3.4.4 The benefits of leveraging historical state information

This experiment aims to evaluate the effectiveness of rapid recovery techniques using historical state information for data processing. In this setup, we periodically save the state information of the filter to disk every hour. In the event of an estimator crash, the monitoring system automatically retrieves the closest saved filter state information to serve as the initial value for the restarted filter. Subsequently, historical observations recorded

after the timestamp of the saved state information are processed in accordance with the methodology outlined in Section 3.2.

To assess the algorithm's performance, the clock estimation process is initially allowed to operate until achieving stability. Thereafter, the following 24 hours are designated as the timeframe for conducting restart tests. The specific experimental arrangement involves manually interrupting the clock process, then running it for 2 hours, followed by a 2-hour pause. This cycle is repeated throughout the duration. Within this 24-hour period, a total of 6 interrupt-restart test cycles are executed. In the experimental setup, the filter begins recording state information from 2:00, logging every 4 hours. This means that during each rapid restart, we can only access the most recent historical state information from 2 hours ago. In practical applications, the interval for recording filter state is typically less than 2 hours. The purpose of this configuration in the experiment is to test the performance under less favorable conditions. The experiment utilized two different strategies for comparative analysis. Strategy (a) relies on normal real-time clock estimation results using only real-time observations, while strategy (b) utilizes historical states and observations to accelerate the convergence of clock estimation. In accordance with the suggestions derived from the findings in Section 3.4.3, the sampling interval for the analysis of historical data is determined to be 60 seconds.

Figure 3.8(a) and 3.8(b) show the time series of the clock differences between the results and the GBM products using strategy (a) and strategy (b), respectively. Figure 3.8(a) clearly illustrates that clock processes often exhibit marked instability after a crash and the following restart. The results displayed in Figure 3.8(b) represent the converged clock series after the processing of both hourly files and buffered data is completed. Conversely, as demonstrated by Figure 3.8(b), the adoption of a rapid recovery strategy that leverages historical states and observations enables the clock difference series to directly achieve a converged state.

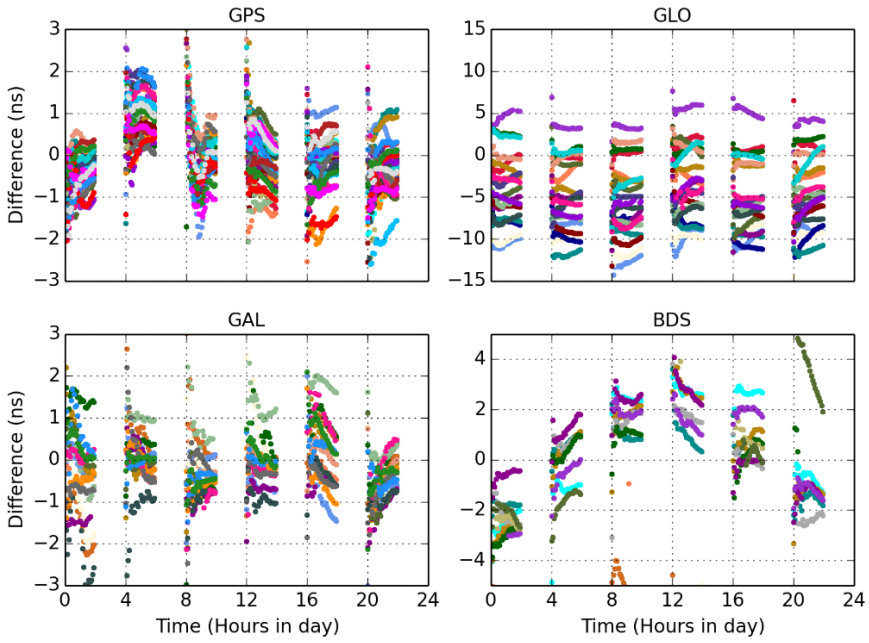

(a) The result of a direct restart using only real-time observations

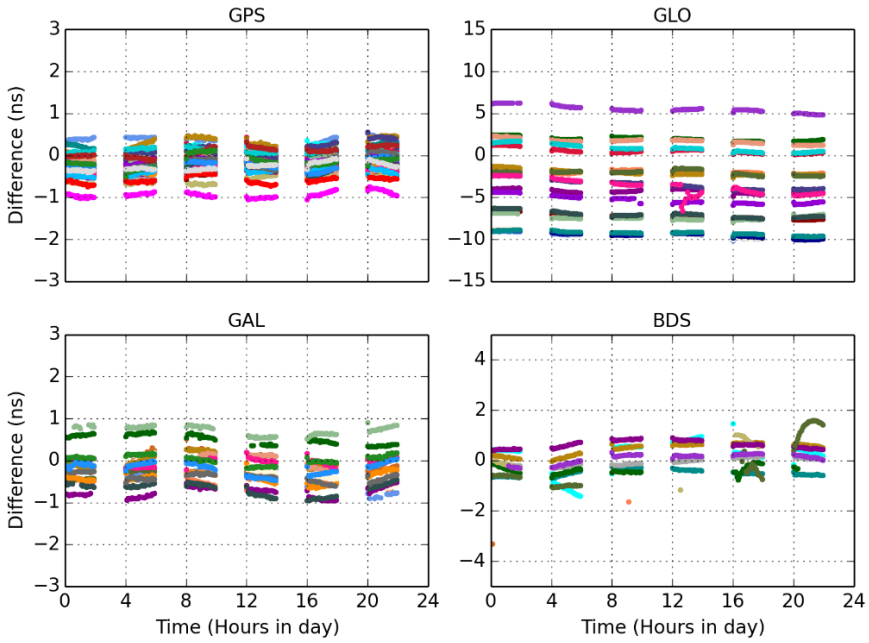

(b) The result of rapid recovery using real-time and achieved observations along with the historical filter states

Figure 3.8 Clock difference series in comparison with GBM products

Aligned with Figure 3.8, Figure 3.9 showcases the accuracy of estimated clock using two strategies. The STD of clock shown in Figure 3.9 (a) stands at 0.11ns for GPS, 0.37ns for GLONASS, 0.14ns for Galileo, 0.17ns for BDS MEO/IGSO, and 0.82ns for BDS GEO

satellites. These results are significantly more favorable than those observed in Figure 3.9 (b).

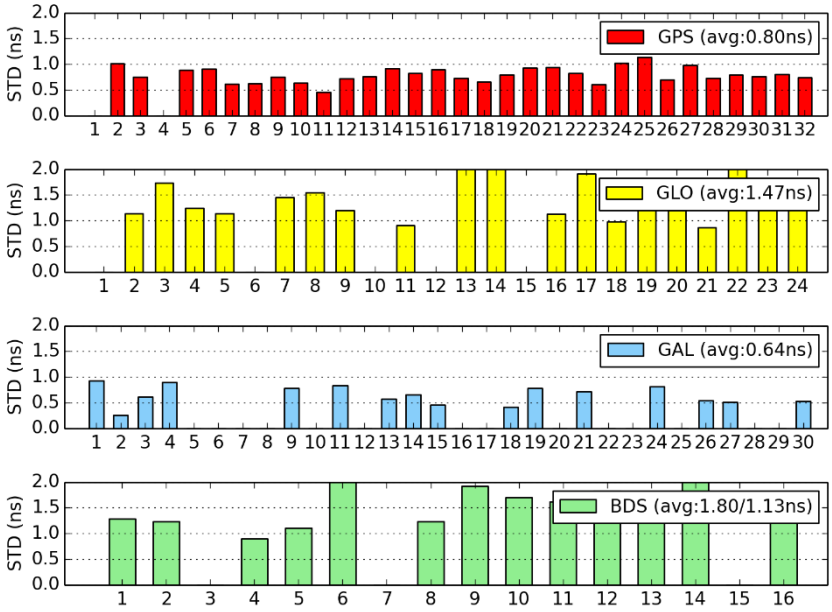

(a) The result of a direct restart using only real-time observations

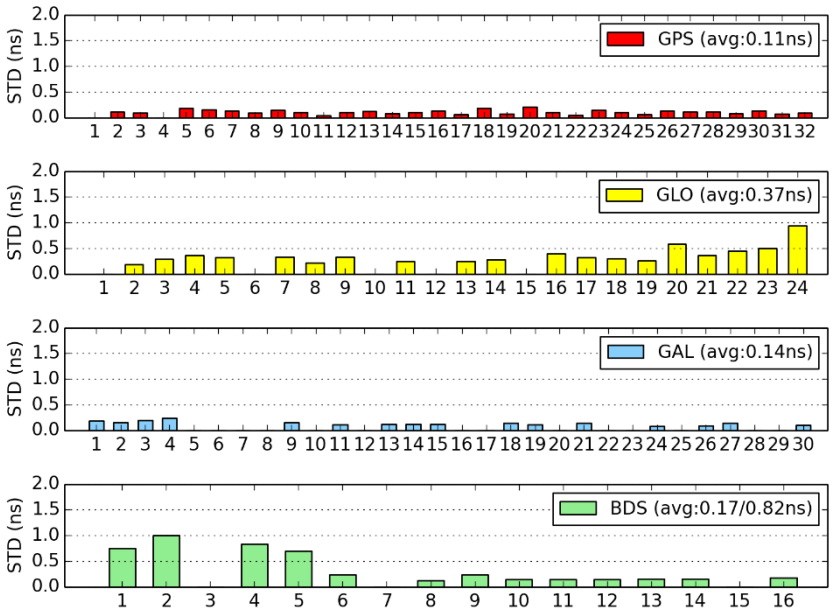

(b) The result of rapid recovery using real-time and achieved observations along with the historical filter states

Figure 3.9 Clock STD in comparison with GBM products

By utilizing historical states, we no longer need to worry about accuracy issues during the filter's convergence process. This strategy essentially extends the filter's historical states, ensuring continuity and enabling the filter to immediately enter a state of convergence upon

restart. The only factor affecting the speed of service restoration is when we can commence broadcasting real-time products at a high sampling rate. As depicted in Figure 3.4, there is a strict linear relationship between data processing time and the number of epochs processed. For instance, in this case, it takes approximately 2.25 seconds to process each epoch. Therefore, the time required to resume broadcasting real-time products with a high sampling rate is entirely dependent on the time difference between the moment the system crashed and the point when the latest historical state information was saved. In this example, with a 2-hour gap between the system crash and the last historical state snapshot, and setting the sampling interval at 60 seconds, we need to process 120 epochs, which altogether takes around 270 seconds. Additionally, processing the 5 epochs accumulated in the buffer during these 270 seconds requires an extra 11.25 seconds. Once these steps are completed, real-time service can be resumed. This means that even if the clock estimation process crashes and does not restart for up to 2 hours, we can still resume real-time service in less than 5 minutes, significantly enhancing the system's reliability.

3.5 Summary

In this chapter, several approaches for rapid convergence of real-time clock estimation are proposed in order to improve the robustness of the real-time precise positioning service. The core idea of these approaches is to use historical observations processed in a large sampling rate and saved state information to shorten the convergence time and to smoothly transfer the processing from historical data to real-time stream to a regular clock estimating line.

Multi-threading technology is used to joint these steps together seamlessly in the design of the real-time service system. All algorithms are realized based on the PANDA software package. The performance of the rapid clock restart methodology is evaluated.

The relationship between the length of historical observations and the computation time is investigated and confirmed their linear correlation. On average, it takes about 4.5 minutes to process one hours' historical observations using 70 stations with the processing interval of 30 seconds, i.e., we need about 109 minutes for a restart using 24 hours' historical observations. The accuracy of the clock estimates after a converged restart is indeed improved with the increased length of historical observations. However, the improvement dims if the length of historical data is longer than a certain value for example 24 hours Among the systems, for Galileo and BDS GEO satellites, the convergence of the clock estimation is faster than the others, about 16 hours for Galileo and 18 hours for BDS

GEO satellites. In addition, the time consuming will be further shorten if we enlarge the interval of adjustment, but the accuracy of the clocks becomes slowly worse with the increase of processing sampling. Thus, a suitable selection of adjustment interval is important to balance the accuracy and the computational efficiency.

Utilizing historical filter state information is a practical strategy that involves saving this data periodically. By keeping these historical states during regular operations and using them for any restart, we can notably decrease the downtime. According to the results in Section 3.4.4, even if the clock estimation process encounters a crash and is offline for up to 2 hours, we are capable of restoring real-time service in less than 5 minutes. This method significantly reduces service interruptions, thereby improving the system's reliability and efficiency in real-world applications.

4 Decentralized Real-time Satellite Clock Estimation

Note: This chapter introduces a decentralized method for real-time clock estimation, which has been published in (Jiang et al. 2019). The italicized text represents content from the published paper.

4.1 Introduction

Though the quality of the IGS precise clock products has been improved largely since 1994, to provide real-time satellite clocks of high stability, normally to be updated within 5 seconds, is still full of challenges. First, the heavy computational burden against the requirement on high update rate and involvement of more stations and multi-constellation satellites is one of the crucial issues. The failure of product update will directly lead to the lack or delay of products. In addition, clock estimation in single-process mode is still unreliable. Although the method proposed in Chapter 3 solves the problem of rapid clock restart, it still has limitations. The method fails when the observations are interrupted such as events caused by power off or hardware failure. Limited by various factors, currently efficiency and robustness are two key issues for real-time clock estimation.

In the conventional real-time clock estimation, UD observations are employed and the computation time depends mainly on the number of estimated ambiguity parameters (Geng et al. 2012). As introduced in Chapter 2*, obviously, the computation becomes much more time-consuming if more stations are involved for reliable estimation. The task, to update clocks within five seconds, could be fulfilled with difficulty for multi-GNSS clock estimation, with more than 120 satellites. Furthermore, for such a large linear system, a sophisticated quality control procedure, which must be implemented, also needs significant computation time. In recent years, fast computation approaches optimized according to CPU structure, such as matrix operations were also skillfully introduced into GNSS data processing in order to improve the computational efficiency (Gong et al. 2018). Ambiguity resolution was also implemented to reduce the number of active ambiguities, and consequently, the computation burden for clock estimation* which was introduced in Section 2.3 *(Laurichesse et al. 2009).*

Since the number of parameters to be estimated by the ED model is greatly reduced, estimation by using the ED model is another way to solve the efficiency problem. Bock et al. employed ED phase observations to densify CODE's final clock of 5-minute intervals to 1 Hz for special precise applications, in which the 5-minute clocks derived by using UD

phase and range observations are fixed as "control points" (Bock et al. 2009). Generally, UD provides absolute clocks, while ED generates the high-rate clock change as the majority of parameters, e.g., ambiguities are eliminated and consequently the computation load is significantly reduced. On the same basis, Zhang and Li extended this method for real-time clock estimation with a dual-thread strategy; the UD thread is for the absolute clock estimation with an interval of five seconds, while the ED thread estimates the clock change with an interval of one second (Zhang et al. 2011). The ED clocks are aligned to the UD ones to generate the final high-rate satellite clocks to meet the requirements of real-time kinematic PPP.

Furthermore, Ge et al. introduced an alternative approach to estimate high-rate real-time satellite clocks using ED phase and UD range observations in a single filter, so that no ambiguities are estimated and clock changes are aligned by range to absolute clocks (Ge et al. 2012). The result shows that the approach can achieve a comparable accuracy to that of the UD approach, whereas the computation time is reduced to one tenth. This strategy was also implemented into real-time multi-GNSS clock estimation and evaluated (Zhang et al. 2016, Chen et al. 2017, Chen et al. 2018).

Anyway, as discussed above, the mixed-differenced method with UD for absolute clocks and ED for clock variation is one of the most efficient strategies for multi-GNSS clock estimation with large networks, although UD is now widely used. One of the remaining issues is how to combine the UD and ED, integrated into one process as parallel inline processes (Zhang et al. 2011) or even in a single adjustment (Ge et al. 2012).

In addition, another effective way to improve the robustness of real-time products is the combination of difference clock processes. Mervart and Weber (2013) use Kalman filter to combine independent clock corrections from different ACs. Any clock correction was expressed as three parts, which are the intimal clock bias, AC-specific clock offset and satellite-specific clock offset and combined in a filter epoch by epoch. The combined solution significantly reduces the risk of outages and outliers in single thread clock product. Chen et al. (2017b) improves the strategy of outages and anomalies processing in Mervart and Weber's method in the combination. Parameter separation and weight estimation are proposed in the processing. The results show that the availability of combined products is as high as 99.9%, which is much better than that of single AC and IGS01 and IGS02 products. Although the theoretical difference is slight, the reliability and robustness of the processing schema are of great concern for providing satellite clocks for real-time operational service. For this purpose, we have to consider the following two aspects. First

of all, redundant processing lines are definitely needed and can be deployed either in the same location or offsite, and their outputs can be combined to a unique product for providing reliable service. It will not affect the performance if some of the redundant processing lines are crashed. Second, disturbed processing may be needed if a network cannot be processed in a single adjustment because of too many stations and/or satellites. In fact, along with the development of modern processors and servers, the parallel computing on a distributed framework is receiving increasing interest in scientific computation community.

In this chapter, an alternative processing strategy is developed for multi-GNSS real-time high-rate clock estimation, in which a number of UD and ED processing lines can be involved and their output clocks are combined to generate a unique clock product. The UD and EU lines can be designed for sub-networks or a set of GNSS systems, or duplicated lines for redundancy. They can be deployed and operated independently over different and even offsite computers. Then, the ED and UD clocks are combined with separated software developed by us in a similar way to that done for the combination of AC products at the IGS real-time combination center (Mervart et al. 2013). As each of the processing lines can be run in different computers, we named it Decentralized Clock Estimation (DECE) in this study.

The processing strategy is realized based on the PANDA software for validation (Liu et al. 2003, Shi et al. 2008). A network of about 110 real-time stations with the tracking capacity of GPS, GLONASS, Galileo, and BDS four systems is employed and real-time estimated clocks, as well as the computation time using the UD processing mode and the DECE mode, are compared and the PPP performance is also evaluated. First, the current research status for multi-GNSS and real-time clock estimation is introduced, followed by the discussion of the multi-GNSS real-time clock estimation model. Additionally, the strategy of data processing and the real-time clock estimation system based on PANDA software are presented. The real-time clock product estimated by the DECE strategy is also validated by clock comparison and its application to multi-GNSS PPP. Finally, a summary of the results and corresponding conclusions is provided.

4.2 Multi-GNSS clock combination

In this section, we propose a method to combine multiple independent original UD or ED clocks together to generate a unique real-time clock, such as clocks from different software packages or different networks, etc. It will not only improve the stability of the product, but

also solves the problem of computation efficiency. It should be noted that all combination method proposed in this chapter use the same ultra-rapid orbit to avoid the effects of orbital differences and improves the consistency between original and combined clock. The final goal is to provide a reliable real-time GNSS product with high quality.

Although the ED model is computationally efficient enough to support a high-rate update, it can only provide epoch-differenced clocks. Therefore, the UD model must be involved in order to obtain the absolute clock. Thus, a combination process is essential to generate the final clock product that takes advantage of both ED and UD clocks. Theoretically, we can also consider the further combination of the combined ED and UD clock products in Section 4.2.1. A simple but efficient approach was implemented by using the latest available UD clocks to align the high-rate clock changes estimated by the ED model to generate the final high-rate absolute clocks.

Assuming that the update interval of the UD model is k times of the ED model, for example, if the update rate of the UD is 20 sec and that of ED 5 sec, then k = 4, and the combination for post-processing can be expressed as follows (Zhang et al. 2011),

$$dT(t_i) = \begin{cases} dT_{UD}(t_i) & ,mod(i,k) = 0 \\ dT(t_{i-1}) + dT_{ED}(t_i, t_{i-1}) & ,otherwise, i \geq 1' \end{cases} \quad (4.1)$$

where dT_{UD}, dT_{ED} represent the UD and ED clock at each epoch, dT represents the combined clock, t is the epoch time, and the symbol mod means remainder operator. From Equation (4.1), it can be seen that the essence of this approach is using the last UD estimate to calibrate the ED estimates at the following epochs.

However, in the case of real-time clock estimation, the approach must be adapted, as the computation of the UD model usually takes a much longer time than the ED model. Thus, only the latest available UD clocks could be used to calibrate the ED clocks to absolute ones.

For real-time processing, the update rate of the UD and ED model should be properly selected, i.e., the processing/update interval must be larger than the processing time needed and it must be k times the ED interval. The processing schema is illustrated in Figure 4.1. In the Figure, j is the epoch index of UD processing, the related epoch time is $t_{j\times k}$, and within two adjacent UD epochs, there are k ED epochs.

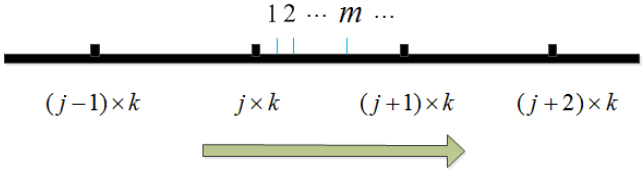

Figure 4.1 UD and ED processing schema

According to the above criteria for selecting k, we can assume that at each ED epoch within $t_{j\times k}$ and $t_{(j+1)\times k}$, let us say epoch $t_{j\times k+m}$, the UD clock at epoch $t_{(j-1)\times k}$ is always available, and that at epoch $t_{j\times k}$ it may be available depending on the computation efficiency of the UD process. Thus, the combined clock reads as the first expression of Equation (4.1) if $dT_{UD}(t_{j\cdot k})$ is unavailable at epoch $t_{j\times k}$ while reads as the second expression of Equation (4.2) if $dT_{UD}(t_{j\cdot k})$ is available.

$$dT(t_{j\cdot k+m}) = \begin{cases} dT_{UD}(t_{(j-1)\cdot k}) + \sum_{l=(j-1)\times k+1}^{j\times k+m} dT_{ED}(t_l, t_{l-1}) \\ dT_{UD}(t_{j\cdot k}) + \sum_{l=j\times k+1}^{j\times k+m} dT_{ED}(t_l, t_{l-1}) \end{cases} \quad (4.2)$$

with the following definition,

$$\Delta T_{ED}(t_l, t_m) = \sum_{r=m+1}^{l} dT_{ED}(t_r, t_{r-1}) \quad (4.3)$$

Equation (4.2) can be rewritten as

$$dT(t_{j\cdot k+m}) = \begin{cases} dT_{UD}(t_{(j-1)\cdot k}) + \Delta T_{ED}(t_{j\cdot k,(j-1)\cdot k}) + \Delta T_{ED}(t_{j\cdot k+m,j\cdot k}) \\ dT_{UD}(t_{j\cdot k}) + \Delta T_{ED}(t_{j\cdot k+m,j\cdot k}) \end{cases} \quad (4.4)$$

In the combination, accumulated ED clocks over the UD interval are computed, then the combined clocks are calculated using Equation (4.4), according to which the UD clock is available for the working ED epoch. It should be pointed out that the accumulated ED clocks over the latest two UD epoch intervals must be saved for continuous propagation of the clock reference.

Besides this, it should be noted that the matching of the UD and ED processes is simplified to an addition operation and the noise of them are not considered in this study. We take the results of the UD process as a constraint which generates the absolute clock offset, whereas the ED process generates a set of relative clocks.

4.3 Real-time decentralized clock estimation strategy

Instead of integrating ED and UD and combination processing in a single process in terms of threads, we propose a decentralized clock estimation mode in which UD, ED, and the combination can be run in separated computers with a network connection. Figure 4.2

shows a flow chart of the simplest DECE configuration with one UD, and one ED and a combination process each running in a server. Ultra-rapid orbit and real-time observations are needed for each server group and we fix site coordinates to Solution INdependent EXchange (SINEX) format solution (Ray et al. 2004; Rebischung et al. 2014). Both clock products from the ED and UD processes are transferred to the server where the combination is running to generate the final clock products simultaneously according to Equation (4.4). It should be noted that the orbit switching on each server is synchronous.

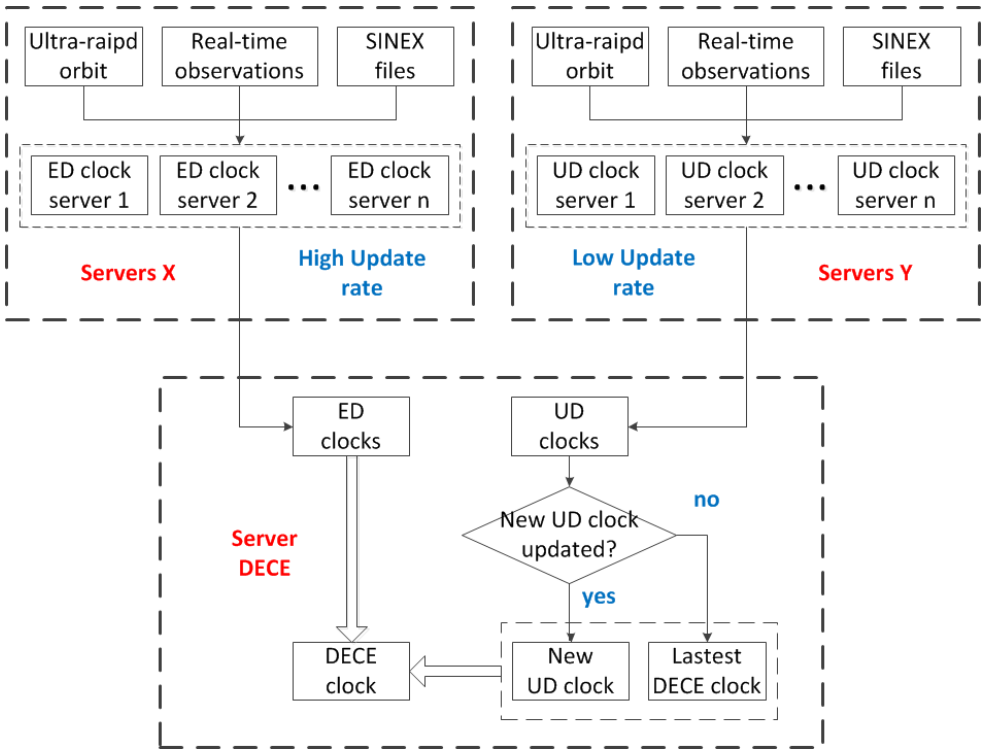

Figure 4.2 Flow chart of the DECE clock estimation with the basic configuration, i.e., one UD, one ED, and one combination process, each running in a server

One of the advantages of the DECE is that the data exchange among the processes is very small and mainly for transmitting the estimated clocks, and thus can be easily realized through a TCP/UDP port. A much more important advantage is that DECE can significantly improve the robustness of the real-time precise positioning service by running redundant processing processes.

Although only two clock estimation processes are deployed in Figure 4.2 and used in this study, it can be extended to include more with the same strategy and stations as redundant processing. Processing processes with different strategies or different station sub-networks can also be involved for using more stations. All the processing processes can be deployed in servers either of a local network or in an offsite network. The

combination processes automatically collect the necessary clock estimates according to specified weights to generate a combined product. It is obvious that the robustness of the processing or the availability of the clock products can be dramatically improved by such a distributed system, as the system can always provide high-rate clock product if one of the redundant ED solutions and one of the redundant UD solutions are working well. The crash of the clock combination process is negligible, since it can provide well-qualified combined clocks instantaneously after restarting.

4.4 Real-time experimental evaluation

In order to validate the DECE strategy, the PANDA software package (Liu and Ge, 2003, Shi et al. 2008) is used as the base, and the real-time estimator is adapted to a distributed environment and a tool for real-time clock combinations developed for the DECE processing. First, we describe the whole data processing of the real-time precise positioning service based on the PANDA software package, and then the network and finally the processing parameters and processing schema used in the validation.

4.4.1 Data processing system

In the data processing system, the real-time POD is carried out in batch-processing mode using the observations from MGEX and IGS networks. All parameters in POD are estimated by least squares adjustment and previous 24-hour observations are used to generate the rapid orbit. Then the real-time orbit is predicted based on the rapid orbits in a batch-processing mode by using orbit integrator for at least six hours in a similar way to that of the IGS ultra-rapid data processing. Then the real-time clock estimation processes will do parameter estimation epoch by epoch based on the fixed real-time orbit using the methodology introduced in Section 4.3.2.

The BNC software version 2.12 (Stürze et al. 2016) is used to receive real-time observations as well as ephemeris data to feed the filter for clock estimation, and is also used to generate state-space representation corrections from the estimated orbits and clocks. Real-time data are transported using the NTRIP protocol and encoded/decoded following the RTCM 3.3 standard (RTCM, 2016). The structure of all systems is shown in Figure 4.3.

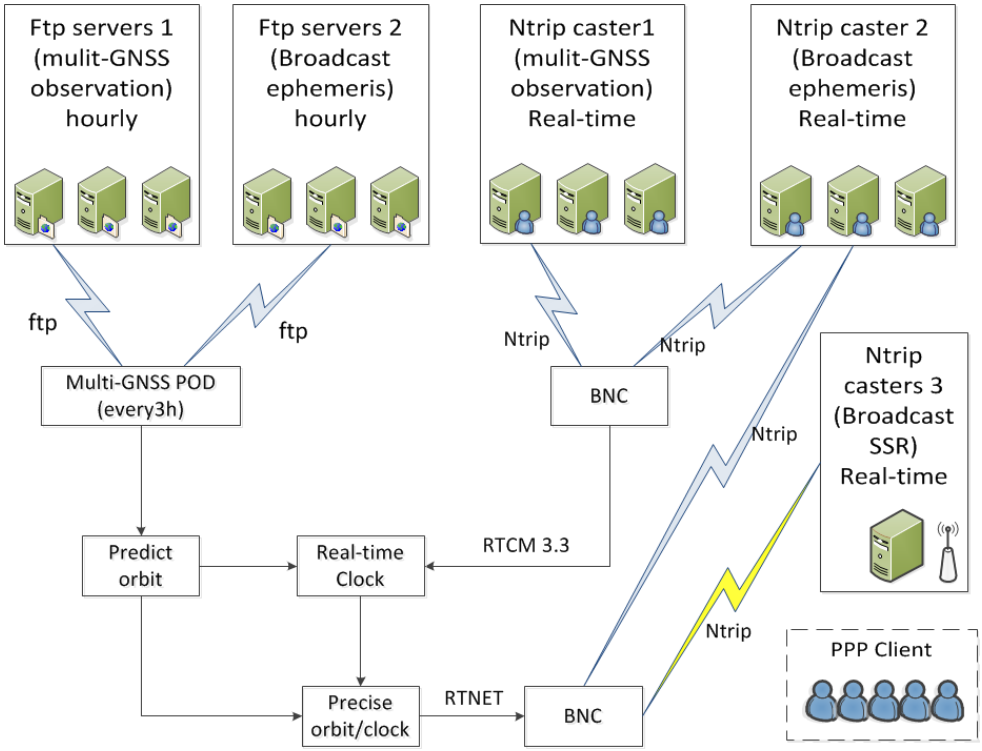

Figure 4.3 Flow chart of the real-time precise positioning service system based on the PANDA software package

In order to evaluate the performance of the DECE processing strategy, the "Real-time Clock" function in Figure 4.3 can be replaced by a single UD processing or by the DECE in Figure 4.2 to carry out UD processing and DECE processing for comparison.

4.4.2 Data and network

A network of 110 global multi-GNSS stations is employed in the experiment. All the 110 stations can track GPS signals, while 105, 65, and 83 stations are with GLONASS, Galileo, and BDS tracking capacity, respectively. Most of the real-time observation streams are provided by IGS and the Multi-GNSS Experiment (MGEX). GFZ and BKG also contributed some multi-GNSS stations. The distribution of the stations is shown in Figure 4.4. The circle marks are the 110 stations used for clock estimation, while the stars indicate the 12 stations used for real-time PPP test in Section 4.5.3, which are not included in clock estimation. Because of the network or other reasons, real-time streams are not as stable as the recorded observation files. Normally there are at least 90 stations available for clock estimation.

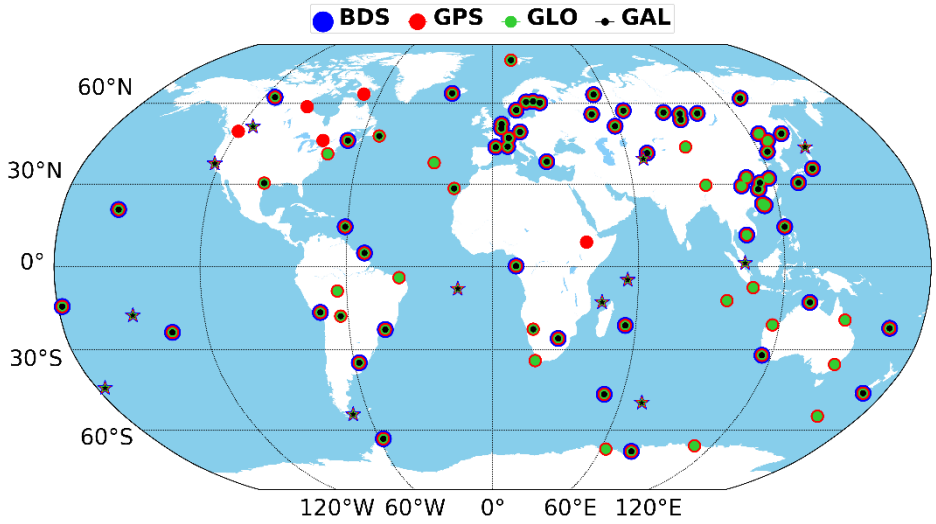

Figure 4.4 Distribution of stations for the multi-GNSS real-time clock estimation marked by cycles and that for PPP test by pentagrams

4.4.3 Processing strategy

The data processing parameters follow those outlined in Table 3.1, with the exception that the ED model no longer includes estimates for the ISB and ambiguity parameters.

4.5 Validation and results

The experimental real-time precise positioning service has been run operationally and we take the orbit and DECE clock products from Day of Year (DOY) 274 to 280, 2018 for the validation. In the experiment, we use a 5-sec update rate for ED clock estimator and 20 sec for UD clock estimator to generate 5 s final DECE clock products. The CPU we used is Intel(R) Xeon(R) CPU E5-2637 v4 @ 3.50GHz.

4.5.1 DECE results compared to UD results

Taking the results of DOY 251 in 2018 as an example, Figure 4.5 shows the time consumed using UD and DECE at each epoch. The computing time of the DECE is 0.07 seconds on average, which is much less than that of the UD mode, which is about 5.66 seconds. It should be noted that it is difficult to update the UD clock within five seconds at each epoch, especially when quality control is involved. What is more, with the completion of Galileo and BDS in the near future, 124 satellites will be used and the burden of calculation will further increase. On the contrary, the DECE model can solve this computational problem easily.

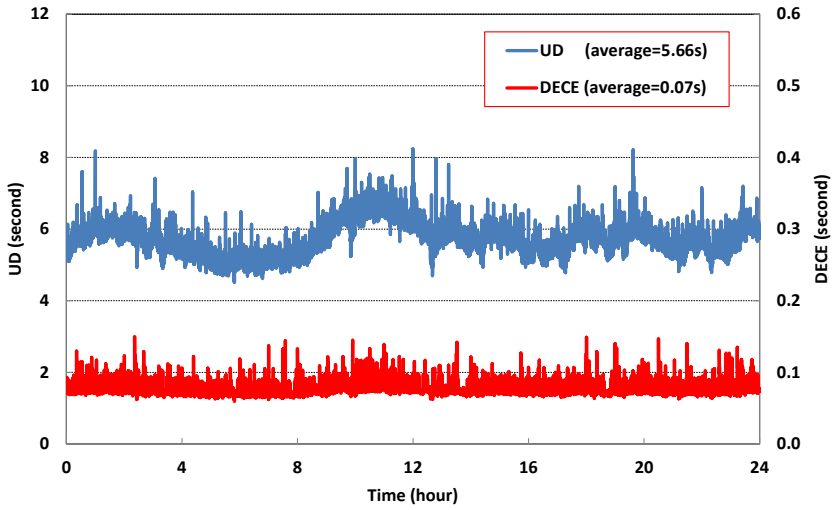

Figure 4.5 Computational time at each epoch using DECE and UD modes for DOY 251, 2018

According to the combination algorithm described by Figure 4.1, the difference between DECE and UD clocks is mainly caused by the non-synchronization of the clock datum. Taking the results of DOY 251 in 2018 as an example, Figure 4.6 shows the time series of differences between the DECE and UD products and each subplot shows the differences of all satellites of one system.

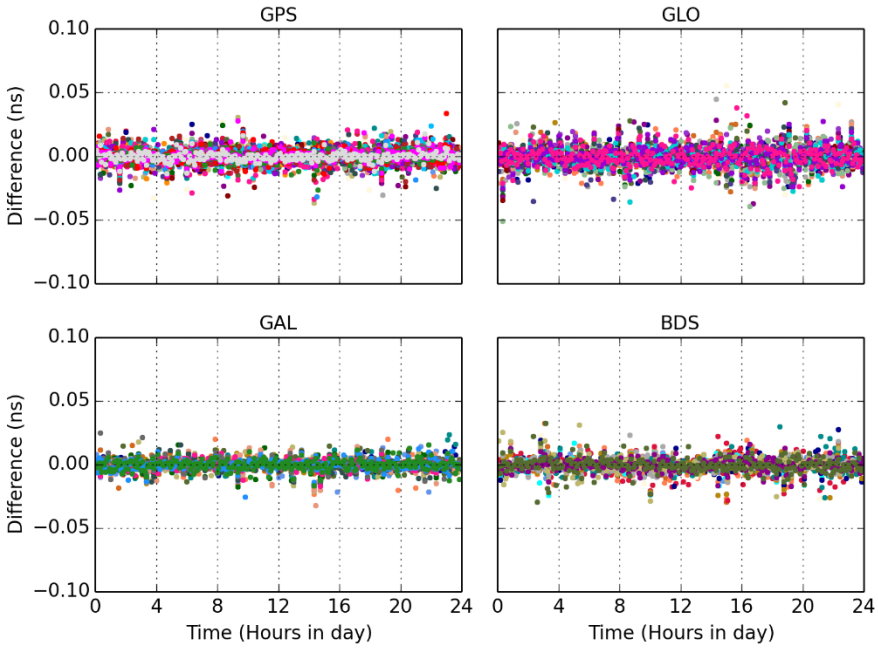

Figure 4.6 Differences between DECE clock and UD clock

From the results, it is obvious that most of the differences between DECE and UD are very subtle, normally smaller than 0.02 nsec (about 6 mm). For multi-GNSS real-time PPP, the influence of such differences can be ignored.

Figure 4.7 shows the detailed behavior of the difference between the UD and the DECE results, which takes a 5-minute time series as an example. Since the interval of UD results is 20 seconds, which cannot fit with the 5-seconds DECE clock at each epoch, the linear interpolation has implemented to the UD clock to ensure there is always a corresponding point fit to DECE. In addition, it will not be clear enough if the results of many satellites are plotted together in one figure, so here we plot the single satellite's series and take G02 and G06 as an example for analysis.

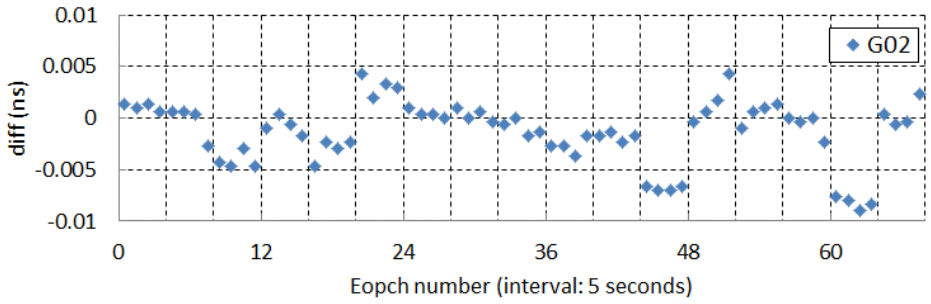

(a) Result of G02 satellite

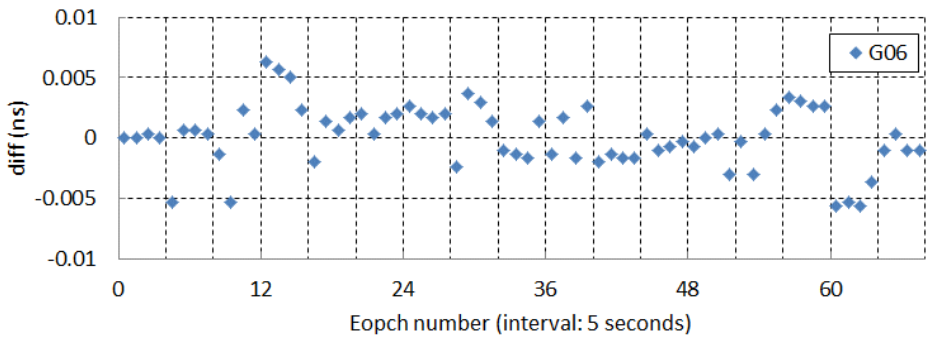

(b) Result of G06 satellite

Figure 4.7 Detailed differences between DECE and UD

Figure 4.7 is interesting because there appears to be a periodical slip every 4 epochs (20 seconds) in the series, but not always obviously. This is probably because normally the DECE process needs to adjust to the UD process as a datum every 4 epochs. According to the combination methodology described in Section 4.4.3, the difference between DECE and UD clocks present in the series is mainly caused by the non-synchronization of the clock datum. However, more detailed property of these slips still needs further research.

4.5.2 DECE results compared to post-processed products

As for further evaluation of the DECE products, they are also compared with the GBM products provided. The clock difference and the Signal-In-Space Ranging Error (SISRE) which is a measure of the joint effect of orbits and clocks will be analyzed below.

4.5.2.1. Clock STD

Since receiver and satellite clocks are estimated epoch-wise as white noise, the clock datum could change from epoch to epoch and the inter-system range bias at receivers could also induce inter-system clock biases. Therefore, in the multi-GNSS clock comparison, a satellite clock from each system is selected as a reference, and single-differenced clocks with respect to the reference satellites are used, in which the datum differences between different products are removed. Here G01, R01, E01, and C11 are selected as the reference satellite for each system, respectively.

As the bias in the time series of the between-satellite clock differences can be absorbed by ambiguities in PPP, the STD of the clock is a significant indicator to reflect the impact of the clock on phase-based positioning. STD values of the differenced clocks are calculated for each satellite and shown in Figure 4.8. Each subplot in Figure 4.8 is for a system indicated inside the i-th system averaged STD value. For BDS to the left and right of the slash means the value for MEO/IGSO and GEO, respectively.

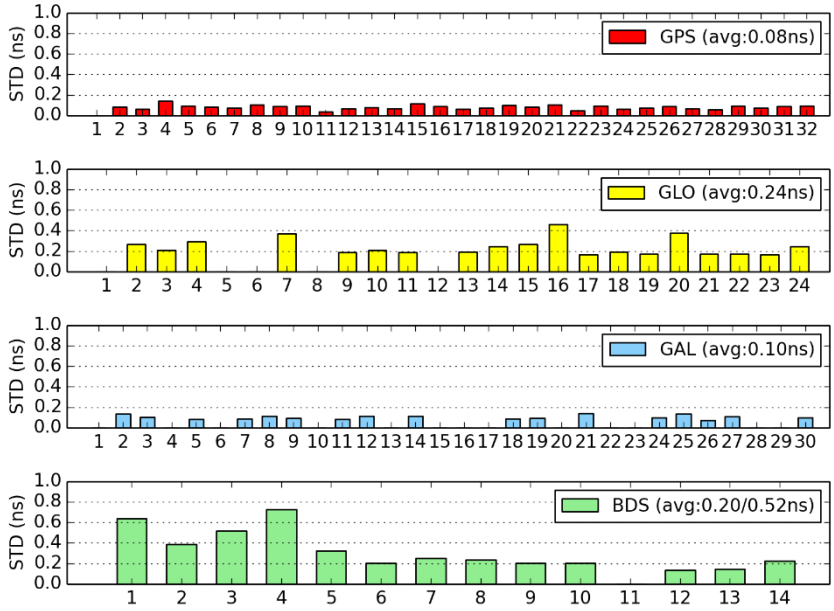

Figure 4.8 STD of the clock difference between DECE and GBM product

From the statistical results above, it can be seen that the average STD of GPS is 0.08 ns, while GLONASS, Galileo, BDS MEO/ISO, and BDS GEO are 0.24 ns, 0.10 ns, 0.20 ns, and 0.52 ns, respectively. The main reason for the larger difference of BDS GEO satellites is due to the insufficient tracking stations and the poor tracking geometry.

4.5.2.2 Clock SISRE

In the clock estimation, most of the orbit biases in the radial direction can be absorbed by clock parameters. This means that satellite clocks are biased by orbit biases in the radial direction and the biases are complementary. The SISRE is a statistical measure for the impact of orbit and clock errors on the modeled pseudo range. The SISRE takes the orbit differences into consideration while comparing clocks of two products by projecting their satellite position difference on the line-of-sight direction from satellite to the user position. It is introduced as a more reliable indicator of the comprehensive influence of orbits and clocks. The formula of SISRE (Montenbruck et al. 2015) is,

$$SISRE = \sqrt{(a * dR - c * dt)^2 + b * (dA + dC)^2} \qquad (4.5)$$

where dR, dA, *and* dC *represent the orbit differences in radial direction, along direction, and cross directions, while* dt *denotes the real-time clock error compared to final products,* c *is the speed of light in vacuum, a and b represent the SISRE coefficient according to satellite altitude. The coefficients for multi-GNSS SISRE are shown in Table 4.1 (Montenbruck et al. 2015). Obviously, we can find that the SISRE is mostly affected by the radial direction orbit difference and clock difference.*

Table 4.1 Coefficient of SISRE

System	***a***	***b***
GPS	*0.98*	*1/41*
GLONASS	*0.98*	*1/45*
Galileo	*0.98*	*1/61*
BDS (MEO/IGSO)	*0.98*	*1/54*
BDS (GEO)	*0.99*	*1/126*

The results of SISRE are shown in Figure 4.9. From the statistical results above, it can be seen that the average SISRE for GPS is 0.12 m, while GLONASS, Galileo, BDS MEO/ISO, and GEO 1.51 m, 0.11 m, 0.33 m, and 0.52 m, respectively. The SISRE of GLONASS is significantly larger than for other systems probably due to FMDA which

needs further research. It should be noted that SISRE primarily reflects the impact of these products on pseudo-range positioning.

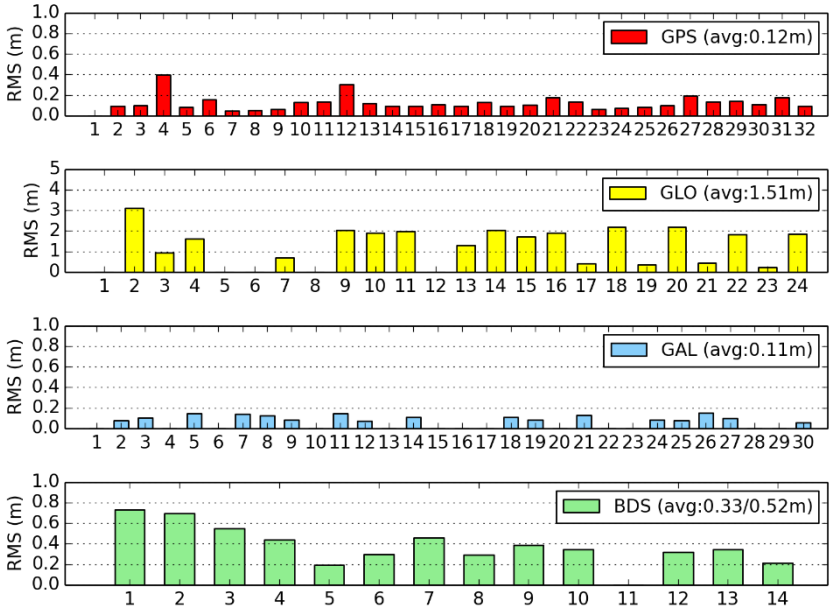

Figure 4.9 SISRE of the DECE clock

4.5.3 PPP validation

PPP is a convincing way to directly verify the orbit and clock products together. In the experiment, real-time kinematic PPP is also carried out for 12 global multi-GNSS stations from MGEX using the DECE products and the UD products, respectively. The data processing strategy and parameter model are the same as in Table 3.1, except that the satellite clock is fixed in PPP and coordinates are estimated in the kinematic mode as white noise. The real-time streams come from mgex.igs-ip.net:2101 and the sample rate is set to five seconds. PPP for all stations is processed using multi-GNSS observations.

Figure 4.10 illustrates the positioning error of the station ASCG in the north, east, and vertical components. The figure shows that the positioning accuracy of PPP with the DECE clock in a real-time mode is better than 10 cm in the horizontal and 20 cm in the vertical after initialization, which can meet the need most positioning applications. Similar accuracies were obtained for the other stations.

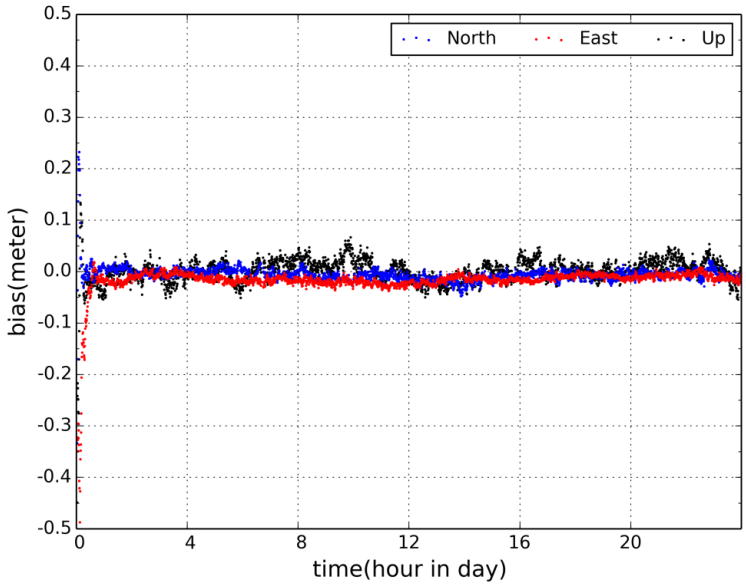

Figure 4.10 Result of real-time PPP using the DECE clock

The Root Mean Square (RMS) is an important indicator for evaluating the positioning performance which can be calculated as,

$$RMS = \sqrt{\sum_{i=1}^{n} (X_{ppp} - X_{ref})^2 / n} \tag{4.6}$$

where X_{ppp} and X_{ref} represent any of the calculated and reference coordinates and n is the epoch number used for PPP.

In the experiment, the RMS of the position differences using DECE and UD products are shown in Figure 4.11, in which the legend H and V mean horizontal and vertical direction, respectively. All results are counted after PPP convergence. The statistics show that the average RMS is about 3.10 cm for using UD and 3.14 cm for DECE in horizontal, and 5.47 cm for using UD and 5.51 cm for DECE in vertical. In general, for PPP, centimeter-level positioning results can be achieved using the clock products. Normally the result of UD is a little better than DECE, but there is almost no difference in the accuracy between using DECE and UD products.

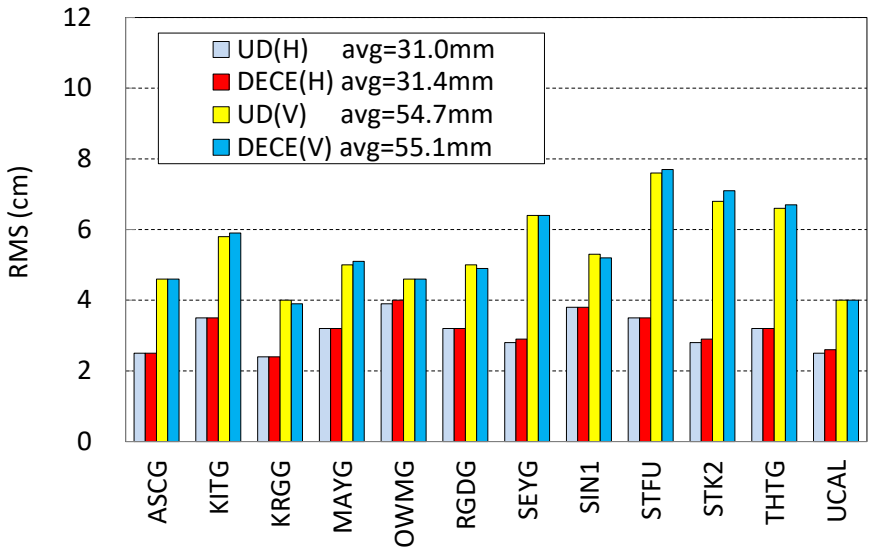

Figure 4.11 Comparison of RMS in PPP results utilizing DECE and UD products

4.6 Discussion

With the great progress of multi-GNSS real-time PPP, the performance of real-time clock products becomes more and more important. Different from post-processing and near-RT modes, the computational efficiency of real-time clock estimation is critical, because the delay or missing of the products will directly affects the positioning accuracy of the PPP client. Moreover, since the recovery of real-time service normally takes a lot of time, especially in case of software crashes, higher requirements for the stability and continuously of real-time products are also necessary. In Section 4.3, to solve the problems above, we proposed a DECE strategy to improve the computational efficiency and enhance the robustness of the real-time system. First, both low-rate UD and high-rate ED processes are implemented to guarantee the timely update of real-time clock products. From Figure 4.1, it is noted that although with the launch of more new satellites and setup of more ground GNSS stations in near future, the processing pressure will still not increase significantly. In addition, when using the DECE strategy, more than one line can be the processed in different processing centers or processing using different strategies (ED/UD). This means the robustness of the processing or the availability of the clock products can be significantly improved by such a distributed system, as the system can always provide high-rate clock products if one of the redundant ED solutions and one of the redundant UD solutions are both working well. As the PPP experimental results show in Section 4.5, centimeter accuracy position can be achieved using the DECE real-time products, which

is a great improvement of computational efficiency and robustness. It also improves the experience of real-time positioning users.

4.7 Summary

In this chapter, a decentralized clock estimation approach is proposed to improve the computational efficiency and robustness of the real-time precise positioning service. In the new approach, both the UD and ED modes are implemented but run separately in different computers. The UD mode estimates clock offsets with a lower update rate because a great number of ambiguities parameters are included, while the ED mode determines clock variations with a higher update rate. The products of the two modes are combined to generate the final products. Redundant UD and/or ED processing lines can be scheduled even in offsite computers with an internet connection to improve the robustness of the processing system. More processing lines for different networks can also be included to improve the clock quality.

The new approach is realized for the experimental evaluation based on the PANDA software package for GNSS data processing and BNC software for data communication. The experiment was carried out in real time with about 110 stations for clock estimation and 12 stations for PPP. The clock comparison of the new approach with GFZ MGEX product shows that the STD of GPS is 0.08 nsec, while GLONASS, Galileo, BDS MEO/ISO, and BDS GEO are 0.24 nsec, 0.10 nsec, 0.20 nsec, and 1.52 nsec, respectively. The average SISRE of the clock product of GPS is 0.02 m, while GLONASS, Galileo, BDS MEO/ISO, and BDS GEO are 1.51 m, 0.11 m, 0.33 m, and 0.52 m, respectively. Using the estimated clocks and corresponding orbit products, real-time kinematic multi-GNSS precise point positioning can be realized with an averaged RMS of about 31.4 mm in horizontal and 55.1 mm in vertical.

All these results confirm that the decentralized clock estimation can provide comparable clock products as the most used undifferenced method but with a much higher computational efficiency and robustness. It is a suitable approach for multi-GNSS real-time clock estimation with the increasing number of satellites and stations and signals of different frequency bands.

5 Real-time Precise Positioning Service

Since its establishment in 1994, the IGS has remained steadfast in its commitment to delivering high-quality GNSS products, accessible worldwide at no cost. Continuing this tradition of excellence, the RTS provided by IGS ensures the provision of superior quality products crucial for a variety of geospatial applications. It stands as a pivotal initiative, dedicated to providing GNSS orbit and clock correction services essential for PPP and related applications. Leveraging the IGS's global infrastructure of network stations, data centers, and analysis centers, the RTS ensures the delivery of world-standard, high-precision GNSS data products.

Aligned with the IGS RTS mission, each AC within the IGS has systematically developed its own RTPPS system, contributing to a harmonized effort to enhance global navigation satellite systems. These tailored RTPPS systems, managed by individual ACs, play a vital role in fulfilling the overarching objectives of the IGS. With a primary focus on real-time data and services, particularly satellite orbit and clock corrections, each AC significantly enhances the collective performance and reliability of the network, especially in areas critical for precise navigation and timing.

This chapter provides a comprehensive overview of the RTPPS system at GFZ as one of the IGS real-time ACs. It elaborates on the system's components, encompassing advanced real-time orbit, clock, UDP, and regional atmosphere corrections on the server side, as well as various positioning modes on the client side. Additionally, the chapter evaluates the performance of each functional module, starting with the accuracy of orbit and clock correction products, and analyzes the impact of network configuration on clock estimates. Furthermore, the performance of UPD products is analyzed. Finally, this chapter examines client-side performance, including an assessment of atmosphere modeling effectiveness and a comparison of various PPP positioning models. The main contribution of the author in this chapter is the development of the real-time UPD, regional augmentation, and PPP modules for the RTPPS at GFZ.

5.1 System architecture

Typically, a RTPPS system comprise both server-side and client-side components. The server side primarily handles real-time POD, PCE, UPD, and extraction of regional atmosphere delay information. On the other hand, the client side is responsible for

implementing various precise positioning algorithms, including PPP, PPP-AR, and PPP-RTK clients. Figure 5.1 illustrates the overall architecture of RTPPS developed by GFZ.

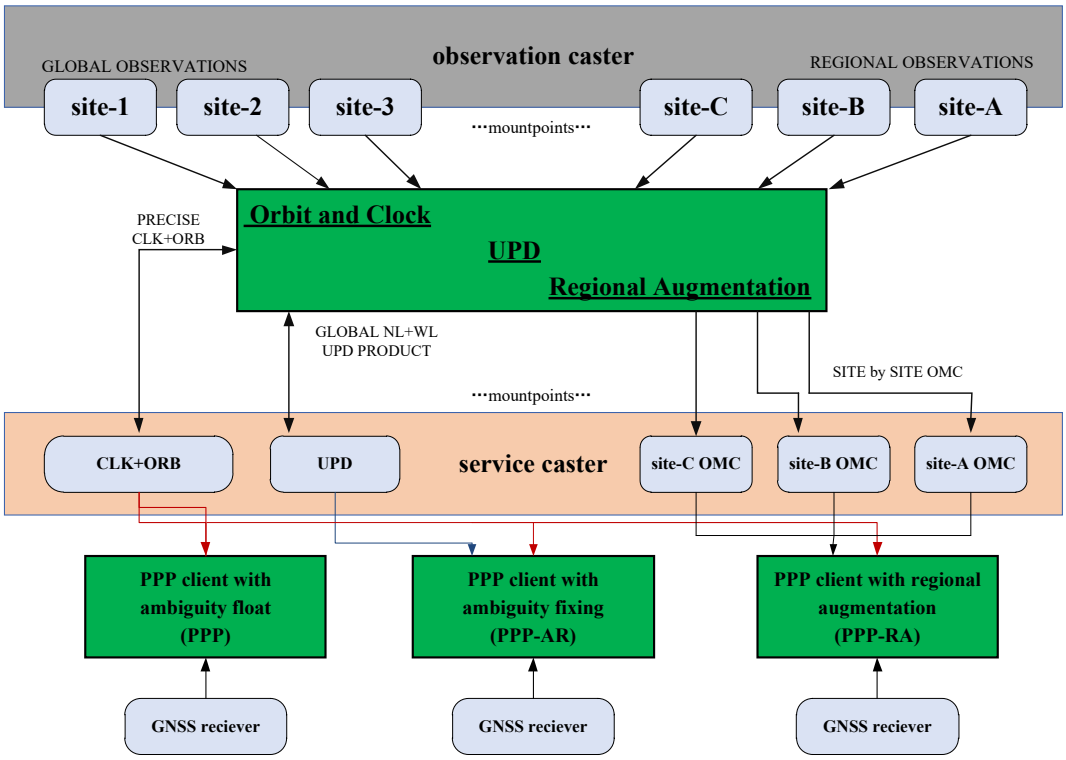

Figure 5.1 The structure of RTPPS at GFZ

This system integrates data from both global and regional observation stations to optimize positioning performance. It utilizes data collected by global observation stations for basic navigation signal correction through orbit and clock calculations. Additionally, regional augmentation based on local GNSS stations further enhance positioning performance. This architectural design allows the service center to offer various PPP services, ensuring global applicability while optimizing performance based on regional characteristics to provide more accurate and reliable positioning services. Real-time orbit and clock correction services serve as foundational support for users to achieve standard PPP, while UPD corrections facilitate ambiguity resolution, significantly improving positioning accuracy and shortening convergence time. Moreover, regional augmentation services enable instantaneous ambiguity fixing. The real-time orbit and clock functionality within the RTPPS is provided by the PANDA software, while the remaining functionalities are delivered by the PPP client software developed by the authors of this dissertation. A detailed introduction to each module of RTPPS will be provided below.

5.1.1 Real-time orbit and clock

The orbits provided by GFZ RTPPS are actually generated in the same way as that for the ultra-rapid orbits by the IGS ACs. The orbits used in real-time clock estimation is predicted based on the solution of the latest observations processed in batch mode. GNSS satellite orbit prediction is capable of achieving high precision, commonly reaching stability at the centimeter accuracy level within a few hours. The advantage of using predicted orbits is that it significantly reduces the computational pressure of real time parameter estimation and is unaffected by the instability of real-time data streams.

In real-time data processing, orbit determination and subsequent prediction are conducted at fixed intervals of either 2 or 3 hours, while normally the estimated arc length of the orbit extends 24 hours. The core processing script meticulously orchestrates a sequence of operations to safeguard the integrity and precision of orbit determination.

Facing the challenge of an increasing number of satellites in multi-GNSS POD, some improvements have been made to the efficiency of orbit estimation to ensure the smooth completion of orbit updates within each planned time period (Li et al. 2019a). In the process of orbit estimation, we have increased the data processing sampling interval from the conventional 300 seconds to 450 seconds to reduce the computational load. At the same time, we have extended the arc length of the orbit estimation from 24 hours to 48 hours to enhance the system's continuous operation capability. Lastly, we introduced parallel technology for orbit integration processing, treating each satellite individually, to shorten the time consumed by orbit integration.

Given the challenge of accurately predicted GNSS clock over the long term, real-time data streams are utilized to estimate clock per epoch using the SRIF. As demonstrated in Chapter 4, although the final real-time clock products might be generated by combining estimates from multiple independent processes, the processing workflow for each process remains the same. The following outlines the processing workflow for a single clock estimation process. It’s noteworthy that the clock offset processing adopts a real-time concurrent mode, rather than the batch processing mode used for orbit determination. Since the previous chapters have already provided detailed explanations of the real-time clock estimation strategy, it will not be reiterated here.

5.1.2 Real-time UPD

As detailed in Section 2.4, the UPD estimation module requires inputs of real-time float ambiguities, which can be derived from orbit determination, clock estimation, or PPP. This approach provides the estimator with the flexibility to use real-time orbit and clock products from various ACs, enhancing the adaptability of the system. Additionally, it allows for straightforward utilization of both regional and global network. The strategy for UPD estimation in RTPPS involves real-time single-epoch processing, utilizing least squares as the estimator.

Within the GFZ RTPPS services, float ambiguities from PPP are used for UPD estimation. Typically, the global network for UPD estimation includes about 200 globally distributed IGS stations, whereas regional UPD estimation usually requires at least 10 stations. At each epoch, a number of PPP process are running parallel and provide float WL and IF ambiguities epoch-by-epoch to UPD estimator. The UPD estimation process begins with WL UPDs, followed by NL UPDs, with identical procedure. Through iterative processes and quality control strategies, outliers are discarded until all UPDs conform to established standards.

At the end of each epoch-loop, the satellite-end UPD information is encoded in the RTCM format and uploaded to the caster. Users can then achieve real-time PPP-AR upon acquiring the UPD.

5.1.3 Real-time PPP and its regional augmentation

As detailed in section 2.3, with the support of real-time orbit and clock, a single GNSS receiver can achieve precise real-time positioning. Moreover, if real-time UPD information is available, users can implement more accurate PPP-AR solutions. Additionally, the support from a regional reference network, leveraging the spatial correlations among stations, enables the use of generated atmosphere information to further enhance the performance of the PPP solution.

Extracting precise real-time atmosphere information is crucial. In the atmosphere augmentation service of GFZ RTPPS, all stations within the regional network first undergo real-time PPP with fixed station coordinates. For epochs where ambiguities are fixed, precise zenith troposphere delay information can be directly obtained from the parameters. Additionally, slant ionosphere delay information can also be extracted for satellites with fixed ambiguities. Subsequently, the real-time precise atmosphere information for each

reference station is broadcast to the NTRIP caster. For PPP users within the network, accessing atmosphere information from the NTRIP caster allows them to achieve an atmosphere-augmented PPP-RTK solution. Typically, compared to standard PPP solutions, PPP-RTK can significantly shorten the convergence time. With adequately precise atmosphere information, it can also considerably enhance the positioning accuracy compared to PPP-AR.

5.2 Real-time orbit and clock performance

This section primarily assesses the performance of real-time orbit and clock products, UPD and PPP-RTK as well as atmosphere for regional augmentation. The impact of the number of stations on clock performance is also analyzed in detail.

5.2.1 Orbit and clock performance

Taking the products from February 2022 as an example, the performance of RTPPS real-time products is analyzed. The GBM product provided by GFZ is used as the reference. Furthermore, radial orbit correction has been incorporated into the clock comparison process to consider the compensation of radial component and the clock estimates. Figures 5.2 illustrates the RMS of the orbit in along-track, cross-track and radial direction, as well as the STD of the real-time clock. For positioning, we primarily focus on radial orbit errors and the stability of clock. According to the results, the RMS for the radial orbit component is 0.02 cm for GPS, 0.03 cm for GLONASS, 0.04 cm for Galileo, and 0.07 cm for BDS non-GEO satellites. Additionally, the STD of the clock is 0.08 ns for GPS, 0.18 ns for GLONASS, 0.06 ns for Galileo, and 0.14 ns for BDS non-GEO satellites. This level of performance ensures that the systems can reliably achieve centimeter-level real-time positioning accuracy.

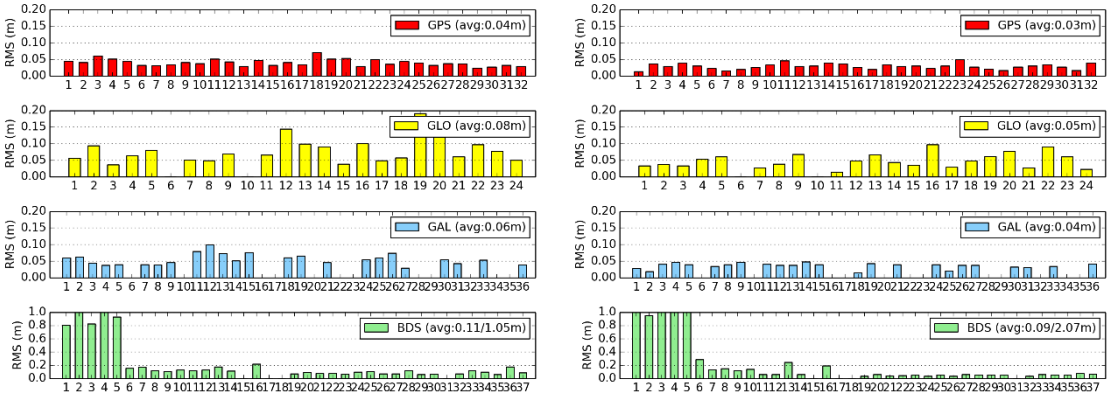

(a) RMS of orbit in along-track

(b) RMS of orbit in cross-track

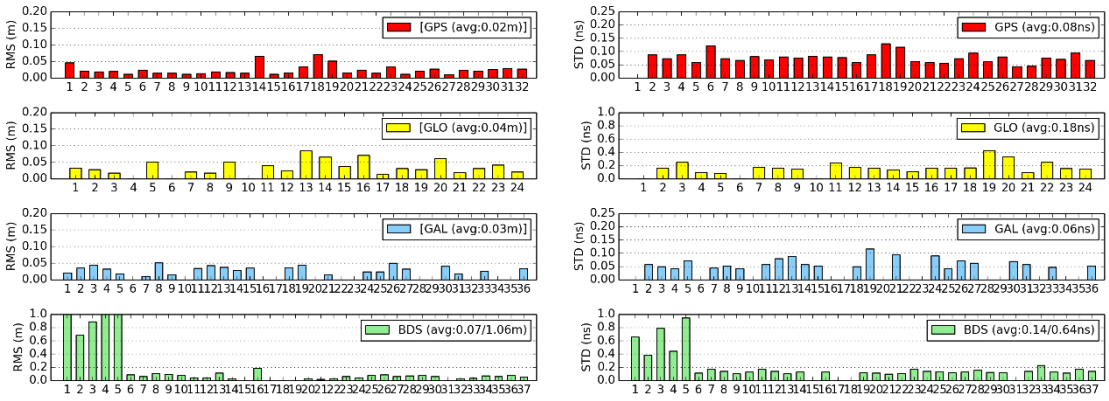

(c) RMS of orbit in radial direction (d) STD of the clock

Figure 5.2 Performance of real-time products

5.2.2 Impact of network configuration on clock estimates

In the real-time clock estimation, the instability of real-time data streams often leads to fluctuations in the number of available stations. This raises a common question: How many stations are needed at a minimum to ensure that the estimated clock is reliable enough to be broadcast to users? In this section, a simulated mode is adopted, processing varying quantities of stations to assess the impact of station count on the accuracy of clock estimates. To eliminate the influence of orbital factors, the experiment uses post-processed orbits and analyzes the impact of the number of stations on clock error estimation. Additionally, the BDS GEO satellites are not included in the experiment because they are closely related to regional station distribution and not significantly affected by global station distribution. Starting with 100 evenly distributed stations, the number of stations is reduced by 10 each time. However, once the station number drops to 50, it is reduced by only 5 each time. This adjustment is made because parameter estimation becomes more challenging with fewer stations. Figure 5.3 (a) – (d) illustrate the distribution of stations for processing with counts of 100, 70, 40, and 10 stations, respectively. When fewer than four stations are observed by the satellite, the clock parameter estimation is considered unstable, and the clock product is no longer generated.

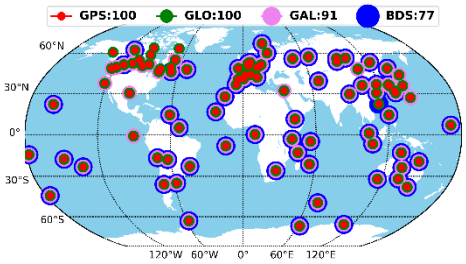

(a) Number of stations used: 100

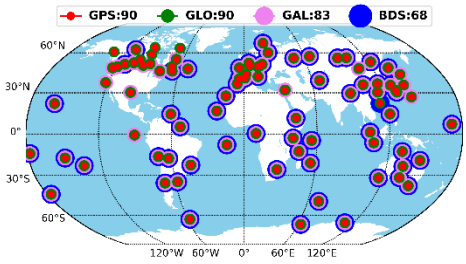

(b) Number of stations used: 90

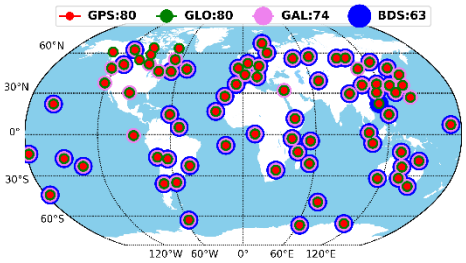

(c) Number of stations used: 80

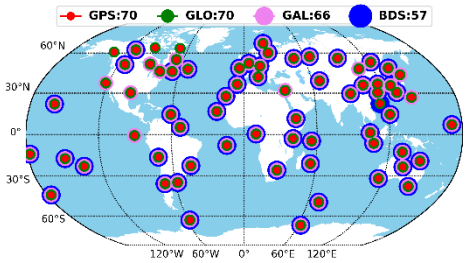

(d) Number of stations used: 70

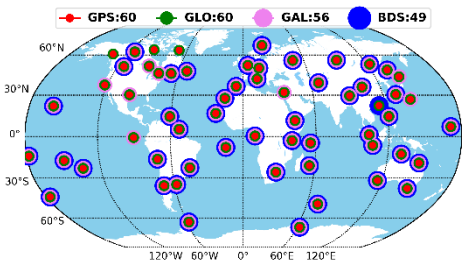

(e) Number of stations used: 60

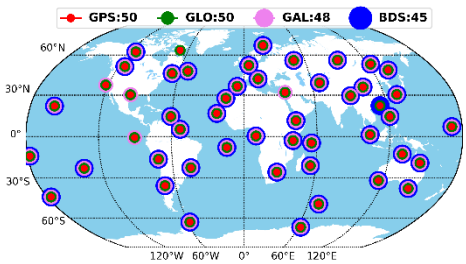

(f) Number of stations used: 50

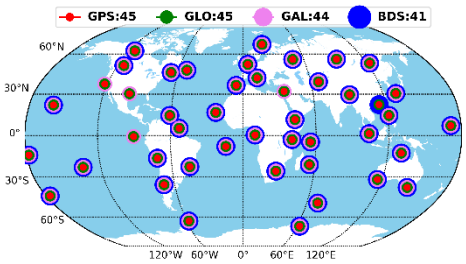

(g) Number of stations used: 45

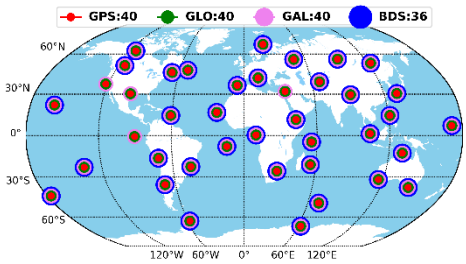

(h) Number of stations used: 40

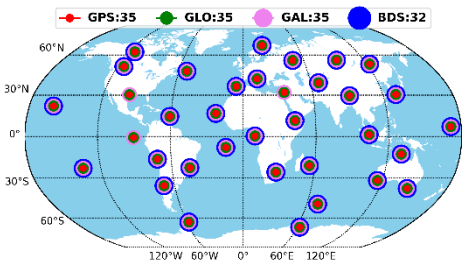

(i) Number of stations used: 35

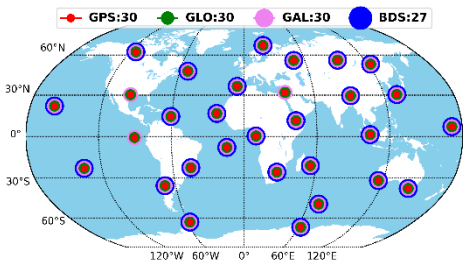

(j) Number of stations used: 30

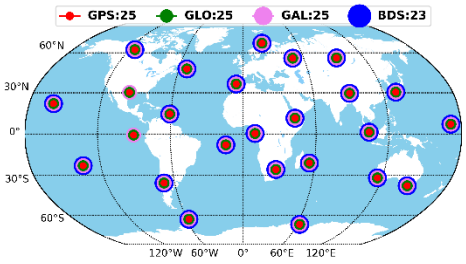

(k) Number of stations used: 25

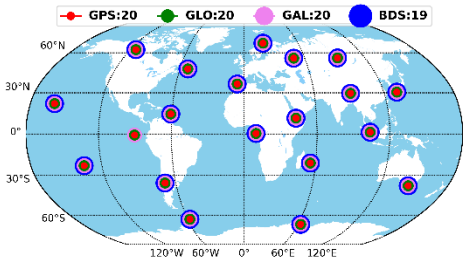

(l) Number of stations used: 20

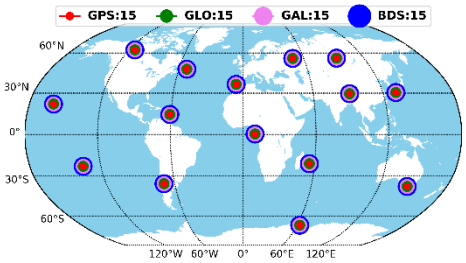

(m) Number of stations used: 15

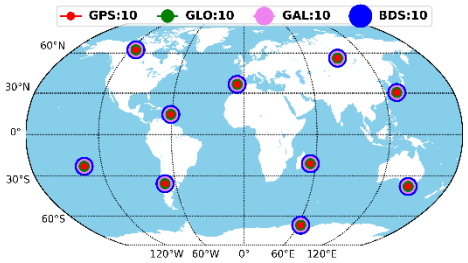

(n) Number of stations used: 10

Figure 5.3 Site distribution (from 100 to 10)

For simplicity in analysis, the following accuracy performance analysis primarily focuses on scenarios involving 100, 70, 40, and 10 stations. Figure 5.4(a) - (d) illustrate the estimated clock series for counts of 100, 70, 40, and 10 stations, respectively. The conclusion that can be drawn is that the clock series show no significant variation when the number of stations does not decrease below 40. However, when the number of stations is too low, such as only 10, the clock series exhibit noticeable interruptions, leading to a sharp decline in product integrity.

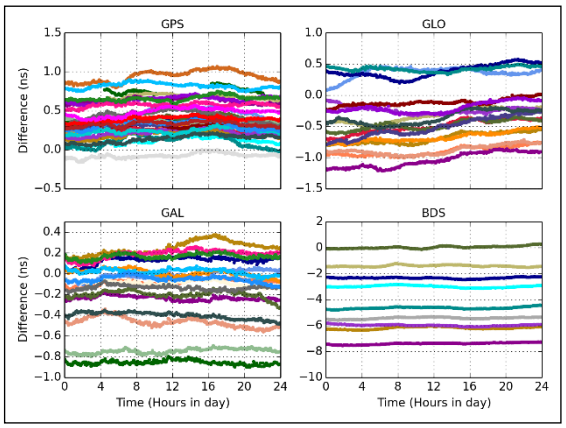

(a) Number of stations used: 100

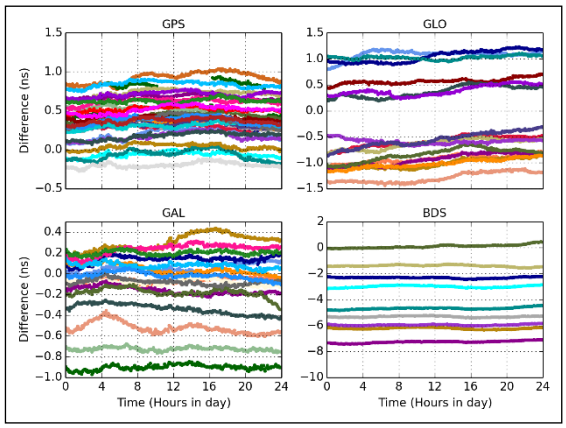

(b) Number of stations used: 70

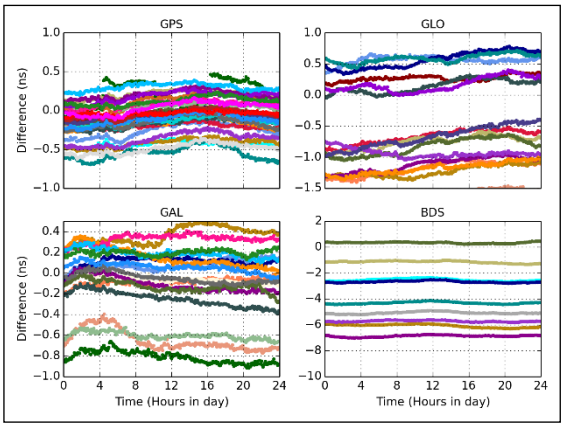

(c) Number of stations used: 40

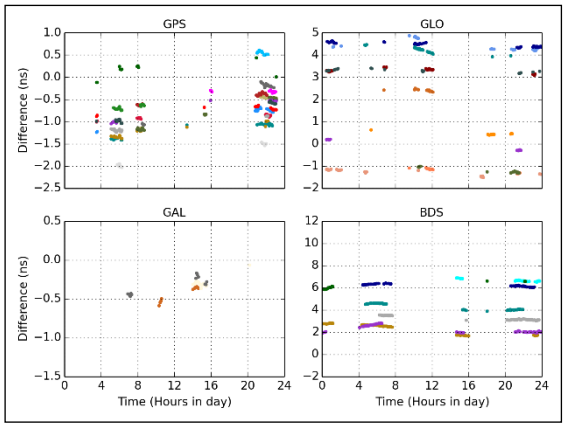

(d) Number of stations used: 10

Figure 5.4 Clock series with different configuration

Figure 5.5 (a) - (d) illustrate the STD of the clock series. It can be observed from the figures that, although the accuracy of the clock does not significantly deteriorate with a reduced number of stations, the quantity of products has significantly decreased.

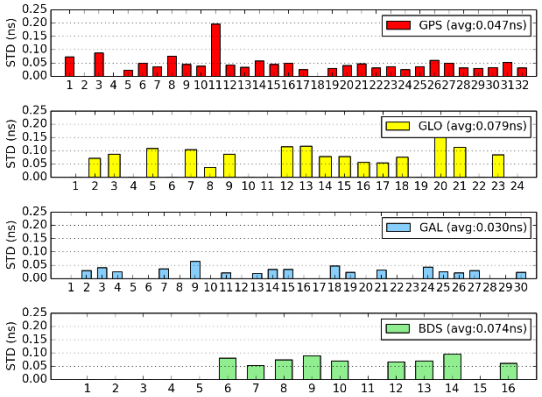

(a) Number of stations used: 100

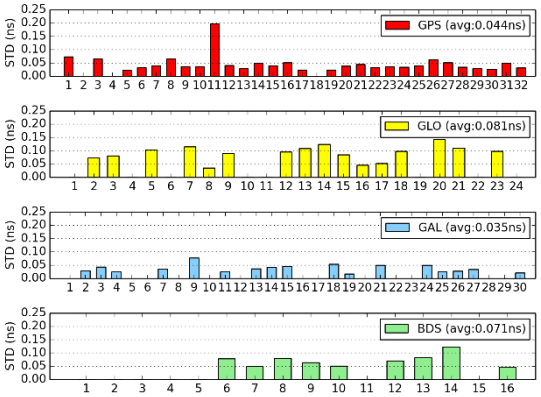

(b) Number of stations used: 70

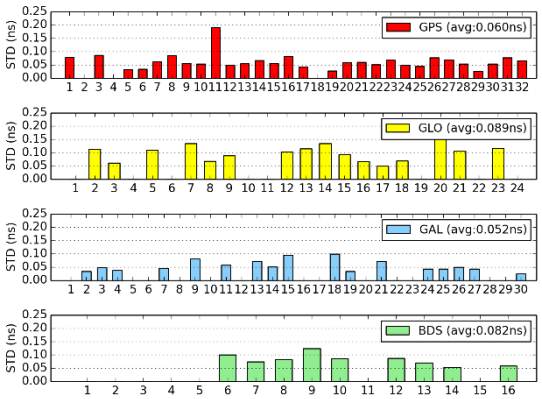

(c) Number of stations used: 40

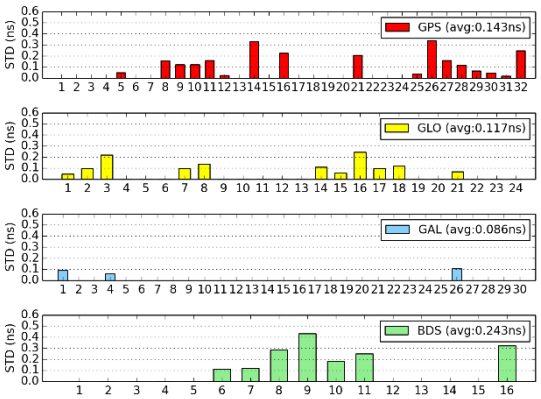

(d) Number of stations used: 10

Figure 5.5 Clock STDs with different configuration

Figures 5.6 and 5.7 present the results of all experimental groups, where Figure 5.6 shows the STD of the clock, and Figure 5.7 demonstrates product integrity. From these results, it can be seen that when the number of stations decreases to below 35, there is a notable decline in product accuracy; when the number falls below 40, product integrity is also compromised. The fundamental conclusion is that when the number of real-time stations drops below 40, we consider the product to be unreliable.

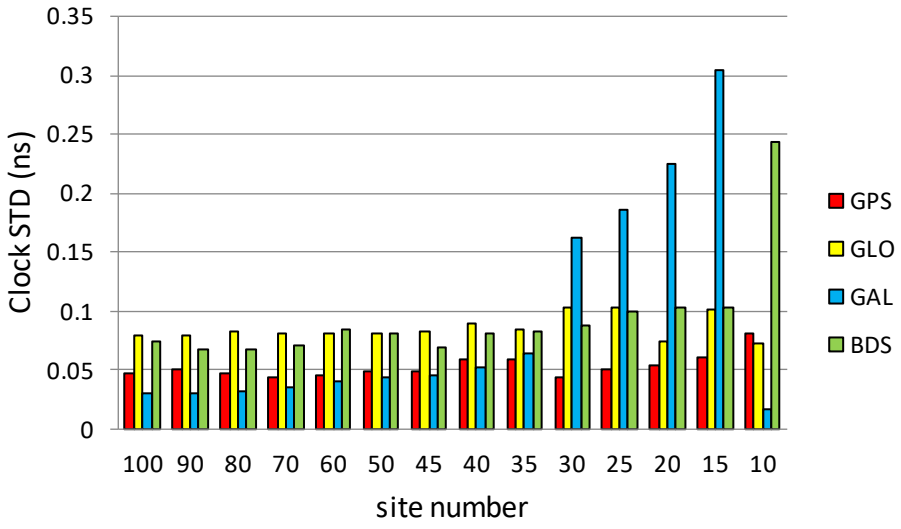

Figure 5.6 Clock STD for all experiment groups

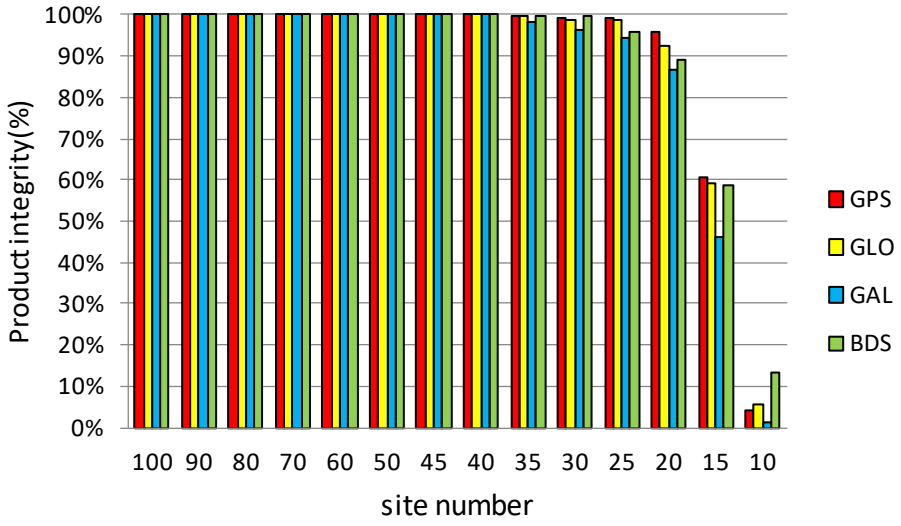

Figure 5.7 Product integrity for all experiment groups

5.3 Real-time UPD performance

In general, UPD estimation can utilize the same network for real-time clock estimation and apply epoch-by-epoch methods for real-time data processing. This section illustrates the

real-time UPD performance using a one-day solution estimated from real-time PPP float ambiguities as an example. It is important to note that, in the analysis presented in this section, the first two hours of UPD data are excluded from evaluation due to ongoing convergence of PPP ambiguities, rendering the UPD unreliable during this phase. Additionally, minor interruptions in UPD may occur due to stability issues with the data stream, primarily resulting from exclusions by the UPD quality control function. Ultimately, only MEO satellites from the BDS are utilized in the UPD estimation process. Figures 5.8 (a)-(c) respectively depict the WL UPD series for the GPS, Galileo, and BDS systems, while Figures 5.9 (a)-(c) illustrate the STD of the WL UPDs for each system. The results suggest that the WL UPDs remain relatively stable across all systems, with an accuracy within 0.05 cycles, and notably, the Galileo system demonstrates the highest UPD stability, maintaining an accuracy within 0.02 cycles. In all the series sub-plots, , different colors represent different satellites.

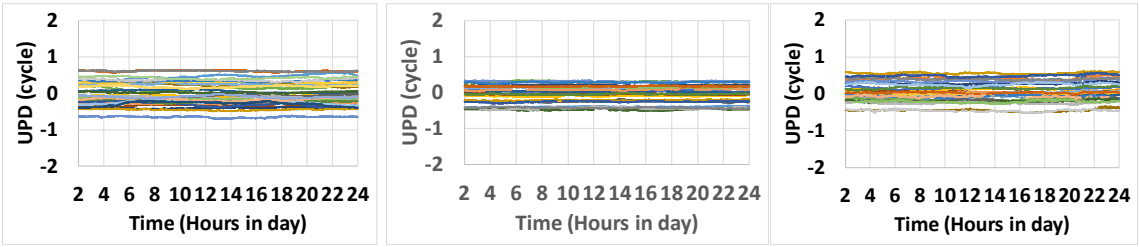

(a) GPS satellites (b) Galileo satellites (c) BDS satellites

Figure 5.8 WL UPD series

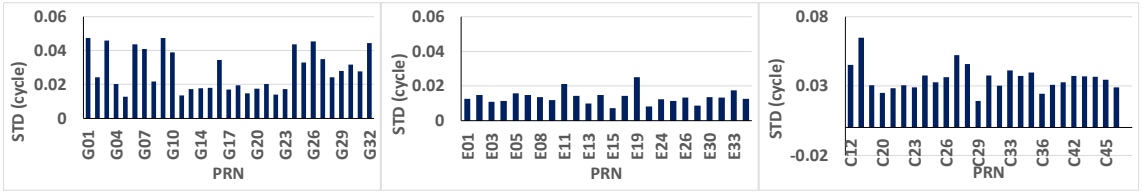

(a) GPS satellites (b) Galileo satellites (c) BDS satellites

Figure 5.9 WL UPD STD

Furthermore, Figures 5.10 (a)-(c) showcase the NL UPD series for GPS, Galileo, and BDS, and Figures 5.11 (a)-(c) present the STD of the NL UPDs for each system. The results show that NL UPDs exhibit more fluctuations compared to WL UPDs, yet the overall accuracy remains within 0.05 cycles.

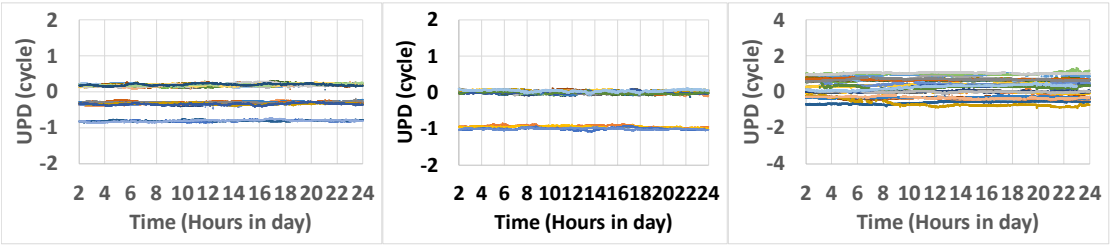

(a) GPS satellites (b) Galileo satellites (c) BDS satellites

Figure 5.10 NL UPD series

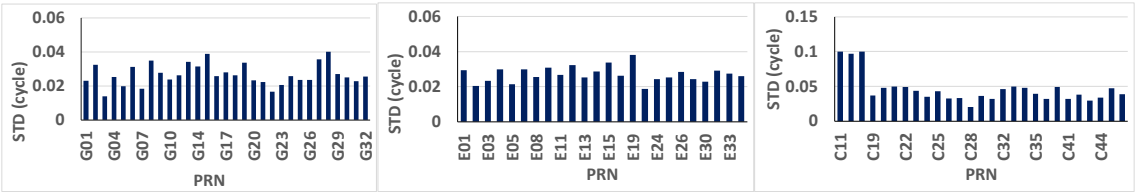

(a) GPS satellites (b) Galileo satellites (c) BDS satellites

Figure 5.11 NL UPD STD

5.4 Real-time positioning performance

In this section, a station from the Satellite Positioning Service of the German State Survey (SAPOS) network located in Germany is utilized to analyze the positioning performance of using difference strategies including real-time PPP and PPP-AR and PPP-RTK. Both the GPS and Galileo systems are supported by the SAPOS network. Due to the requirement of atmosphere delay augmentation information from nearby reference stations for PPP-RTK, this section first analyzes the accuracy of regional real-time atmosphere delay within the before delving into the positioning performance of various PPP strategies.

Figure 5.12 illustrates the distribution of used stations in the PPP experiment, where station 0266 is designated as a rover station, and stations 0256, 0265, and 0278 serve as reference stations. The spatial arrangement of these reference stations is such that the distance between each station is approximately 100 kilometers, forming a strategic network that supports the accuracy and reliability of the PPP-RTK services. It should be noted that the UPD calculations have been prepared in advance, utilizing data from approximately 30 stations. This foundational work underpins the analysis presented here, allowing us to focus on the demonstration and validation of PPP-RTK algorithm without delving into the specifics of UPD computation.

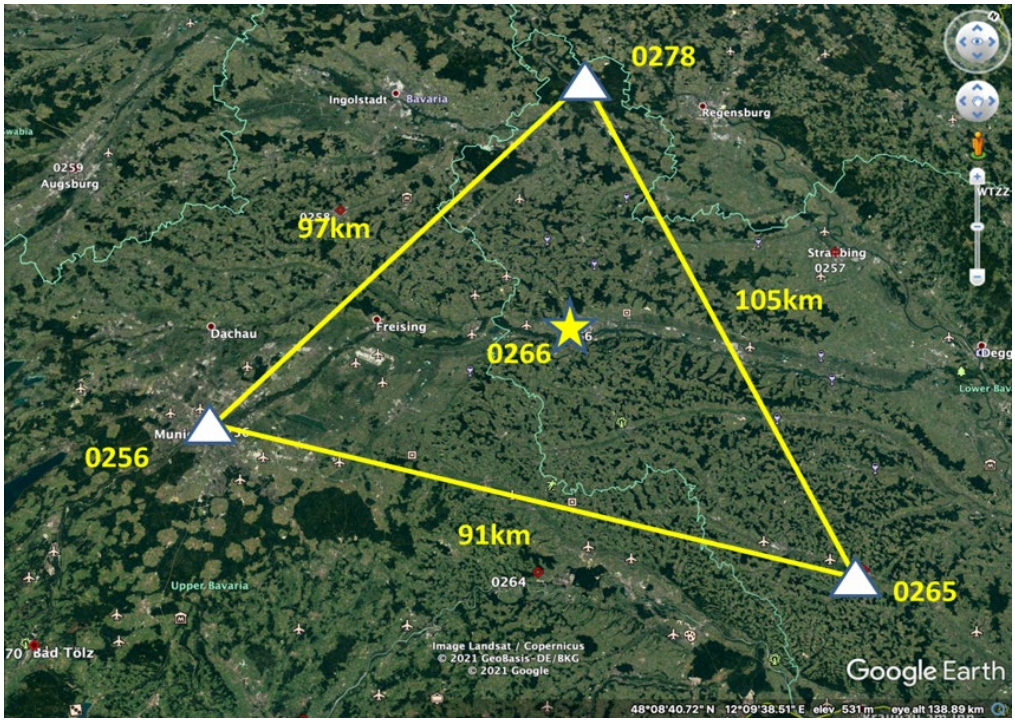

Figure 5.12 Site distribution of PPP-RTK experiment

Utilizing the methods outlined above, the slant ionospheric delays for each station are calculated separately. Taking the GPS as an example, Figures 5.13(a) -(d) depict the slant ionosphere delays extracted from each station after the ambiguities were resolved. Different colors in the figures represent results from different satellites. From these figures, it is observed that the trend of ionosphere delays across satellites exhibits consistency. This observation suggests a degree of spatial correlation in the ionosphere delays between different stations in a regional area.

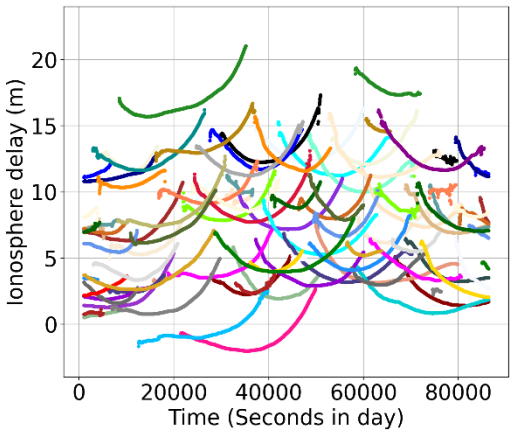

(a) Station 0256

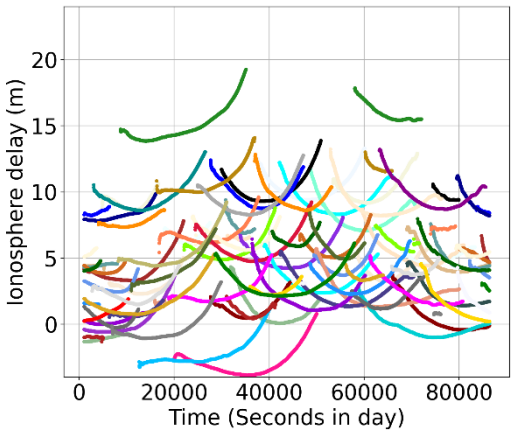

(b) Station 0265

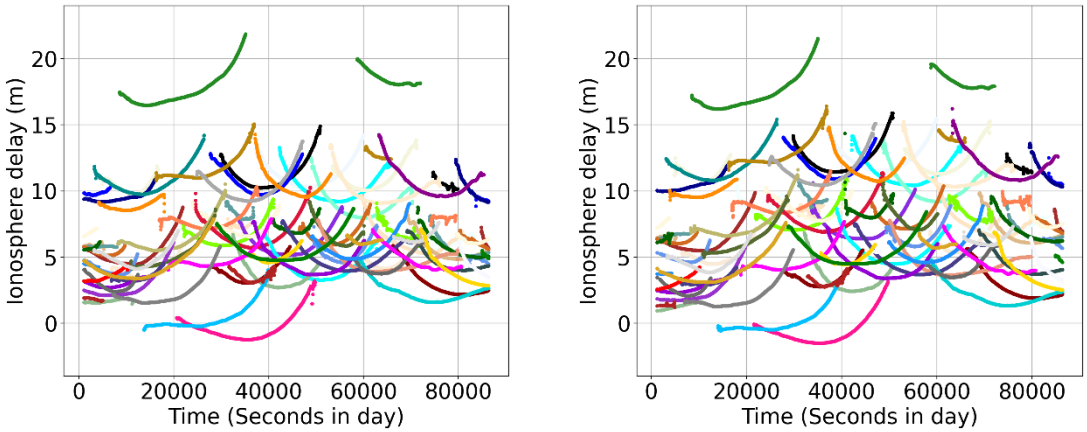

(c) Station 0266 (d) Station 0278

Figure 5.13 Slant ionosphere delay of station 0256, 0265, 0266 and 0278

Using the methods outlined in Equations (2.12) and (2.13) to interpolate the ionosphere delay of the rover station, and comparing it with that derived by PPP AR at the rover station, the differences are shown in Figures 5.14(a) and (b) for GPS and Galileo, respectively. The error of interpolation is less than 5cm, with an RMS of about 1cm. This demonstrates that the ionosphere delay interpolated for reference stations can accurately represent the ionosphere delay experienced by the rover station.

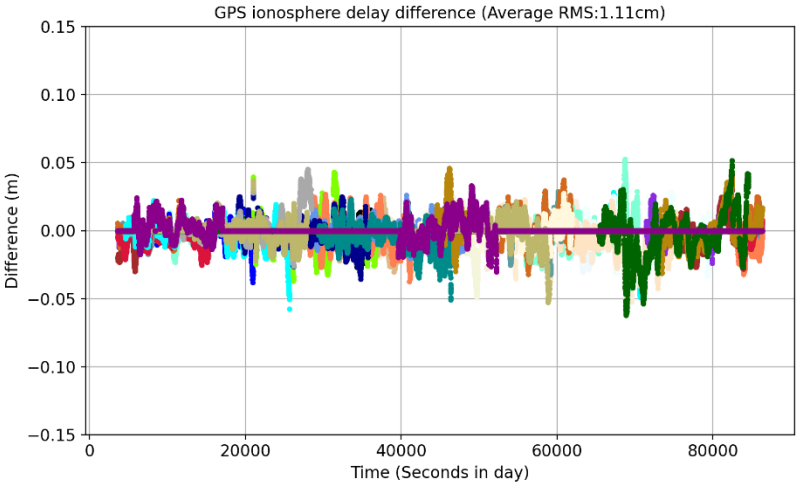

(a) Results of all GPS satellites

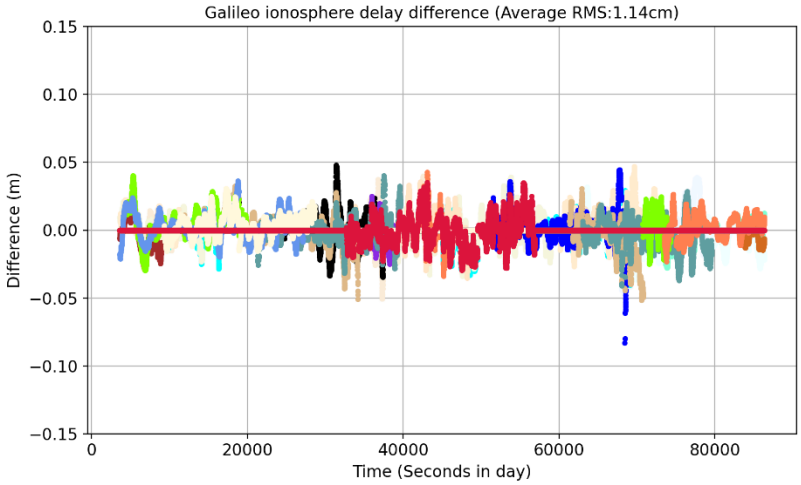

(b) Results of all Galileo satellites

Figure 5.14 Slant ionosphere error series of the station 0266

Similar to the ionosphere analysis, we conducted interpolation modeling of the zenith troposphere wet delay and compared it with that calculated by PPP AR at the rover station. Figure 5.15 illustrates the difference series. It can be observed that the error of the interpolated troposphere delay is generally within 2cm, with an RMS of less than 1cm. The high-precision modeling of atmosphere delays in this example opens up possibilities for regional augmentation on the rover side.

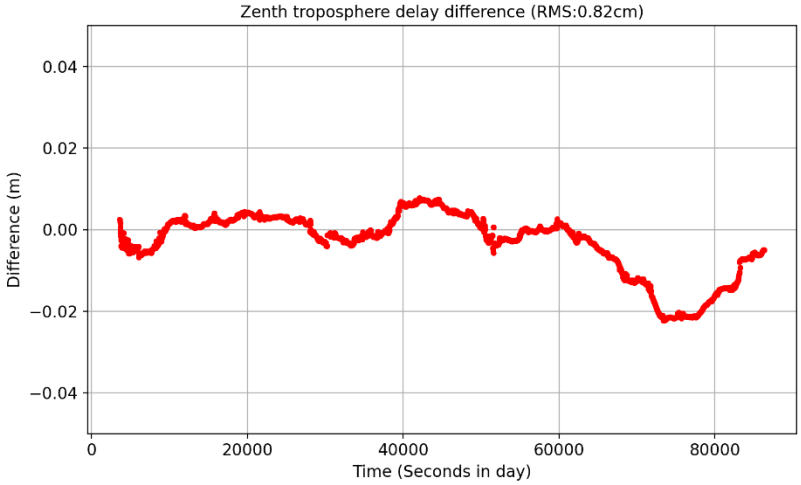

Figure 5.15 Zenith troposphere wet delay interpolation errors of the station 0266

Based on the ionosphere and troposphere products mentioned above, we conducted PPP validation for clients. Figures 5.16(a), (b), and (c) showcase the positioning results for rover stations using PPP, PPP-AR, and PPP-RTK, respectively. The filter was restarted every hour, and we compiled positioning results from 1:00 to 23:59. Due to the semi-real-

time processing mode adopted, UPD still needed to converge before 1:00, hence positioning results before this time were not listed. From the figures, it is evident that the main contribution of PPP-AR is the enhancement of positioning accuracy as well as the acceleration in convergence time. Meanwhile, the significant contribution of regional atmosphere augmentation lies in its substantial reduction of convergence time. It is clear from the PPP-RTK result in this example that PPP-RTK exhibits virtually no convergence time. The average positioning accuracies of PPP, PPP-AR, and PPP-RTK are 3.2 cm, 3.1 cm, and 4.9 cm; 1.5 cm, 2.4 cm, and 2.8 cm; and 0.6 cm, 0.6 cm, and 2.2 cm in the north, east, and up directions, respectively, based only on the results after convergence.

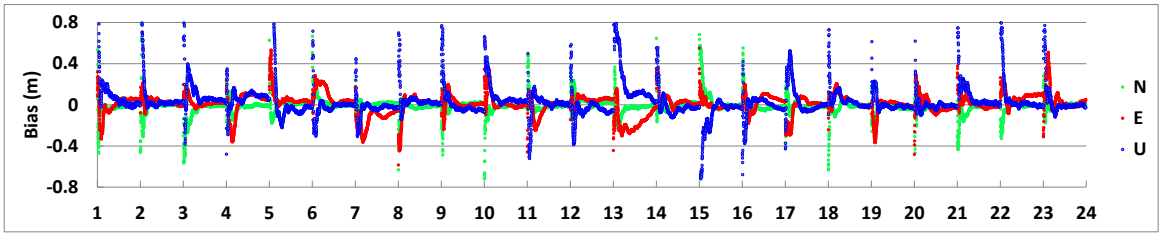

(a) PPP results

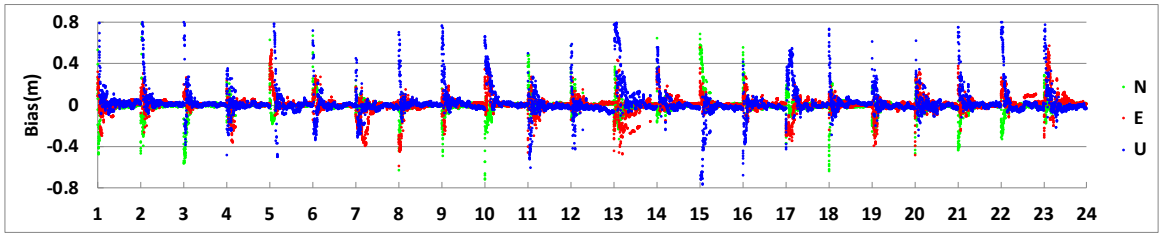

(b) PPP-AR results

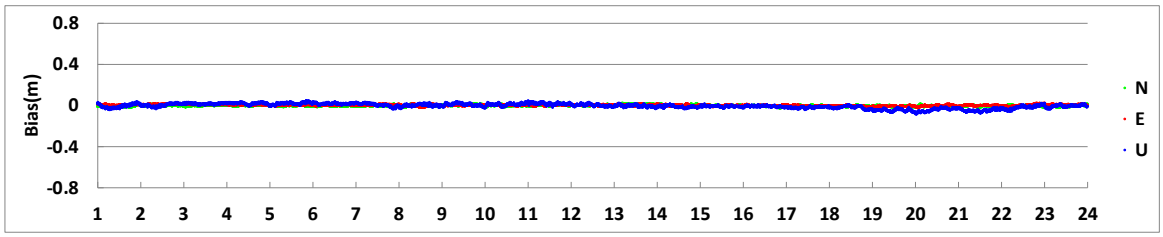

(c) PPP-RTK results

Figure 5.16 Real-time positioning results of the station 0266

The density of the augmentation network plays a critical role in determining the performance of PPP-RTK. In high-latitude regions, where ionospheric activity is relatively low and exhibits greater stability, a sparser network of reference stations, with inter-station spacing ranging from 100 to 200 km, is generally adequate to provide reliable corrections. Conversely, in mid- and low-latitude regions, characterized by heightened and more dynamic ionospheric activity, a denser reference station network is essential. In such regions, inter-station distances should be reduced to approximately 50 km to adequately

capture the rapid spatial and temporal variations in ionospheric delays. This variation in network density requirements underscores the need to optimize augmentation infrastructure based on the geophysical characteristics of the region, ensuring precise and robust PPP-RTK performance.

5.5 Summary

This chapter delves into the GFZ RTPPS, detailing the architecture and functionality of the real-time GNSS precise positioning services. It is structured into server-side and client-side components. The server-side manages real-time POD, PCE, UPD estimation, and the generation of regional atmospheric information. In contrast, the client-side implements a variety of real-time precise positioning algorithms, including PPP, PPP-AR, and PPP-RTK. The analysis rigorously examines the capabilities and performance of these components, particularly emphasizing the accuracy of orbit and clock, the impact of network configuration on clock estimation, and the effectiveness of UPD products. Additionally, the chapter assesses proficiency in atmosphere modeling and various PPP positioning models on the client-side, demonstrating the extensive capabilities of the system in real-time precise positioning with regional augmentation. Real-time positioning experiments have demonstrated that PPP-AR significantly accelerates convergence times and enhances positioning accuracy. Moreover, PPP-RTK further reduces convergence times compared to PPP-AR. Especially in accordance with the experimental results presented in this chapter, the utilization of regional atmospheric information enables PPP to effectively shorten convergence times.

The author's contributions in this chapter encompass the development of real-time UPD, regional augmentation, and PPP modules within GFZ RTPPS system. These components, working in coordination with the RTPPS orbit and clock modules, form a comprehensive real-time GNSS precise positioning service system.

6 Real-time GNSS Applications in Geoscience

6.1 Introduction

The advent of high-precision, real-time GNSS applications represents a significant breakthrough in the proactive monitoring and early detection of natural hazards such as earthquakes and tsunamis. This transformative technology is increasingly recognized for its pivotal role in enhancing our ability to respond preemptively to these catastrophic events, thereby mitigating their impact on human lives and infrastructure.

This chapter introduces the application of the RTPPS within the framework of the EWRICA project, highlighting its critical role in hazard monitoring and early warning systems. The RTPPS serves as a foundational platform for real-time hazard assessment, enabling rapid and effective responses to potentially devastating events. Building upon the robust capabilities of RTPPS, the RTPM system has been meticulously designed and developed to further advance the detection and monitoring of natural hazards.

Through real-time data acquisition and processing, the RTPM system provides early warnings essential for risk mitigation and damage reduction. While precise earthquake predictions remain unattainable, the system detects initial seismic waves (P-waves) within seconds of an event and issues warnings before the arrival of more destructive secondary waves (S-waves). These warnings can reach populations in a broader area, spanning several hundred kilometers from the epicenter, typically within the first one or two minutes after the initial shock. This allows critical infrastructure, such as power plants and dams, to initiate protective measures, such as shutting down systems or entering warning modes, while giving individuals in affected regions valuable time to take safety precautions. The integration of these systems within the EWRICA project reflects a comprehensive approach to hazard monitoring, merging cutting-edge technological tools with practical applications to strengthen resilience against natural disasters.

This chapter further provides an in-depth examination of the RTPM system’s architecture and functionality. Using the EWRICA project as a case study, it explores specific examples of GNSS-based monitoring to demonstrate how this technology is effectively applied to reduce the impact of natural disasters. These examples underscore the sophisticated interplay between advanced technology and geoscience, fostering a deeper understanding of the dynamic processes shaping our planet's geological landscape and illustrating the transformative potential of GNSS in disaster risk management.

6.2 RTPM system

The RTPM system is a prime example of GNSS technology integrated into geoscience applications, particularly for earthquake detection and analysis. It is meticulously organized into three critical components: the real-time PPP module, the database module, and the website module. Figure 6.1 illustrates the functionality of each module and their interrelationships.

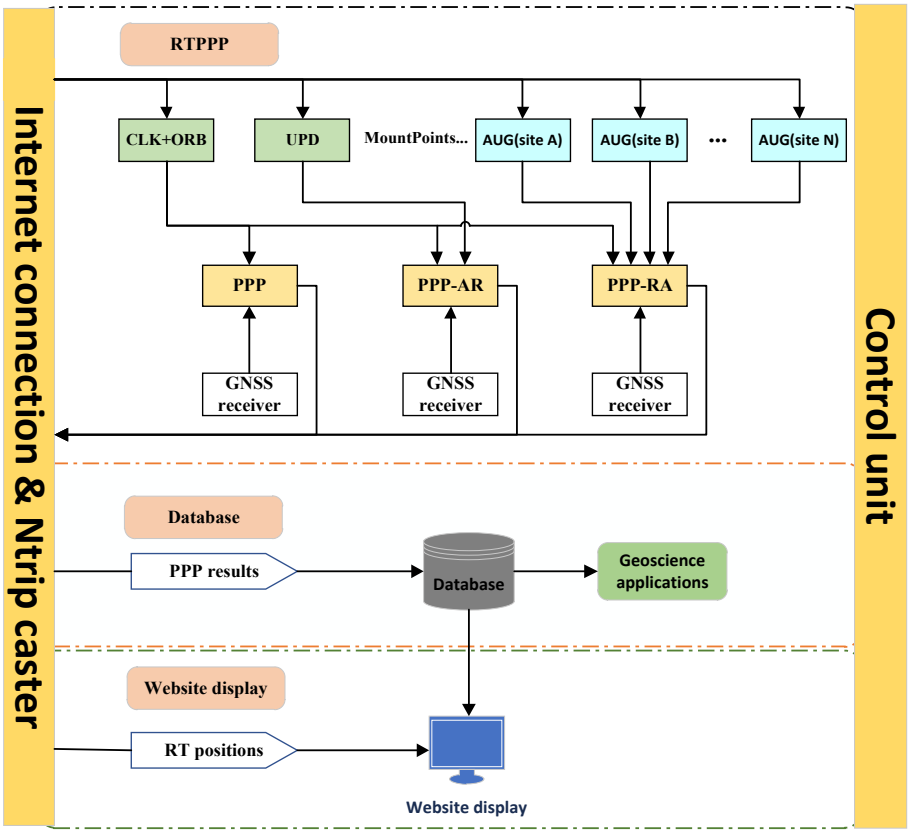

Figure 6.1 The structure of the RTPM system

6.2.1 RTPPP software

The Real-Time Precise Point Positioning (RTPPP) software is the technological heart of the RTPM system. It enables the utilization of signals from an array of satellite constellations including GPS, GLONASS, Galileo, and BDS, thus enhancing positional accuracy and reliability.

It supports various positioning algorithms including PPP, PPP-AR and PPP-RTK in both static and kinematic mode and provides products of comprehensive output options from coordinate series to receiver clock, ISB, ambiguities, and atmosphere delays, ensuring a holistic overview of positioning data.

As part of the data processing workflow, users are afforded the convenience of visual aids directly on the user interface. These aids include detailed logs, which offer insight into the operational specifics and data flow during the processing phase, and dynamic real-time positioning sequence diagrams that visually represent the positioning data as it evolves over time. Such graphical representations are invaluable for both monitoring and analysis purposes.

6.2.2 Data management

The database module acts as a secure and scalable repository, archiving the voluminous and continuous stream of geospatial data generated by the GNSS sensors. This repository is crucial for long-term data analysis and pattern recognition, playing a key role in the study of tectonic movements and contributing to the predictive modeling of seismic activities.

In the context of the RTPM system, the PostgreSQL software is used as a crucial component, focusing on data storage. This strategic choice leverages PostgreSQL's advanced capabilities to manage, store, and ensure the integrity of the real-time data generated by the RTPM system. The integration of PostgreSQL into the RTPM system architecture is not merely a technical decision but a strategic one, emphasizing the importance of robust data management in real-time monitoring applications. PostgreSQL's exceptional handling of concurrent transactions and its support for advanced data types make it an ideal solution for managing the voluminous and complex data streams produced by RTPM system. By adopting PostgreSQL, the RTPM system benefits from enhanced scalability, reliability, performance optimization, and cost-effectiveness.

6.2.3 Real-time monitoring website

The website display module serves as the interactive face of the RTPM system. It is crafted to present the real-time geospatial data in an accessible and user-friendly manner, offering both the scientific community and public stakeholders a visual representation of seismic activities as they unfold. Through dynamic maps and real-time data feeds, the module ensures that the critical information is not only disseminated swiftly but also rendered in a format that facilitates immediate interpretation and action.

6.3 Implementation in EWRICA project

6.3.1 Introduction of EWRICA project

Countries like Japan, the United States, and Chile are leading the integration of GNSS networks into their early warning systems, demonstrating a proactive stance in disaster

preparedness and risk mitigation. In contrast, European nations including Italy and Greece, while committed to leveraging GNSS technology for natural hazard mitigation, continue to face challenges in implementing practical, real-time solutions. Despite these challenges, the intent to strengthen GNSS networks across Europe is evident. This is further exemplified by Portugal, Spain, and other European countries, showing a keen interest in adopting GNSS-based monitoring systems. The growing availability of GNSS infrastructure in these regions points to a promising future where advanced technologies are implemented for real-time monitoring and early warning of natural hazards, thus enhancing the scope for preventive measures and timely responses.

Within this context, the EWRICA project aims to incorporate GNSS into the Mediterranean Tsunami Warning Systems (TWS) and for the rapid assessment of regions at high risk for severe ground motion and landslides, supporting "Rapid Response" activities. The project's primary objective is to develop a prototype of a GNSS-based fast source inversion and ground motion parameter derivation platform tailored for the existing GNSS-Networks in Italy and Greece. This platform, eventually extendable to other regions in the Mediterranean and globally, seeks to create robust local ground motion models shortly after an earthquake to assess secondary effects such as tsunamis and landslides, and to pinpoint areas likely to suffer building damage and collapse.

This goal will be achieved by enhancing the accuracy of real-time GNSS processing, which includes the use of collocated sensors (GNSS and accelerometers) and integrating near-field seismic-geodetic data into real-time source inversion. A fast and robust kinematic source inversion procedure will be developed that integrates GNSS, broadband, and strong motion data in real-time. This joint inversion of near-field data will not only refine the assessment of seismic moment, hypocenter, and rupture kinematics but will also expedite the derivation of source parameters compared to traditional far-field data processing. The improved source assessment will enable more reliable predictions of ground motion, which in turn, will enhance forecasts of secondary effects like landslides and tsunami generation. Consequently, the project plans to provide probabilistic estimates for medium and short-period ground shaking parameters, tsunami wave heights, and potential slope instabilities within minutes after an earthquake. Figure 6.2 illustrates the connections and data flow among the various work packages within the EWRICA project.

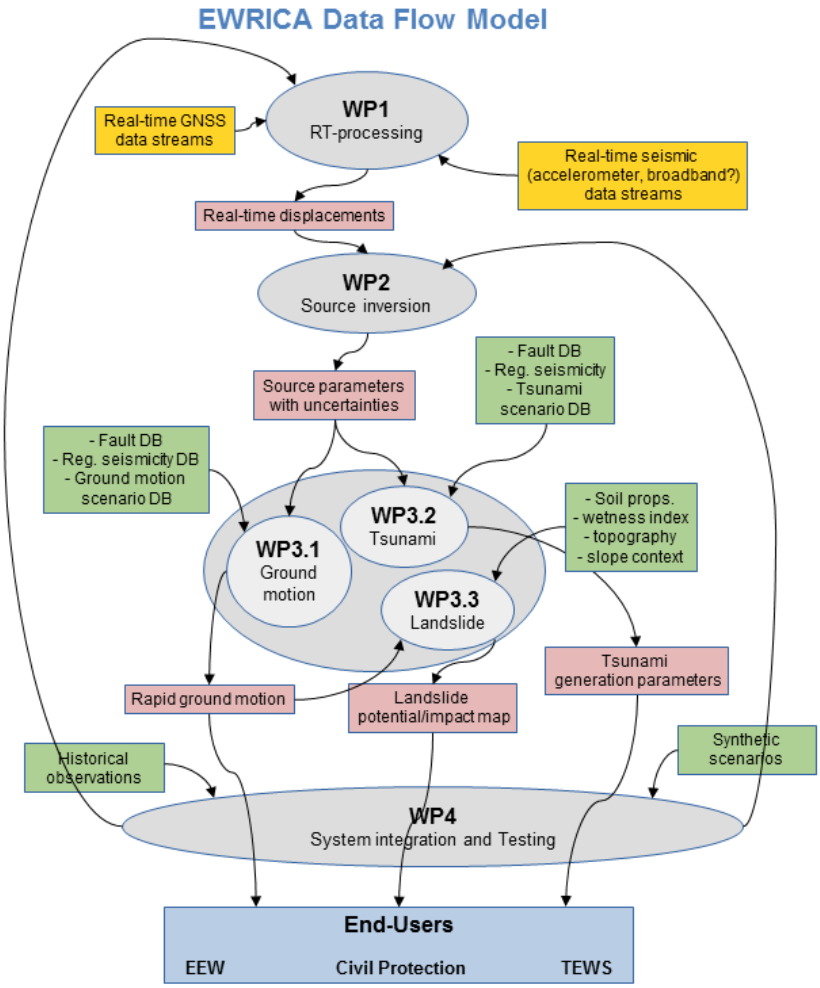

Figure 6.2 Connections and data flow between the individual work packages

The RTPM system is built into Working Package 1 (WP1), providing precise real-time surface displacement information to other WPs. The principal objective here is to optimize the use of ground motion data for the rapid derivation of earthquake source parameters using real-time PPP and PPP-AR techniques, enabling the precise determination of station positions with respect to reference stations in the global GNSS network. Further precision and quicker convergence are sought through PPP-RTK by utilizing regional GNSS networks to mitigate correlated error sources like satellite orbit uncertainties or troposphere delay modeling. Moreover, the project incorporates multi-GNSS joint processing (GPS, GLONASS, Galileo, and BDS), aiming to deliver even more precise and robust solutions while enhancing the precision and reliability information of ground displacements.

Figure 6.3 showcases the data processing strategy of the RTPM system in the EWRICA project and its integration with other WPs. All data are streamed through NTRIP. In the processing of GNSS data, the workflow begins with the acquisition of raw observations, followed by the simultaneous computation of PPP solutions and UPD. These UPDs are then relayed back to the server. Utilizing both UPD and raw data, AUG corrections are calculated alongside the PPP-AR solutions and are also sent back to the server. Eventually, the monitoring rover stations, upon receiving UPD and AUG corrections, realizes the PPP-RTK solution which then serves as an input for joint processor of GNSS and seismometer Data. This intricate system illustrates the layered approach to precise geospatial data computation, necessary for delivering accurate and timely warnings through the system.

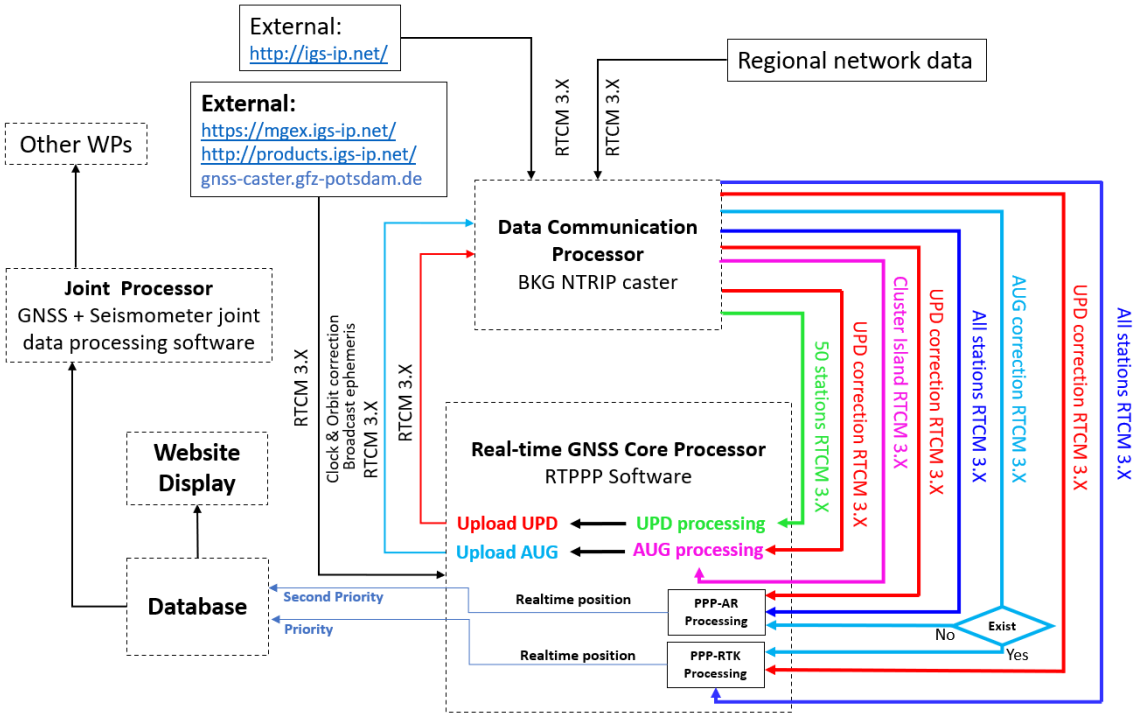

Figure 6.3 Data processing strategy in the EWRICA project

6.3.2 Implementation in the RING network in Italy

The RTPM system has been deployed within Italy's National GPS Integrated Network (RING, http://ring.gm.ingv.it/), where it provides high-accuracy, real-time positioning information for earthquake monitoring. Figure 6.4 depicts the distribution of the 228 measuring stations within the RING network. During the testing phase, it was observed that approximately 100 stations were capable of delivering a stable real-time data stream. As most of these real-time stations support only a single GPS system, the decision was made to utilize the single GPS system for the real-time experiment.

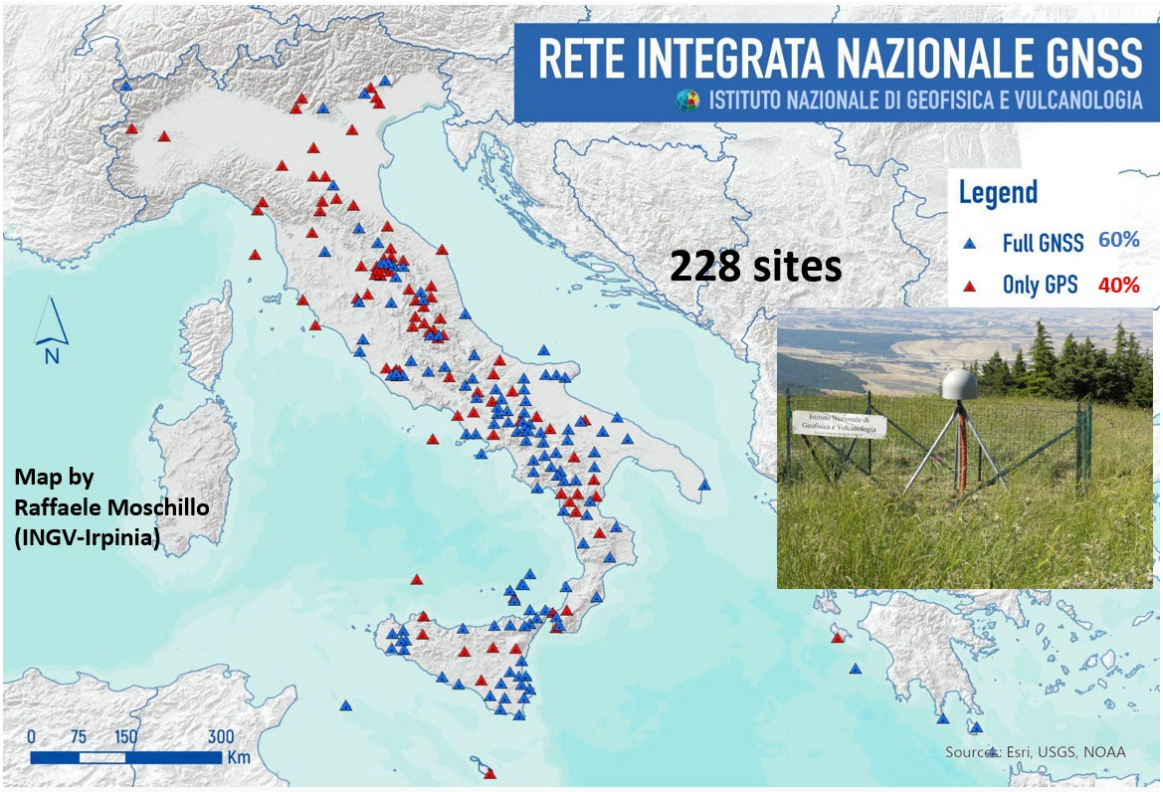

Figure 6.4 Site distribution of the RING network in Italy

6.3.3 Implementation in the BIG network in Indonesia

Additionally, the RTPM system is deployed in the BIG network in Indonesia. Figure 6.5 shows the distribution of GNSS stations in Indonesia, with over 200 stations already operational and providing real-time data streams.

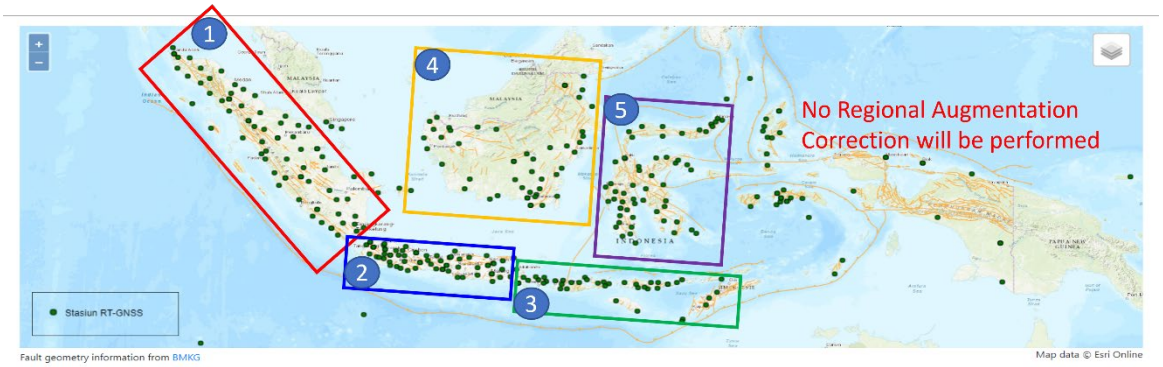

Figure 6.5 Site distribution of the BIG network in Indonesia

It should be noted that due to Indonesia's elongated terrain and the active ionosphere in the mid to low latitude regions, the country is divided into five smaller sub-regions for practical deployment. Each sub-region independently calculates the UPD and atmospheric

augmentation corrections. However, the specific data processing algorithm is the same for each sub-region.

6.3.4 Positioning performance

Taking the results from the Italian RING network on June 20, 2021, as an example, Figure 6.6 (a) presents the Time To First Fix (TTFF) for the PPP-RTK positioning results at each station within the RING network. Generally, aided by regional atmospheric augmentation techniques, the majority of stations achieve a TTFF of less than 20 seconds, indicating rapid initial positioning capability. In contrast, Figure 6.6 (b) - (d) reveals the positioning accuracy metrics, where the precision is quantified within a 1-sigma deviation. Remarkably, this accuracy amounts to about 1 cm in the horizontal plane and 3 cm in the vertical dimension. These results demonstrate the RTPM system's capability to provide real-time high accuracy for earthquake monitoring.

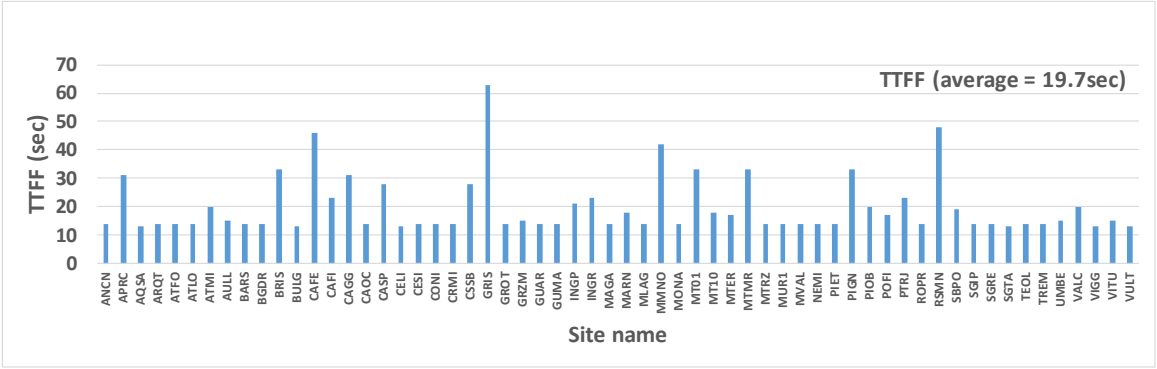

(a) TTFF

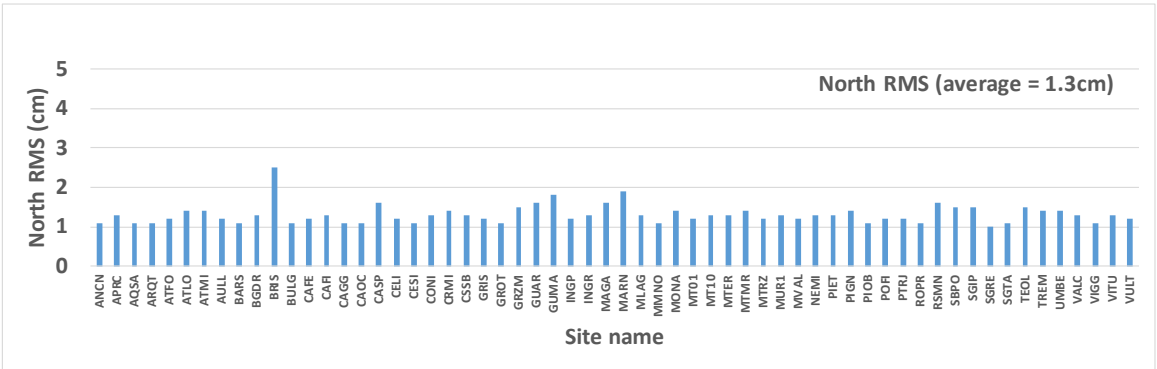

(b) North RMS

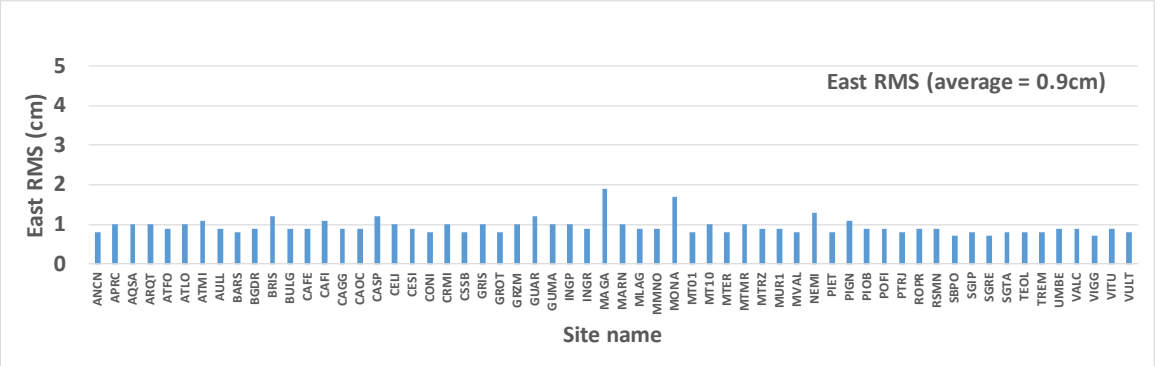

(c) East RMS

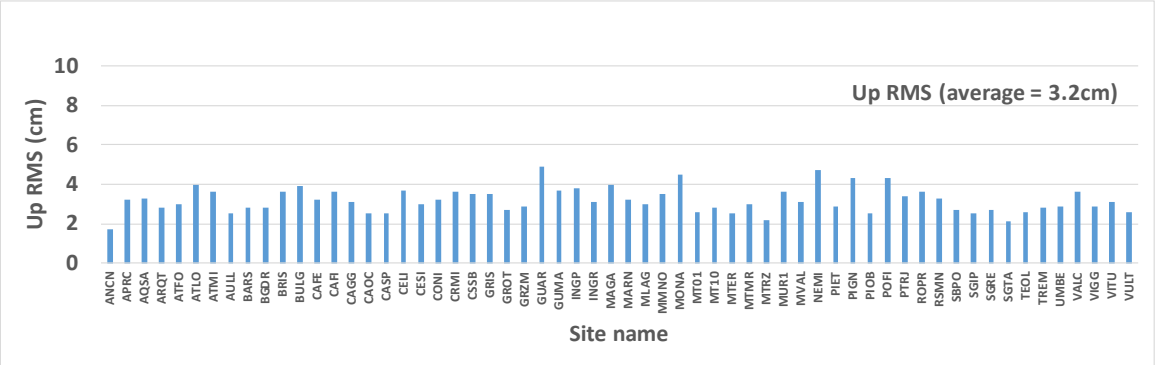

(d) Up RMS

Figure 6.6 PPP-RTK Performance of the RING network

Due to Indonesia's location in a low-latitude region, a significant characteristic is the active ionosphere, which results in a slight decrease in positioning performance compared to Germany and Italy. Taking the CKTF station as an example shown in Figure 6.7, the positioning accuracy is roughly double that of the RING network stations, with 2 cm in the horizontal plane and 6 cm in elevation. Optimizing real-time positioning performance in low-latitude areas remains a subject for further research.

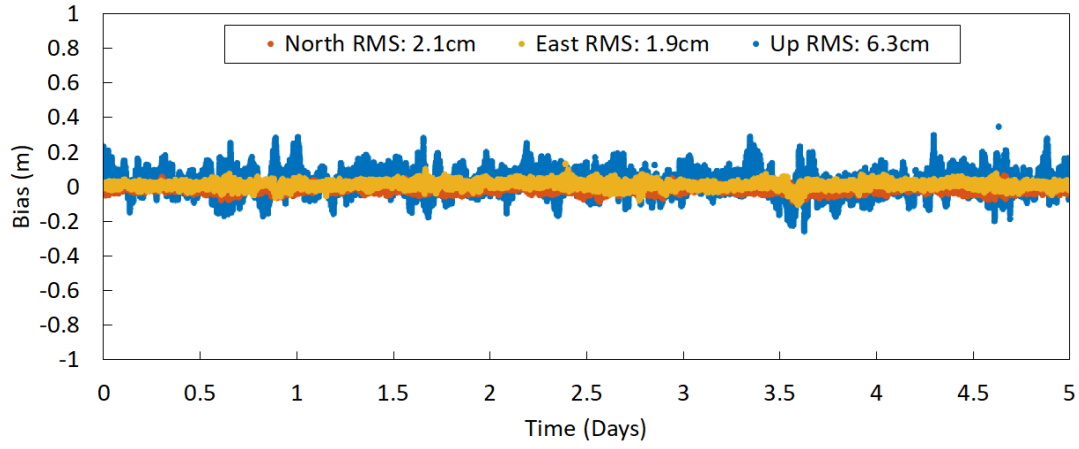

Figure 6.7 PPP-RTK result of CKTF station in the BIG network

Figure 6.8 presents an example of an earthquake that occurred in central Italy on October 30, 2016 (Avallone et al. 2016), to illustrate the surface displacement results processed by RTPM. The earthquake had a magnitude of 6.5 and a focal depth of 9.2 km, with the GNSS monitoring station located approximately 10 km from the epicenter. The data processing mode was near real-time. To enhance the clarity of displacement in the figure, a 0.5-meter offset was added to the north direction and a -0.5-meter offset was added to the east direction. From the figure, it is evident that the system can effectively capture the surface displacement information caused by the earthquake.

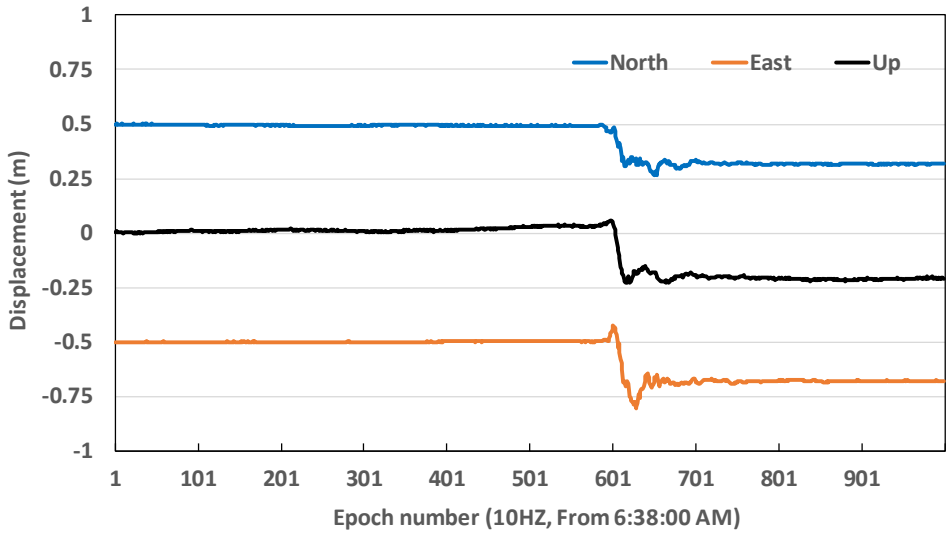

Figure 6.8 Surface displacement during the earthquake

6.4 Summary

This chapter comprehensively explores the application of real-time high-precision GNSS technology in earthquake monitoring and management. It first introduces the significance of high-precision GNSS technology in the field of geosciences, emphasizing its crucial role in the monitoring and management of natural disasters. Subsequently, it focuses on the application of the RTPM system within the EWRICA project and its pivotal role in earthquake activity monitoring. Designed specifically for earthquake monitoring, the RTPM system integrates real-time PPP modules, database modules, and website modules to provide robust support for achieving high-precision, real-time earthquake monitoring and analysis. Additionally, through case studies such as the EWRICA project, Italy's RING network, and Indonesia's BIG network, it showcases the potential of PPP-RTK technology in earthquake monitoring across different environments. The deployment and application

of the RTPM system signify significant advancements in real-time GNSS technology in the field of earthquake monitoring, providing crucial tools for disaster monitoring and early warning, and contributing positively to earth science research and disaster management. Through the discussions in this chapter, a deeper understanding of the role of real-time high-precision GNSS technology in earthquake monitoring and its importance in disaster prevention and response is gained.

7 Conclusions and Outlooks

7.1 Conclusions

This study presents a comprehensive investigation into real-time high-precision satellite clock estimation within multi-GNSS systems, introducing innovative methodologies that enhance the accuracy and practicality of GNSS applications in geosciences and related fields. The main contributions of this research are summarized as follows:

A novel approach is proposed to rapidly recover real-time satellite clock estimates following service interruptions by utilizing historical observations and filter state information. Experimental results demonstrate that by leveraging historical data for post-processing, recovery time is reduced by approximately 90%, as it eliminates waiting times for real-time data and processing interval limitations. Moreover, integrating historical state information further accelerates the recovery process, enabling service restoration within just 5 minutes. This significant reduction in downtime is particularly advantageous for real-time PPP users, enhancing system availability and reliability.

A novel decentralized clock estimation strategy is developed that maintains the accuracy of traditional methods while dramatically reducing computation time per epoch, from over 5 seconds to approximately 0.1 seconds. This breakthrough enables high-frequency clock updates at 1 Hz or even 10 Hz, crucial for applications requiring frequent clock updates, such as real-time disaster monitoring and other high-frequency tracking scenarios. Notably, the computational efficiency of this method remains largely unaffected by increasing station and satellite numbers, ensuring scalability for future GNSS advancements. Its decentralized nature further strengthens system robustness: high-accuracy, high-frequency real-time clock products can still be delivered as long as at least one UD clock and one ED clock remain operational.

Building on the advancements in real-time clock estimation, the GFZ RTPPS system has been further enhanced to offer more reliable services for real-time PPP users, while contributing to the IGS. Results show that GPS and Galileo clock accuracy in routine services exceeds 0.1 ns, positioning it competitively among other IGS analysis centers. Additionally, a client-side module has been developed to support real-time UPD estimation, regional atmospheric corrections, and real-time positioning applications such as PPP, PPP-AR, and PPP-RTK. Results confirm that the system meets the centimeter-level accuracy

requirements of real-time PPP clients, with PPP-RTK achieving near-instantaneous convergence.

High-accuracy real-time GNSS techniques have also been successfully applied to geoscientific research. The RTPM system has been developed for real-time precise Earth surface displacement monitoring in seismic applications, already deployed in multiple regions including the RING network in Italy and the BIG network in Indonesia. Results indicate that, in the RING network, the system delivers real-time displacement solutions with an accuracy of approximately 1 cm horizontally and 3 cm vertically. In regions with high ionospheric activity, such as Indonesia, vertical accuracy may degrade by a factor of two. This highlights the immense potential of GNSS in advancing real-time geoscience applications.

In conclusion, this research represents a significant advancement in real-time GNSS satellite clock estimation, introducing innovative methodologies that enhance computational efficiency, reliability, and practical usability. The proposed techniques not only improve the performance of real-time PPP services but also extend the application of high-accuracy GNSS solutions to critical fields such as geosciences and disaster monitoring. The successful deployment of these methods in real-world systems, including seismic monitoring networks, underscores their practical impact and adaptability. These contributions provide a solid foundation for future research, paving the way for ongoing advancements in real-time GNSS positioning and its increasingly vital role in scientific and engineering applications.

7.2 Outlooks

Looking to the future, this dissertation proposes the following research and technology development directions:

(1) Support for more constellations and frequencies: This study currently supports only GPS, GLONASS, Galileo, and BeiDou satellites, with a primary focus on dual-frequency data processing. However, as the global GNSS landscape evolves with the introduction of additional constellations and new frequencies, such as those offered by emerging systems and Low Earth Orbit (LEO) satellites, there is an increasing need to extend the system's capability to handle more than two frequencies. The future will likely see the proliferation of new signals from various satellites, and incorporating these will enhance the flexibility and accuracy of real-time positioning services. Expanding the algorithms and data processing systems introduced in this dissertation will be crucial to accommodate the

increasing variety of signals. This will not only improve positioning performance but also strengthen system resilience in challenging environments, such as urban canyons and areas with obstructed satellite visibility.

(2) Integration of real-time orbit determination: This research primarily focuses on improving real-time clock estimation, while real-time orbit determination still relies on prediction algorithms. One limitation of using predicted orbits is that they may experience orbit switching jumps and certain delays, which can degrade the performance of real-time positioning systems. Future research could explore the integration of real-time orbit estimation into the processing framework. By developing dedicated algorithms for real-time orbit determination, errors from orbital prediction models could be mitigated. It is important to note that the methods introduced in this study for real-time clock estimation can also be adapted for real-time orbit determination. Furthermore, this integration would reduce dependence on external orbit prediction sources, enhancing the robustness of real-time positioning systems, particularly in regions with limited GNSS satellite visibility.

(3) Advanced error modeling: This study employs relatively simple error modeling approaches, such as linear interpolation for ionosphere and troposphere delays, and does not address multipath effects. While these methods provide basic error correction, they are insufficient in complex environments where such effects are more pronounced, such as urban canyons or areas with dense foliage. With the rapid advancement of Artificial Intelligence (AI) technologies, future research could explore their potential to develop more accurate and dynamic error models. AI could be used to process large datasets and identify patterns in ionospheric, tropospheric, and multipath errors, thereby improving GNSS positioning accuracy in challenging conditions. Additionally, machine learning techniques, such as deep learning, could aid in real-time error detection, anomaly resolution, and model optimization, allowing the system to better adapt to unpredictable environmental changes. The application of AI and machine learning could significantly enhance real-time error prediction and correction, leading to more reliable and accurate GNSS solutions across a broad spectrum of applications, from geoscience to autonomous navigation.

Through the exploration and implementation of these future directions, the technology behind real-time GNSS positioning is expected to evolve significantly, offering more precise, flexible, and robust solutions for a variety of sectors. These advancements could greatly benefit critical areas such as disaster monitoring, transportation, and geoscientific research, ultimately contributing to the continued progress of global positioning and navigation technologies.

References

Alcay, S., & Turgut, M. (2021). Evaluation of the positioning performance of multi-GNSS RT-PPP method. Arabian Journal of Geosciences, 14, 1-19, doi: 10.1007/s12517-021-06534-4.

Allahvirdi-Zadeh, A., Wang, K., & El-Mowafy, A. (2021). POD of small LEO satellites based on precise real-time MADOCA and SBAS-aided PPP corrections. GPS solutions, 25(2), 31, doi: 10.1007/s10291-020-01078-8.

Avallone, A., Latorre, D., Serpelloni, E., Cavaliere, A., Herrero, A., Cecere, G., ... & Selvaggi, G. (2016). Coseismic displacement waveforms for the 2016 August 24 Mw 6.0 Amatrice earthquake (central Italy) carried out from High-Rate GPS data. Annals of Geophysics, doi: 10.4401/ag-7275

Bahadur, B., & Nohutcu, M. (2019). Comparative analysis of MGEX products for post-processing multi-GNSS PPP. Measurement, 145, 361-369, doi: 10.1016/j.measurement.2019.05.094.

Bar-Sever, Y., Blewitt, G., Gross, R. S., Hammond, W. C., Hsu, V., Hudnut, K. W., ... & Webb, F. (2009, December). A GPS real time earthquake and Tsunami (GREAT) alert system. In AGU Fall Meeting Abstracts (Vol. 2009, pp. G21A-02).

Bar-Sever, Y., Young, L., Stocklin, F., Heffernan, P., & Rush, J. (2004, December). The NASA global differential GPS system (GDGPS) and The TDRSS Augmentation Service for Satellites (TASS). In ESA 2nd workshop on navigation user equipment.

Bertiger, W., Bar-Sever, Y., Dorsey, A., Haines, B., Harvey, N., Hemberger, D., ... & Wil lis, P. (2020). GipsyX/RTGx, a new tool set for space geodetic operations and resear ch. Advances in space research, 66(3), 469-489, doi: 10.1016/j.asr.2020.04.015.

Bierman, G. J. (2006). Factorization methods for discrete sequential estimation. Courier C orporation.

Blewitt, G. (1990). An automatic editing algorithm for GPS data. Geophysical research letters, 17(3), 199-202, doi: 10.1029/GL017i003p0019.

Blewitt, G., Bertiger, W., & Weiss, J. P. (2010, June). Ambizap3 and GPS carrier-range: a new data type with IGS applications. In Proceedings of IGS workshop and vertical rates, Newcastle, UK (Vol. 28).

Blewitt, G., Kreemer, C., Hammond, W. C., Plag, H. P., Stein, S., & Okal, E. (2006). Rapid determination of earthquake magnitude using GPS for tsunami warning systems. Geophysical Research Letters, 33(11), doi: 10.1029/2006GL026145.

Bock, H., Dach, R., Jäggi, A., & Beutler, G. (2009). High-rate GPS clock corrections from CODE: support of 1 Hz applications. Journal of Geodesy, 83, 1083-1094, doi: 10.1007/s00190-009-0326-1.

Caissy, M., L. Agrotis, G. Weber, M. Hernandez-Pajares, and U. Hugentobler (2012), Coming Soon: The International GNSS Real-Time Service, GPS World, Jun 2012, Vol. 23 Issue 6, p52.

Chen, H., Jiang, W., Ge, M., Wickert, J., & Schuh, H. (2014). An enhanced strategy for GNSS data processing of massive networks. Journal of Geodesy, 88, 857-867, doi: 10.1007/s00190-014-0727-7.

Chen, L., Song, W., Yi, W., Shi, C., Lou, Y., & Guo, H. (2017). Research on a method of real-time combination of precise GPS clock corrections. GPS solutions, 21, 187-195, doi: 10.1007/s10291-016-0515-3.

Chen, L., Zhao, Q., Hu, Z., Jiang, X., Geng, C., Ge, M., & Shi, C. (2018). GNSS global real-time augmentation positioning: Real-time precise satellite clock estimation, prototype system construction and performance analysis. Advances in Space Research, 61(1), 367-384, doi: 10.1016/j.asr.2017.08.037.

Chen, X., Allison, T., Cao, W., Ferguson, K., Grunig, S., Gomez, V., ... & Talbot, N. (2011, September). Trimble RTX, an innovative new approach for network RTK. In Proceedings of the 24th international technical meeting of the satellite division of the institute of navigation (ION GNSS 2011) (pp. 2214-2219).

Choy, S., Bisnath, S., & Rizos, C. (2017). Uncovering common misconceptions in GNSS Precise Point Positioning and its future prospect. GPS solutions, 21, 13-22, doi: 10.1007/s10291-016-0545-x.

Collins, P., Lahaye, F., Heroux, P., & Bisnath, S. (2008, September). Precise point positioning with ambiguity resolution using the decoupled clock model. In Proceedings of the 21st international technical meeting of the satellite division of the Institute of Navigation (ION GNSS 2008) (pp. 1315-1322).

Deng, Z., Fritsche, M., Uhlemann, M., Wickert, J., & Schuh, H. (2016, February). Reprocessing of GFZ multi-GNSS product GBM. In IGS workshop (pp. 08-12).

Deng, Z., Wang, J., & Ge, M. (2022, May). The GBM rapid product and the improvement from undifferenced ambiguity resolution. In EGU General Assembly Conference Abstracts (pp. EGU22-794), doi: 10.5194/egusphere-egu22-794

Dixon, K. (2006, September). StarFire: A global SBAS for sub-decimeter precise point positioning. In Proceedings of the 19th international technical meeting of the satellite division of the institute of navigation (ION GNSS 2006) (pp. 2286-2296).

Dong, D. N., & Bock, Y. (1989). Global positioning system network analysis with phase a mbiguity resolution applied to crustal deformation studies in California. Journal of G eophysical Research: Solid Earth, 94(B4), 3949-3966, doi: 10.1029/JB094iB04p039 49

Dow, J. M., Neilan, R. E., & Rizos, C. (2009). The international GNSS service in a changing landscape of global navigation satellite systems. Journal of geodesy, 83, 191-198, doi: 10.1007/s00190-008-0300-3.

Dow, J. M., Neilan, R. E., & Rizos, C. (2009). The international GNSS service in a changing landscape of global navigation satellite systems. Journal of geodesy, 83, 191-198, doi: 10.1007/s00190-008-0300-3.

Duong, V., Harima, K., Choy, S., Laurichesse, D., & Rizos, C. (2019). An optimal linear combination model to accelerate PPP convergence using multi-frequency multi-GNSS measurements. GPS Solutions, 23, 1-15, doi: 10.1007/s10291-019-0842-2.

El-Mowafy, A., Deo, M., & Kubo, N. (2017). Maintaining real-time precise point positioning during outages of orbit and clock corrections. GPS solutions, 21, 937-947, doi: 10.1007/s10291-016-0583-4.

ESA (2012) SENTINEL-3, ESA's Global Land and Ocean Mission for GMES Operationa l Services. European Space Agency. https://sentinel.esa.int/documents/247904/35118 7/S3_SP-1322_3.pdf

Fotopoulos, G., & Cannon, M. E. (2001). An overview of multi-reference station methods for cm-level positioning. GPS solutions, 4, 1-10, doi: 10.1007/PL00012849.

Fu, W., Huang, G., Zhang, Q., Gu, S., Ge, M., & Schuh, H. (2019). Multi-GNSS real-time clock estimation using sequential least square adjustment with online quality control. Journal of Geodesy, 93, 963-976, doi: 10.1007/s00190-018-1218-z.

Gao, Y., & Shen, X. (2001, September). Improving ambiguity convergence in carrier phase-based precise point positioning. In Proceedings of the 14th international technical meeting of the Satellite Division of the Institute of Navigation (ION GPS 2001) (pp. 1532-1539).

Ge, H., Li, B., Nie, L., Ge, M., & Schuh, H. (2020). LEO constellation optimization for LEO enhanced global navigation satellite system (LeGNSS). Advances in Space Research, 66(3), 520-532, doi: 10.1016/j.asr.2020.04.031.

Ge, M., Chen, J., Douša, J., Gendt, G., & Wickert, J. (2012). A computationally efficient approach for estimating high-rate satellite clock corrections in realtime. GPS solutions, 16, 9-17, doi: 10.1007/s10291-011-0206-z.

Ge, M., Douša, J., Li, X., Ramatschi, M., Nischan, T., & Wickert, J. (2012). A novel real-time precise positioning service system: global precise point positioning with regional augmentation. Journal of global positioning systems, 11(1), 2-10, doi: 10.5081/jgps.11.1.2.

Ge, M., Gendt, G., Rothacher, M. A., Shi, C., & Liu, J. (2008). Resolution of GPS carrier-phase ambiguities in precise point positioning (PPP) with daily observations. Journal of geodesy, 82, 389-399, doi: 10.1007/s00190-007-0187-4.

Geng, J., Guo, J., Meng, X., & Gao, K. (2020). Speeding up PPP ambiguity resolution using triple-frequency GPS/BeiDou/Galileo/QZSS data. Journal of Geodesy, 94, 1-15, doi: 10.1007/s00190-019-01330-1.

Geng, J., Teferle, F. N., Shi, C., Meng, X., Dodson, A. H., & Liu, J. (2009). Ambiguity resolution in precise point positioning with hourly data. GPS solutions, 13, 263-270, doi: 10.1007/s10291-009-0119-2.

Geng, J., Shi, C., Ge, M., Dodson, A. H., Lou, Y., Zhao, Q., & Liu, J. (2012). Improving the estimation of fractional-cycle biases for ambiguity resolution in precise point positioning. Journal of Geodesy, 86, 579-589, doi: 10.1007/s00190-011-0537-0.

Gong, X., Gu, S., Lou, Y., Zheng, F., Ge, M., & Liu, J. (2018). An efficient solution of real-time data processing for multi-GNSS network. Journal of Geodesy, 92, 797-809, doi: 10.1007/s00190-017-1095-x.

Gómez Skarmeta, A. F., Barberá, H. M., Izquierdo, M. Z., Miñarro, B. Ú., Quiñonero, J. C., & Cáceres, D. A. (2003). Evaluation of EGNOS (GNSS-1) for Application in a Vehicle Driving Support System. In Satellite Navigation Systems: Policy, Commercial and Technical Interaction (pp. 175-182). Springer Netherlands， doi: 10.1007/978-94-017-0401-4_19.

Gu, S., Lou, Y., Shi, C., & Liu, J. (2015). BeiDou phase bias estimation and its application in precise point positioning with triple-frequency observable. Journal of Geodesy, 89(10), 979-992, doi: 10.1007/s00190-015-0827-z.

Hadas, T., Hobiger, T., & Hordyniec, P. (2020). Considering different recent advancements in GNSS on real-time zenith troposphere estimates. GPS Solutions, 24(4), 99, doi: 10.1007/s10291-020-01014-w.

Hauschild, A., & Montenbruck, O. (2009). Kalman-filter-based GPS clock estimation for near real-time positioning. GPS solutions, 13, 173-182, doi: 10.1007/s10291-008-0110-3.

Hernández-Pajares, M., Juan, J. M., Sanz, J., Aragón-Àngel, À., García-Rigo, A., Salazar, D., & Escudero, M. (2011). The ionosphere: effects, GPS modeling and the benefits for space geodetic techniques. Journal of Geodesy, 85, 887-907, doi: 10.1007/s00190-011-0508-5.

Hopfield, H. S. (1969). Two-quartic tropospheric refractivity profile for correcting satellite data. Journal of Geophysical research, 74(18), 4487-4499, doi: 10.1029/JC074i018p04487.

Johnston, G., Riddell, A., & Hausler, G. (2017). The international GNSS service. Springer handbook of global navigation satellite systems, 967-982, doi: 10.1007/978-3-319-42928-1_33.

Jiang, W., Liu, T., Chen, H., Song, C., Chen, Q., & Geng, T. (2023). Multi-frequency phase observable-specific signal bias estimation and its application in the precise point positioning with ambiguity resolution. GPS Solutions, 27(1), 4. doi: 10.1007/s10291-022-01325-0

Jiang, X., Gu, S., Li, P., Ge, M., Schuh, H. (2019): A Decentralized Processing Schema for Efficient and Robust Real-time Multi-GNSS Satellite Clock Estimation. Remote Sensing, 11, 21, 2595. doi: 10.3390/rs11212595

Katsigianni, G., Perosanz, F., Loyer, S., & Gupta, M. (2019). Galileo millimeter-level kinematic precise point positioning with ambiguity resolution. Earth, Planets and Space, 71, 1-6, doi: 10.1186/s40623-019-1055-1.

Kazmierski, K., Sośnica, K., & Hadas, T. (2018). Quality assessment of multi-GNSS orbits and clocks for real-time precise point positioning. GPS Solutions, 22, 1-12, doi: 10.1007/s10291-017-0678-6.

Laurichesse, D., Cerri, L., Berthias, J. P., & Mercier, F. (2013, September). Real time precise GPS constellation and clocks estimation by means of a Kalman filter. In Proceedings of the 26th international technical meeting of the satellite division of the institute of navigation (ION GNSS+ 2013) (pp. 1155-1163).

Laurichesse, D., Mercier, F., Berthias, J. P., & Bijac, J. (2008, January). Real time zero-difference ambiguities fixing and absolute RTK. In Proceedings of the 2008 national technical meeting of the institute of navigation (pp. 747-755).

Laurichesse, D., Mercier, F., & Berthias, J. P. (2009, January). Real time precise GPS constellation orbits and clocks estimation using zero-difference integer ambiguity fixing. In Proceedings of the 2009 international technical meeting of the institute of navigation (pp. 664-672).

Leandro, R. F., Santos, M. C., & Langley, R. B. (2011). Analyzing GNSS data in precise point positioning software. GPS solutions, 15, 1-13, doi: 10.1007/s10291-010-0173-9.

Lichten, S. M. (1990). Estimation and filtering for high-precision GPS positioning applications. Manuscripta Geodaetica, 15, 159-176.

Li, P., Jiang, X., Zhang, X., Ge, M., & Schuh, H. (2020a). GPS+ Galileo+ BeiDou precise point positioning with triple-frequency ambiguity resolution. GPS Solutions, 24, 1-13, doi: 10.1007/s10291-020-00992-1.

Li, P., Zhang, X., & Guo, F. (2017). Ambiguity resolved precise point positioning with GPS and BeiDou. Journal of geodesy, 91, 25-40, doi: 10.1007/s00190-016-0935-4.

Li, X., Chen, X., Ge, M., & Schuh, H. (2019a). Improving multi-GNSS ultra-rapid orbit determination for real-time precise point positioning. Journal of Geodesy, 93(1), 45-64, doi: 10.1007/s00190-018-1138-y.

Li, X., Ge, M., Dai, X., Ren, X., Fritsche, M., Wickert, J., & Schuh, H. (2015). Accuracy and reliability of multi-GNSS real-time precise positioning: GPS, GLONASS, BeiDou, and Galileo. Journal of geodesy, 89(6), 607-635, doi: 10.1007/s00190-015-0802-8.

Li, X., Ge, M., Douša, J., & Wickert, J. (2014). Real-time precise point positioning regional augmentation for large GPS reference networks. GPS solutions, 18, 61-71, doi: 10.1007/s10291-013-0310-3.

Li, X., Liu, G., Li, X., Zhou, F., Feng, G., Yuan, Y., & Zhang, K. (2020b). Galileo PPP rapid ambiguity resolution with five-frequency observations. GPS Solutions, 24, 1-13, doi: 10.1007/s10291-019-0930-3.

Li, X., Li, X., Liu, G., Feng, G., Yuan, Y., Zhang, K., & Ren, X. (2019b). Triple-frequency PPP ambiguity resolution with multi-constellation GNSS: BDS and Galileo. Journal of geodesy, 93, 1105-1122, doi: 10.1007/s00190-019-01229-x.

Li, X., Zhang, X., & Ge, M. (2011). Regional reference network augmented precise point positioning for instantaneous ambiguity resolution. Journal of Geodesy, 85, 151-158, doi: 10.1007/s00190-010-0424-0.

Liu, J., Ge, M. (2003). PANDA software and its preliminary result of positioning and orbit determination. Wuhan University Journal of Natural Sciences, 8(2), 603-609, doi: 10.1007/BF02899825.

Liu, Y., Ye, S., Song, W., Lou, Y., & Gu, S. (2017). Rapid PPP ambiguity resolution using GPS+ GLONASS observations. Journal of Geodesy, 91, 441-455, doi: 10.1007/s00190-016-0975-9

Montenbruck, O., Steigenberger, P., & Hauschild, A. (2015). Broadcast versus precise ephemerides: a multi-GNSS perspective. GPS solutions, 19, 321-333, doi: 10.1007/s10291-014-0390-8.

Mervart, L., & Weber, G. (2011, September). Real-time combination of GNSS orbit and clock correction streams using a Kalman filter approach. In Proceedings of the 24th International Technical Meeting of The Satellite Division of the Institute of Navigation (ION GNSS 2011) (pp. 707-711).

Montenbruck, O., Rizos, C., Weber, R., Weber, G., Neilan, R., & Hugentobler, U. (2013). Getting a grip on multi-GNSS: The international GNSS service MGEX campaign. GPS world, 24(7), 44-49.

Montenbruck, O., Steigenberger, P., & Hugentobler, U. (2015). Enhanced solar radiation pressure modeling for Galileo satellites. Journal of Geodesy, 89, 283-297, doi: 10.1007/s00190-014-0774-0.

Montenbruck, O., Hauschild, A., & Steigenberger, P. (2014). Differential code bias estimation using multi-GNSS observations and global ionosphere maps. NAVIGATION: Journal of the Institute of Navigation, 61(3), 191-201, doi: 10.1002/navi.64.

Musa, T. A., Lim, S., & Rizos, C. (2005, September). GPS Network-Based Approach to Mitigate Residual Tropospheric Delay in Low Latitude Areas. In Proceedings of the 18th International Technical Meeting of the Satellite Division of The Institute of Navigation (ION GNSS 2005) (pp. 2606-2613).

Muellerschoen,R J., Bar-Server,Y E., Bertiger, W I., &Stowers, D A. (2001, January) NASA's Global DGPS for High-Precision Users. GPS World, 12(1), 14–20.

Odijk, D., Zhang, B., & Teunissen, P. J. (2015). Multi-GNSS PPP and PPP-RTK: Some GPS+ BDS Results in Australia. In China Satellite Navigation Conference (CSNC) 2015 Proceedings: Volume II (pp. 613-623). Springer Berlin Heidelberg, doi: 10.1007/978-3-662-46635-3_52.

Pinker, A., Smith, C., & Day, J. (2000). Wide-area augmentation system (WAAS)–the metamorphosis of a major FAA program. GPS Solutions, 3, 48-57, doi: 10.1007/PL00012815.

Prange, L., Orliac, E., Dach, R., Arnold, D., Beutler, G., Schaer, S., & Jäggi, A. (2017). CODE's five-system orbit and clock solution—the challenges of multi-GNSS data analysis. Journal of geodesy, 91, 345-360, doi: 10.1007/s00190-016-0968-8.

Pratt, M., Burke, B., & Misra, P. (1997, September). Single-epoch integer ambiguity resolution with GPS L1-L2 carrier phase measurements. In Proceedings of the 10th International Technical Meeting of the Satellite Division of The Institute of Navigation (ION GPS 1997) (pp. 1737-1746).

Ray, J., Dong, D., & Altamimi, Z. (2004). IGS reference frames: status and future improvements. GPS solutions, 8, 251-266, doi: 10.1007/s10291-004-0110-x.

Rebischung, P., Altamimi, Z., Ray, J., & Garayt, B. (2016). The IGS contribution to ITRF2014. Journal of Geodesy, 90(7), 611-630, doi: 10.1007/s00190-016-0897-6.

Rocken, C., Johnson, J., Van Hove, T., & Iwabuchi, T. (2005). Atmospheric water vapor and geoid measurements in the open ocean with GPS. Geophysical research letters, 32(12), doi: 10.1029/2005GL022573.

RTCM. Radio Technical Commission for Maritime Services (RTCM) Standard 10403.3, Differential GNSS (Global Navigation Satellite Systems) Services; Radio Technical Commission for Maritime Services, Arlington, Virginia, U.S.A., 2016.

Saastamoinen, J. J. B. G. (1973). Contributions to the theory of atmospheric refraction: Part II. Refraction corrections in satellite geodesy. Bulletin Géodésique (1946-1975), 107, 13-34, doi: 10.1007/BF02522083.

Shi, C., Geng, J., Meng, X., Ge, M., Teferle, N., & Dodson, A. (2008). A novel real-time data screening approach in urban navigation. In ENC GNSS (pp. 23-25).

Shi, C., Zhao, Q., Geng, J., Lou, Y., Ge, M., & Liu, J. (2008, December). Recent development of PANDA software in GNSS data processing. In International Conference on Earth Observation Data Processing and Analysis (ICEODPA) (Vol. 7285, pp. 558-566). SPIE, doi: 10.1117/12.816261.

Snay, R. A., & Soler, T. (2008). Continuously operating reference station (CORS): history, applications, and future enhancements. Journal of Surveying Engineering, 134(4), 95-104.

Steigenberger, P., Hugentobler, U., Loyer, S., Perosanz, F., Prange, L., Dach, R., ... & Montenbruck, O. (2015). Galileo orbit and clock quality of the IGS Multi-GNSS Experiment. Advances in space research, 55(1), 269-281, doi: 10.1016/j.asr.2014.06.030.

Stürze, A., Mervart, L., Weber, G., Rülke, A., Wiesensarter, E., & Neumaier, P. (2016, April). The new version 2.12 of BKG Ntrip Client (BNC). In Geophys. Res. Abstr (Vol. 18, p. 12012).

Teunissen, P. J. G. (1990). Quality control in integrated navigation systems. IEEE aerospace and electronic systems magazine, 5(7), 35-41, doi: 10.1109/62.134219.

Teunissen, P. J. G., Khodabandeh, A., & Zhang, B. (2016). Multi-GNSS PPP-RTK: mixed-receiver network and user scenarios. In International Symposium on Earth and Environmental Sciences for Future Generations: Proceedings of the IAG General Assembly, Prague, Czech Republic, June 22-July 2, 2015 (pp. 215-221). Cham: Springer International Publishing, doi: 10.1007/1345_2016_232.

Teunissen, P. J. G. (1995). The least-squeres ambiguity decorrelation adjustment: a method for fast GPS integer ambiguity estimation. J. Geod., 70, 65-82, doi: 10.1186/BF03352298

Ventura-Traveset, J., López de Echazarreta, C., Lam, J. P., & Flament, D. (2015). An Introduction to EGNOS: The European Geostationary Navigation Overlay System. GALILEO Positioning Technology, 323-358, doi: 10.1007/978-94-007-1830-2_14.

Wang, N., Yuan, Y., Li, Z., Montenbruck, O., & Tan, B. (2016). Determination of differential code biases with multi-GNSS observations. Journal of Geodesy, 90, 209-228, doi: 10.1007/s00190-015-0867-4.

Wang, N., Li, Z., Duan, B., Hugentobler, U., & Wang, L. (2020). GPS and GLONASS observable-specific code bias estimation: comparison of solutions from the IGS and MGEX networks. Journal of Geodesy, 94, 1-15, doi: 10.1007/s00190-020-01404-5.

Wübbena, G., Schmitz, M., & Bagge, A. (2005, September). PPP-RTK: precise point positioning using state-space representation in RTK networks. In Proceedings of the 18th international technical meeting of the satellite division of the Institute of navigation (ION GNSS 2005) (pp. 2584-2594).

Yang, Y., & Gao, W. (2006). An optimal adaptive Kalman filter. Journal of Geodesy, 80, 177-183, doi: 10.1007/s00190-006-0041-0.

Yang, Y., Gao, W. G., & Zhang, X. D. (2010). Robust Kalman filtering with constraints: a case study for integrated navigation. Journal of Geodesy, 84, 373-381, doi: 10.1007/s00190-010-0374-6.

Zhang, B., Chen, Y., & Yuan, Y. (2019). PPP-RTK based on undifferenced and uncombined observations: theoretical and practical aspects. Journal of Geodesy, 93, 1011-1024, doi: 10.1007/s00190-018-1220-5.

Zhang, X., Li, X., & Guo, F. (2011). Satellite clock estimation at 1 Hz for realtime kinematic PPP applications. GPS solutions, 15, 315-324, doi: 10.1007/s10291-010-0191-7.

Zhang, W., Lou, Y., Gu, S., Shi, C., Haase, J. S., & Liu, J. (2016). Joint estimation of GPS/BDS real-time clocks and initial results. GPS solutions, 20, 665-676, doi: 10.1007/s10291-015-0476-y.

Zumberge, J. F., Heflin, M. B., Jefferson, D. C., Watkins, M. M., & Webb, F. H. (1997). Precise point positioning for the efficient and robust analysis of GPS data from large networks. Journal of geophysical research: solid earth, 102(B3), 5005-5017, doi: 10.1029/96JB03860.

Zuo, X., Jiang, X., Li, P., Wang, J., Ge, M., & Schuh, H. (2021). A square root information filter for multi-GNSS real-time precise clock estimation. Satellite Navigation, 2, 1-14, doi: 10.1186/s43020-021-00060-0.

Acknowledgments

The completion of this dissertation would not have been possible without the great help and support of a number of people and organizations.

First and foremost, I would like to express my sincere gratitude to my supervisors, Prof. Dr. Harald Schuh and Prof. Dr. Maorong Ge at Technischen Universität Berlin (TUB) and GFZ for their patient guidance, valuable suggestions and continuous encouragement throughout my study at GFZ as a Ph.D. student. They were always willing to share their insights and gave me suggestions and responded to my questions and queries promptly.

I would like to thank my current and former colleagues at GFZ, Dr. Jungang Wang, Dr. Xingxing Li, Dr. Pan Li, Dr. Shengfeng Gu, Dr. Xinghan Chen, Dr. Wen Huang and many other Ph.D. students for their kind help to my academic study and daily life.

Thanks to Dr. Zhiguo Deng for his concern both in my study and life.

Thanks to Mr. Thomas Nischan and Mrs. Sylvia Magnussen at GFZ for their patient technical support.

I owe a special gratitude to Prof. Shengli Wang from Shandong University of Science and Technology, whose selfless and extensive support and guidance always inspire me step forward. I also feel grateful to Dr. Yong Zhang from Southeast University for his continuous help and support with my work.

Many thanks to GFZ and TUB for hosting and supporting my work.

Finally, I would like to express my gratitude to my family for their endless understanding, support and encouragement. The person I wish to thank most is my wife Meiwei and my daughter Charlotte, who fills my heart with confidence, courage and love all the time.